Alma Mater Studiorum – Università di Bologna

DOTTORATO DI RICERCA IN

Ingegneria Biomedica Elettrica e dei Sistemi IBES

Ciclo XXX

Settore Concorsuale: 09/E1

Settore Scientifico Disciplinare: ING-IND/31

THERMAL STABILITY AND AC LOSSES IN HIGH-FIELD SUPECONDUCTING MAGNETS

Presentata da: Lorenzo Cavallucci

Coordinatore Dottorato   **Supervisore**

Prof. Daniele Vigo   **Prof. Marco Breschi**

Esame finale anno 2018

Abstract

The study and the analysis of quench initiation and propagation is of paramount importance in the design of any superconducting magnets. Several disturbances such as ac losses, failures of the cryogenics or heat load may induce the quench initiation on a magnet and determine its irreversible transition to the normal state. Since the early days of magnet construction, the scientific community has devoted significant efforts in the study of quench.

In the present work, numerical methodologies are presented and discussed for the analysis of electro-thermal stability, quench propagation and temperature margin on superconducting cables and coils. The proposed models are applied to the analysis of several superconducting magnets under development in different research groups in Europe (EU) and United States (US).

The comparison of the numerical results with the experimental tests or with different computational approaches make the author confident about the applicability and reliability of the proposed modelling techniques.

Contents

Introduction

One of the main technical issues in the operation of superconducting magnets is the protection in the event of quench, the irreversible transition from the superconducting to the normal state that may occur due to the deposition of external heat input on the conductor. These energy disturbances may arise from several phenomena, such as cracking of the insulating materials, failures of the cryogenic system, ac losses in the conductor during electromagnetic transients, secondary particle showers in accelerator magnets or nuclear heat load in fusion magnets. Prompt detection of a normal zone and efficient protection of the magnets is important to avoid damages due to the high temperatures that may be reached in the hot spots following the electro-thermal instability.

Aim of this study is hence to discuss some of the principal disturbances than can arise during the normal operation of real magnets. Numerical methods are developed to analyse different magnets configurations during their operative conditions.

A description of the state of the art is a fundamental step to be aware of the know-how and progresses of the scientific community to analyse quench with different methodologies. Hence, the different approaches presented in the literature for the study of quench in high temperature superconductors are described in the first chapter of the present work

The National High Magnetic Field Laboratory (NHMFL), Tallahassee, FL, USA, is presently testing a 32-T all-superconducting user magnet system, combining two series-connected nested high-field HTS inner coils (insert) pancake-wound with SuperPower Rare Earth Barium Copper Oxide (REBCO) tapes and a low-temperature superconducting (LTS) outsert magnet composed of five coils split into 17 electric sections. As a part of the research and fabrication activities for the magnet development, different prototype coils are tested. In the second chapter, the electromagnetic and thermal stability is studied by a quasi 3-D Finite Element Model (FEM) model for the first prototype coils wound in the frame of the 32 T magnet project. The first prototype is a foretype of the real insert of the 32 T magnet. Heater spacers located on the pancakes are fired in case of quench event. Scope of this study is to analyse the quench initiation and propagation, the temperature distribution and the hot spot temperature evolution during the

heaters firing and to focus on the contribution of the different pancakes on the quench of the whole magnet. In order to study the coupling between double HTS inserts and an LTS outsert, as in the 32 T real configuration, in the third chapter, a second prototype is also analysed in the presence of an LTS outsert able to provide a background magnetic field. The inductive coupling and the energy exchange between the HTS insert and the LTS outsert during the quench of both the HTS and the LTS magnets is analysed and discussed. The 32 T magnet itself is modelled in a selected test case without the presence of the LTS insert. The quench propagation and the determination of the most stressed pancakes is analysed and discussed.

In the fifth chapter, in the frame of the EUCARD 2 project, the same numerical approach used for the NHMFL quench studies is applied for the electrical and thermal stability analysis of a Roebel cable composed of 15 REBCO based tapes. A model based on the finite element method is implemented to analyse the heat and current redistribution in the case of pointwise disturbances applied to a single strand of the cable.

In both the analysis for the NHMFL prototypes and of the EUCARD2-Roebel cable, the slow time-varying magnetic field allows one to study the stability without accounting for the coupling and magnetization losses. In the second part of this study, in the frame of the design of the first superconductive Gantry magnet for cancer therapy at the Paul Scherrer Institute (Switzerland), the electrothermal stability of the Gantry is analysed during its operation cycle. The magnetic flux density variation during the cycle to bend the beam particle causes coupling and hysteresis losses in the Gantry magnet system. In the the sixth chapter, the approaches applied for the computation of the coupling losses in the Gantry magnet system are detailed and widely described. The electromagnetic ac and coupling losses of the Gantry configuration are presented and the temperature margin is discussed comparing the temperature distribution at the end of the operating cycle with the current sharing temperature of the magnet.

Part I

Modeling of Quench in HTS Superconductive Magnets

Chapter 1

State of the Art of Quench Modeling in HTS Superconductive Magnets

1.1 Introduction

The possibility of High Temperature Superconductors (HTS) to carry high current densities at intense magnetic field has increased the interest of the scientific community in the application of HTS tapes to the realization of high field magnets [1]-[5] as shown in Table 1.1.

The prompt detection of quench and the efficient protection of the magnets is important to avoid damages due to the high temperatures that may be reached in the hot spots following the electro-thermal instability. The high specific heat and low thermal conductivity of the HTS materials with respect to the LTS determine a propagation of the normal zone in the HTS magnets slower than in the LTS devices, thus determining difficulties in the prompt response and detection of the quench event.

Hence, during the R&D activity for magnets fabrication, and particularly for HTS windings, foundamental step is the analysis of the initiation and the propagation of normal zone which is needed for the quench protection of the magnet from sudden burn and breakdown.

Since the early days of magnet construcition, the scientific communty has then devoted large efforts in the study of quench. One of the first methods for simulating the quench event was presented by Wilson in 1968 [6]. The method was based on the computation of the energy required to quench a magnet. Wilson defined the smallest normal conducting volume that is required in the coil for the normal zone to spread, namely, the minimum propagating zone (MPZ). The energy that is required to create MPZ is called MQE. By using the MQE concept, the heater energy required to quench an LTS magnet can easily be estimated. In fact, the first widely

Table 1.1:
HTS HIGH FIELD PROJECTS [5]

Project	Type	ΔB HTS/LTS	HTS	J_{ave} A/mm^2	Final Data	Comment
32 T NHMFL	user magnet	17/15	REBCO REBCO	200 170	2017	insulated
25 T Tohoku	user magnet	10.6/14	REBCO	112	2016	insulated
28 T Bruker	user magnet	-	-	-	-	-
28 T RIKEN	demo	11.5/17.1	REBCO Bi-2223	157 78	-	insulated
Muon collider solenoid	demo	15/0	REBCO	539	-	no insulated
26 T SuNAM-MIT	demo	26.4/0	REBCO	343	-	no insulated
25 T IEE-CAS	demo	10.7/15	REBCO	267	-	no insulated
30.5 T MIT	user magnet	18.8/11.7	REBCO REBCO REBCO	547	2020	no insulated

used computer program for simulating quench was Wilsons QUENCH [6], which is based on the MPZ concept. QUENCH was very useful in the 1980s, when computers were not advanced enough to solve large problems in three dimensions utilizing the finite-element method (FEM) or finite-difference method in adequate time. Later, other codes based on quench propagation were also presented, e.g., PQUENCH [7] and QLASA [8]. In the 1990s, an extensive code based on difference method was developed at the National High Magnetic Field Laboratory [9], [10]. Later, commercial software like ANSYS, Comsol or Opera have been utilized to solve the heat diffusion equation with Finite Element Methods. In addition, simulation tools for specific tasks have been developed. For example, CUDI has been used to analyze quench propagation in Rutherford cables [11].

The field of quench modelling has become a long way up to the present state of art and it is impossible to discuss and present all the models developed by the scientific community over the years to analyse quench in superconducting devices. The present introduction therefore focuses on some of the different models and approaches developed by the scientific community.

The usual methods for modeling the transition behaviour of superconducting magnets include a variety of modeling techniques, such as analytical equations [12]-[15], equivalent network circuits with lumped elements [16]-[26], homogenized coil models [27]-[40].

Several scientific groups applied the different techniques to study the quench propagation and initiation in High Temperature Superconductive (HTS) devices. In order to focus on the quench modelling in the High Temperature Superconductive magnets, the different methodologies are analysed and discussed in the following chapters.

Before presenting the different models for the study of quench, an introductory qualitative description of the quench phenomenon and of the constitutive law that characterize the superconducting materials are necessarily introduced.

1.2   A Qualitative Introduction of Quench

A superconductive magnet is usually cooled at cryogenics temperature and then energized by the flow of the transport current. Since the presence of the superconductive material, the current will flow with ideally no losses in the magnet. The presence of the cryogenic system will remove heat coming from external disturbances. In the design condition, the cooling system is always able to remove the exceeding heat but particular external heat depositions could determine the transition of the conductor to the normal state. The increase of a steady state heat input, the high magnetic filed variation and the consequent coupling and hysteresis losses induced, the sudden slipping among components and the cracking of the epoxy could deposit external heat in the conductor [41]. During the first 0.1 ms or 1 ms of quench initiation, the sudden energy deposition in a localized region could determine the increase of the temperature of the superconductor and after about 10 ms, if the temperature increase is enough, the current is shared between the superconditive material and the other materials that compose the cable determining the current sharing regime and the generation of Joule heat in addition to the external disturbances.

Depending on the heat balance between heat deposition and removal through the convection and conduction heat fluxes or through cryogenic systems, the conductor could recover to its initial temperature (and the superconducting state) or could increase rapidly its temperature.

If the power balance is favourable for cooling, after 10 ms or 100 ms, the material is recovered to its superconducting state and after 1 s or 10 s, the coil recover its normal operating conditions.

In the negative event of power balance unfavourable, in the hot spot are of the magnet, the initiation of thermal runaway determines the quench propagation through conduction and convection. The normal zone propagate throughout the coil causing the resistance to build up and the magnet to quench.

An external quench protection system is included to protect the magnet from disruption caused by the quench propagation. If a threshold voltage

is exceeded, the quench protection system will detect the quench event and the power supply is switched off. A resistance will close the coil terminals in order to dissipate the magnetic energy stored in the coil. If the magnetic energy is not extracted, the energy is converted into heat through the Joule process determining the damage or even the disruption of the magnet.

If the protection and detection system fails the current behaviour in the magnet will be determined only according to the internal resistance of the conductor, the characteristic of the power supply and the coupling to the other coils. Of paramount importance for the safety design of the coil and of the protection system is therefore an appropriate and wide analysis of the quench initiation and propagation.

1.3 Constitutive Laws of Superconductig Material

Since the discovery of superconductivity, during the decades, the scientific community developed several relations for the characterization of the electro-magnetic behaviour of superconducting materials. As presented by Pierluigi Bruzzone in [42], the voltagecurrent (VI) characteristic of a bulk superconductor can be illustrated by a two-range plot with the first section as a flat, zero-resistance line and the other section as a linear, resistive slope, as shown in Figure 1.1. The change of slope in the Figure defines the transition from the superconductors to the normal state and is defined as the critical current I_c of the superconducting device. The slope of the curve above I_c is determined on the base of the flux flow resistance, R_f, when the lattice of the pinning center is no longer able to anchor the flux lines. A first theoret-
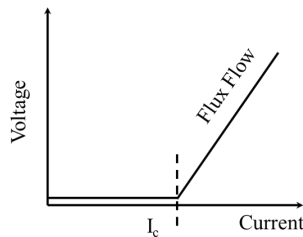
Figure 1.1: Ideal VI for a bulk homogeneous superconductor with linear flux flow range

ical dissertation of the VI for bulk superconductors was given in the 1967 by Jones $et\ al.$ The authors related the local critical current distribution $f(j_c)$ with the profile of the VI profile, leading to the basic formula for the deconvulation by differentiation

$$\frac{\partial^2 E}{\partial J^2} = \rho_f\, f(j_c) \tag{1.1}$$

where E is the longitudinal electric field measured along the conductor.

In the same years, Baixereas and Fournet [43] derived an analogous formulation that derives from the analysis of pinning forces distribution during ac losses.

On the other side, the scientific community proposed several empirical fits for the electro-magnetic characterization of superconducitve materials. The most commonly adopted empirical fit denominated "power law" was proposed by Walter [44] in 1974 and was quickly adopted in US and Europe.

$$E = E_c \left(\frac{I}{I_c} \right)^n \tag{1.2}$$

where E_c is the critical electric field usually set to $10\,\mu\mathrm{V/m}$ and I_c is the current at the critical field.

At high level of electric field, the n-index shows an increase to higher values. The behaviour is usually considered in literature as an evidence of the self-heating of the sample [44]- [46]. At low value of electric field, the theory predicts an exponential profile of the electric field [47]. The exponential behaviour was experimentally confirmed for bulk material in [48] and in [49] for monocore and multicore components.

A fitting formulation based on the exponential fit was proposed in [50]. The influence of the magnetic flux density, temperature and current on the VI formulation is introduced by three increasing parameters T_0, B_0 and J_0:

$$E = J\,\rho_n \, \exp\left(\frac{T - T_c}{T_0} + \frac{B}{B_0} + \frac{J}{J_0} \right) \tag{1.3}$$

where T_c is the critical temperature and ρ_n is the normal resistivity of the superconductor.

Recently, a modified formulation is presented in 2001 by Decroux *et al* in [51] to compute the flux flow resistivity $\rho_{super}\,(J,T)$ in superconductive material:

$$\rho_{super}\,(J,T) = \rho_0 \left(\frac{J}{J_c(T)} - 1 \right)^n \tag{1.4}$$

where T_c is the critical current temperature, $J_c(T)$ is the critical current at the temperature T, n the n-index of the power law and ρ_0 the equivalent resistivity at $2\,J_c$. The n-index and the equivalent resistivity at $2\,J_c$ are obtained through the characterization of the conductor. The interest of the formulation defined as "percolation law" is the reduced number of parameters that must be obtained through the characterization $(J_c(77), n, \rho_w)$ and the influence of these parameters in the studied range of temperature and current densities.

In the years, the scientific community oriented frequently to the use of the power law as a constitutive equation of the superconducting material. The most of the quench models presented in the literature and analysed in the following sections and moreover the models discussed in the chapters are based on the power law as a constitutive law of superconductors.

1.4 Quench Modeling: Analytical Methods

Thermal quench theory was developed by Vysotsky *et al.* in [14] and [52] to analyse and study the quench development in superconducting high-T_c materials of the first generation (BSCCO tapes). The theory was confirmed by many experiments in [53]-[56] and uses the standard power law for voltagecurrent (VI) of HTS superconductors. It was shown in [52] that near the thermal quench current (TQC) I_q, analytical expressions could be found for two cases. If $I < I_q$, the temperature stabilize at a level equal to $T_q - T_f$. Whereas, if $I > I_q$, the temperature rises with strong acceleration after the time t_q [52]-[55] and [57] [58]. The following expression have been found and discussed in [14].

Threshold thermal quench current I_q (TQC) can be computed as:

$$\frac{I_q}{I_0(T_0)} = \frac{n}{n+1} \left[\frac{hP\,(T_c - T_0)}{nE_0 I_0(T_0)} \right]^{1/(n+1)} \tag{1.5}$$

where E_0 is the critical electric field set to usual values of 1 or $0.1\,\mu\mathrm{V/cm}$. The current I_0 is the critical current, h is the heat transfer coefficient and P the cooling perimeter, T_0 the ambient temperature and T_c the critical temperature.

Characteristic time of the quench development can be computed as

$$t_q = t_h \left(\sqrt{\frac{2I_q}{\mid I - I_q \mid (n+1)}} \right) \arctan \left(\sqrt{\frac{I_q}{2 \mid I - I_q \mid (n+1)}} \right). \tag{1.6}$$

Finally, the time evolution of temperature and electric field in HTS devices is determined by the following relations:

$$\text{if } I > I_q \quad \frac{T(t) - T_q}{T_f} = \frac{E(t) - E_q}{E_f} = \tan\left(\frac{t - t_q}{t_f} \right) \tag{1.7}$$

where the characteristic temperature and electric fields are:

$$T_q = T_0 + \frac{T_c - T_0}{n+1} \quad , \quad T_f = (T_c - T_0) \sqrt{\frac{2 \mid I - I_q \mid}{I_q\,(n+1)}} \tag{1.8}$$

$$E_q = \frac{h\,P\,T_c}{I_0(T_0)\,n} \quad , \quad E_f = n\,E_q \sqrt{\frac{2 \mid I - I_q \mid}{I_q(n+1)}} \tag{1.9}$$

and the characteristic time is

$$t_f = t_h \sqrt{\frac{2I_q}{\mid I - I_q \mid (n+1)}}. \tag{1.10}$$

In the relations, T_q is a characteristic temperature at which fast temperature rise starts at time t_q while t_f is the time necessary to heat up a sample at

equilibrium temperature $T_q - T$ if $I < I_q$ [59]. The parameter t_h is the characteristic thermal time expressed by

$$t_h = \frac{C\ A}{P\ h} \qquad (1.11)$$

where C is the volumetrically averaged heat capacity and A is the conductor cross section area.

All the above expressions do not have adjusting parameters and were extensively verified by experiments [52] - [56]. It was also shown that the expressions 1.7 for $I > I_q$ are universal and could be scaled for the widest variety of superconducting applications made of BSCCO materials. In Fig 1.2 dependencies of dimensionless temperatures and voltages on dimensionless time are shown for different superconducting devices.

However, in a real magnets cooling, VI and critical currents of the winding material are not uniform over the magnets volume. To handle such cases, the analysis should start from the evaluation of the characteristic heat length: $l_h = \sqrt{Ak/Ph}$, that is the length through which the temperature is changing along the winding [54]. As the heat conductivity is changing little at temperatures of 2080 K, heat length is determined mainly by cooling conditions. It was shown in [54] by comparison of estimated heat lengths with winding characteristic sizes (experimental data were used), that in windings cooled by cryocoolers their dimensions are smaller than the characteristic length l_h, at least up to 1 m wide windings. So, conduction cooled windings can be considered as quasi-uniform with all parameters averaged along the winding [52], [54], [56] .
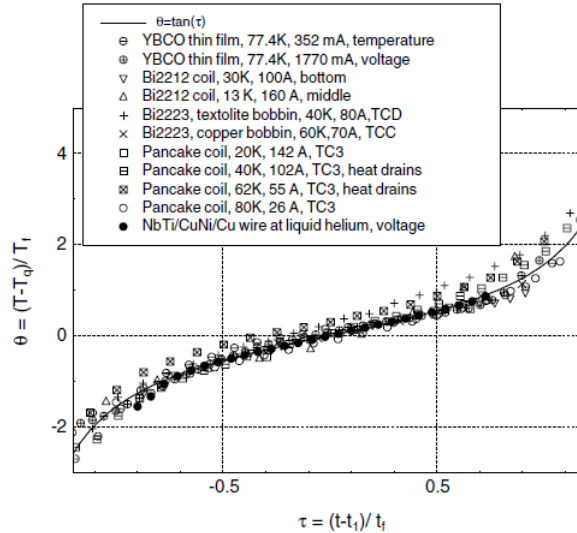

Figure 1.2: Dimensionless temperature θ versus dimensionless time τ for experiments with different objects [14].

1.5 Quench Modeling: Equivalent Network Circuit Models

Several models have been developed within the scientific community to build equivalent thermal and electrical network circuit models for the analysis of electromagnetic and thermal behaviour of superconductive magnets. The advantage of the equivalent circuit approach is the reduction of the degrees of freedom and, accordingly, the computation burden during the simulation activity. In opposition, the approach requires the determination of parameters like electrical or thermal contact resistances that are fundamental for the correct modeling but not easy to be determined experimentally.

The first model to present is a computer code developed by Andy Gavrilin *et al.* for the simulation of the normal zone propagation along winding turns where the turn to turn transverse heat transfer is taken into account both for LTS winding coils [60], [61], [62], [63] and for the analysis of quench in the HTS-based 32-magnet [64], [3], [5] at the National High Magnetic Field Laboratories[1].

The mathematical formulation reduces the governing 3D transient heat balance equation to an equivalent set of coupled 1D equations. Each 1D equation describes the heat balance in one turn with due regard to its thermal coupling with the neighbouring turns. The formulation can be expressed as:

$$\left(A_{Cu}\,C_{Cu} + A_{SC}\,C_{SC} + A_{ins}\left(C_{ins} + f\,\gamma_P^{He}\,C_P^{He}\right)\right)\frac{\partial T}{\partial t} =$$

$$\frac{\partial}{\partial x}\left(A_t\,k_t\,\frac{T}{x}\right) + A_t\,Q_j + A_t\,Q_{AC} + \sum_{i=1}^{4}\frac{P_i}{\delta_i}\,k_i^{(ins)}(T_i)\left(T^i - T\right) + P_{1(2)}\,Q_{heater}$$

$$(1.12)$$

where x is the coordinate along the spiral path following the superconducting tape axes in given pancake, $T = T(x,t)$ the tape temperature, A_{Cu} the tape copper matrix cross section area, A_{SC} the cross section area of the other materials of the tape, including hastelloy substrate etc.. The insulated tape heat capacity also includes the heat capacity of helium in the winding at constant pressure, f is the helium proportion of the insulation in terms of volume. The helium density $\gamma_P^{He}(T)$ is considered temperature dependent to mimic the helium vaporization process. The tape effective longitudinal conductivity k_t is considered as a function of the temperature T and magnetic flux density $B(x,T)$. The heating power density term includes the

---

[1]https://nationalmaglab.org/

Joule heating and AC loss in the superconducting area, in detail:

$$A_t\,Q_j + A_tQ_{AC} = A_t\,Q_J\left(T\left(x,t\right),I\left(t\right),B\left(x,t\right)\right) +$$
$$A_t\,Q_{AC}\left(T\left(x,t\right),I\left(t\right),B\left(x,t\right),\cdot B\left(x,t\right)\right) \tag{1.13}$$

The transverse thermal axial (disk-to-disk) and radial (turn-to-turn, within a disk) links are computed introducing a thermal contact resistance R_c characterizing the quality of the contact between the superconducting tape copper matrix and the insulation. The heat flux density from the quench protection heaters $Q_{heater}(x,t)$ is also introduced if any.

In the modeling activity concerning the analysis of quench of the 32 T-magnet prototypes and the 32 T-magnet itself, the presence of an LTS outsert is modeled based upon the same equations. In these cases, the circuit equations are included to compute the damping of the current in the model. In the following chapters, the results obtained through this code and the quasi 3D FEM model presented in the present work are compared for the R&D prototypes of the NHMFL and the 32 T-magnet itself.

More details about the model and its applications are discussed in [64], [3] and [5].

A different model was developed by Wang Tao, Noguchi So *et al.* for the analysis of transient behaviours of No-Insulation REBCO Pancake Coils. The PEEC (partial element equivalent circuit) model takes into account of the local turn-to-turn contact resistance, the VI characteristic, and the self and mutual inductances of the local coil elements within the No-Insulation (NI) winding to discuss the transient behavior in the NI coil in detail.

As known, a greater number of discrete elements results in a longer computation time, although a higher accuracy is obtained. Owing to the analysis efficiency enhancement in the PEEC analysis for sudden discharging, an No-Insulation pancake coil is subdivided into 18 azimuthal divisions per turn and into 72 azimuthal divisions per turn for the PEEC-thermal coupled analysis for overcurrent. The common PEEC model is shown in Fig. 1.3.

The model, constructed on the basis of Kirchhoff′s first and second laws, takes into account of the electrical resistances of the winding in the azimuthal direction (R_θ) through the non linear VI characteristic and in the radial direction (R_r) through a turn-to-turn contact resistance. Moreover the M matrix that includes the self and mutual inductances of the partial elements is introduced to compute the currents flowing in the azimuthal (I_θ) and radial (I_r) directions respectively.

To investigate the transient behavior in detail during an overcurrent, it is necessary to add a heat conduction analysis to the PEEC model to accurately evaluate the thermal dependence of the physical parameters including
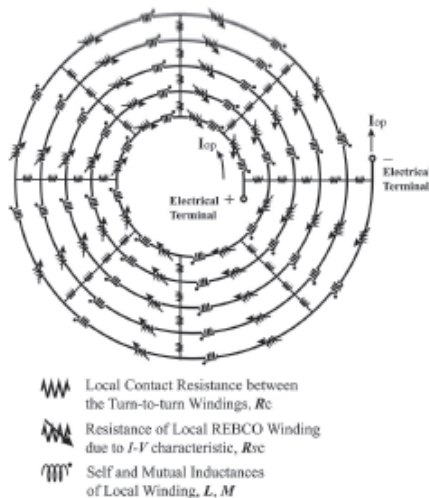
Figure 1.3: Sample of the PEEC model of an NI REBCO pancake coil, which has 8 azimuthal divisions per turn [19].

the electrical resistance, heat capacity, thermal conductivity, and VI characteristic in the local winding. The VI characteristic of a REBCO tape has a thermal as well as a magnetic field dependence, the magnetic field was computed through the Biot-Savart law and imported in the model. The thermal conductivities in the azimuthal (λ_θ) and radial (λ_r) directions are different because of the anisotropy of the insulated tapes.

The PEEC model is applied to the analysis of quench in No-Insulation HTS coils. In detail, turn to turn contact resistance [20] and [22], current behaviour [21], detection methods [23], quench protection [24], normal zone transition [26] are discussed and analysed in literature.

A different thermal network model coupled with a Finite Element coupled is presented by Janne Ruuskanen, Atti Stenvall and Valterri Lahtinen in [69]. The model is applied to the analysis of quench on Feather-M0 magnet (FM0) [70]. The magnet is wound with five turns of Roebel cable consisting of 15 REBCO tapes. A FEM approach is used to solve the heat diffusion equation for the 1D domain representing the center line of the cable. The temperature is therefore assumed homogeneous in the cross-section of the cable.

Heat flux between the cables is taken into account, in the simulations, using the thermal network model. The interaction between the cable turns is represented by a matrix D. This matrix adds the information about the additional heat flux due to different turns, specifying how the elements are thermally connected to ones in the neighbouring turns. In the case that the
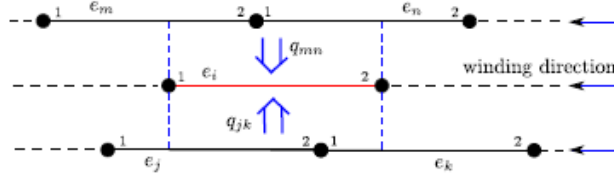
17

Figure 1.4: Top view: Depiction of the thermal network between the turns [69].

winding is made of only one layer, the matrix describe the heat flux between the turns is in one plane. Taking a look at an element in the 1-D modelling domain corresponding to the element e_i (see Fig. 1.4) in the 3-D domain, the heat flux q_i, to it from cable layers next to it is

$$q_i = -k_i \frac{T_i - T_{min}}{\Delta r} - k_i \frac{T_i - T_{jk}}{\Delta r} \qquad (1.14)$$

where k is the thermal conductivity, and Δr the thickness, of the insulation material between the cable turns. Furthermore, q_i is integrated along the width of the element e_i using the basis functions for the varying temperatures along the integration path in the involving elements. As a result of this integration, one gets coefficients for every element node and they together form the matrix D.

Further details about the quench and the detection analysis on the Father-M0 magnet (FM0) carried out with the described model are discussed in [69].

In the frame of the design study of a 10 T REBCO insert solenoid, developed for the NOUGAT [2] project, F. Borgnolutti, A. Badel *et al.* built an electric model of the whole HTS coil in order to understand and compare the electrical and thermal response of the No-Insulation (NI) and Metallic Insulation (MI) winding techniques to a sudden disruption of the power supply [71]. As shown in Fig. 1.5a, each turn of the winding is modelled as a wire loop made of an inductance (L_i) in series with a loop resistance (R_i). Practically, the loop resistance R_i is computed as the equivalent resistance of the parallel circuit made of the superconducting tape, characterized by the VI relation in the form of the power law with n = 20, and the resistance of the substrate and copper layers. The dependence of the tape critical current on temperature, transport current, magnetic field amplitude and angle with respect to the c-axis is taken into account using the same characterization than in [72]. The turn-to-turn contact resistance is modelled with a resistor (R_{ci}). Its value is derived from a turn-to-turn resistivity equal to $110\,\mu\Omega\,cm^2$ and $180\,m\Omega\,cm^2$ for the NI and MI winding, respectively. Resistivity values were obtained from discharge experiment performed on NI

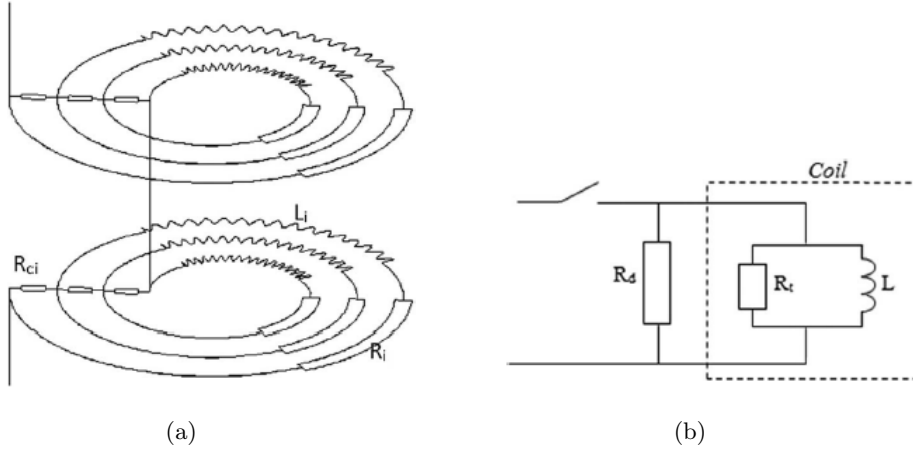[2]http://www.agence-nationale-recherche.fr/Project-ANR-14-CE05-0005

Figure 1.5: (a) Electrical model for an HTS double-pancake (in this example the pancake is made of 2×3 turns). Subscript i stand for the i-th turn [71]. (b) Simplified electric model of the HTS inset assuming that all the turns remain superconducting during the discharge. L is the magnet self-inductance and R_t is the sum of all the turn-to-turn resistances [71].

and MI pancakes [73] and [74]. The electric model also takes into account the mutual inductance between turns and temperature-dependent material properties. At the end of a time step the temperature of each turn is computed assuming no heat exchange between turns. An adaptive time step calculated as a fraction of the smallest time constant of the coil was used for the simulation. The inter-pancake joint resistance is not taken into account in the model.

In the event where all the turns remain superconducting during the discharge, i.e., $R_i = 0$ for all i, then the whole coil model of Fig. 1.5a can be reduced to the model of Fig. 1.5b where L is the total coil inductance, and R_t is the sum of all the R_{ci} [75]. The dump resistor R_d has the dual role to extract energy from the coil so as to reduce the amount of energy that is dissipated in the winding, thus lowering the hot spot temperature, and to limit the inductive peak voltage which develops at the beginning of the discharge. The latter is calculated as:

$$V_{peak} = R_t\, I_n \, \frac{1}{1 + \frac{R_t}{R_d}} \tag{1.15}$$

where I_n is the coil nominal current. The ratio between the energy dissipated in R_d (Q_{Rd}) and the total energy dissipated both in R_d and in R_t (Q_{Rt}) is given by:

$$\frac{Q_{Rd}}{Q_{Rd} + Q_{Rt}} = \frac{1}{\left(1 + \frac{R_d}{R_t}\right)} \tag{1.16}$$

19

The speed of the discharge is characterized by the time constant of the circuit, which is computed as:

$$\tau = \frac{L}{R_t}\left(1 + \frac{R_t}{R_d}\right) \tag{1.17}$$

1.6 Quench Modeling: Homogenized Models

The models based on a homogenization technique of the different materials that assemble a magnet allow to analyse large scale devices. As a matter of fact, the discretization of a single component or layer of a device makes the computational efforts exceedingly high. That disadvantage due to the use of this approach is that a homogenized coil model ignores the distribution of materials within the conductor and the magnet by considering only effective homogenized material properties. A model that homogenizes at the conductor level preserves the turn-to-turn conductor/insulation geometry but includes no details of the internal structure of the conductor. These models are often coupled with electrical circuits to model the dynamic current and the voltage changes during the process of quench detection and protection. Due to the homogenization, however, they provide only rough quench information and cannot evaluate phenomena within the conductor itself.

Several research groups applied these methodologies. The models developed by Philippe Masson [38] at the CAPS (Center for Advanced Power Sistem, US) and by Erkki Hato and Antti Stenvall *et al.* [39] [40] at the Tampere Univeristy of Technology and at CERN are discussed in the following sections.

As presented by Philippe Masson *et al.* in [38], an equivalent electrical resistance of the tape can be calculated. The current sharing is assumed to take place as soon as the YBCO layer, carrying all the current, becomes more resistive than the other layers. The transversal electrical resistances play an important role at short timescales that are not relevant to the proposed homogenized simulation. Therefore, the global simulation assumes the current to share based on the longitudinal values of the resistances of each layer and will not capture small time constant phenomena. Moreover, each turn of the coil is assumed to be perfectly electrically insulated using kapton film and no current can flow directly from one layer to another. The equivalent resistance along the tape can be calculated using a lumped-parameter equivalent circuit. The homogenized electrical resistance can then be calculated
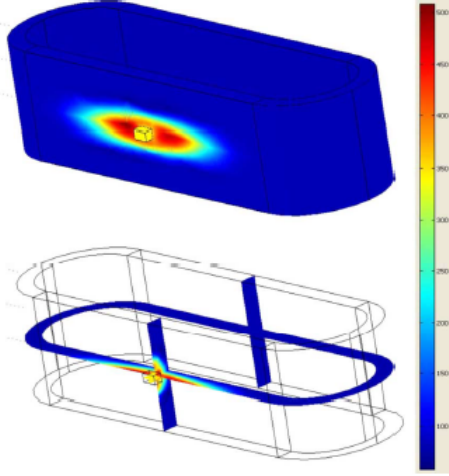
Figure 1.6: Quench propagation in the racetrack coil [38].

as follows

$$R_N = \frac{\prod_{i=1}^{N} R_i}{\sum_{j=1}^{N} \left(\prod_{k \neq j} R_k \right)} \tag{1.18}$$

The resistivity of YBCO is calculated using the equations in [77].

The model is implemented in the COMSOL Multiphysics environment and applied for the study of quench on a racetrack coil that is conduction cooled at 77 K from the inside wall. This type of coil could be used, for example, in the rotor of a superconducting synchronous machine. More results about the quench analysis and the normal zone propagation velocity in the racetrack coil described are discussed in [38].

A different model proposed by Etkki Harom, Antti Stenval *et al.* in [39] and [40], is based on a FEM software built on top of the open-source Gmsh. The software solves the heat diffusion equation where an anisotropic thermal conductivity and a volumetric heat capacity are taken in account. The Joule heat generation within the modelling domain was computed using the formulation $\rho \, || \, J \, ||^2$, where ρ is the effective resistivity of the cable and J the current density. Effective resistivity can be computed by assuming the materials of the cable as in parallel [78] and averaged over the volumetric fraction of the material. The superconductor resistivity was computed with the power law [79]-[80].

The model is applied for the calculation of the hot spot temperature [40] and minimum quench energy [39] for the HTS coil named Father-M0 (FM0) [70] and [81]. Father-M0 is the latest version of an HTS insert for future
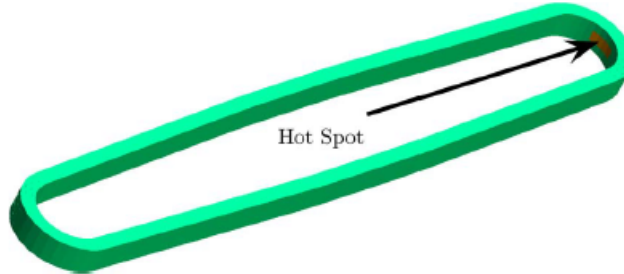
21

Figure 1.7: Modeling domain used for FEM simulations [40].

accelerator magnets in the EuCARD-2 project [70]. The FM0 magnet is designed to have five turns of Roebel cable made from 15 12-mm-wide REBCO tapes. The inner diameter of the magnet is 20 mm, the outer diameter is 25 mm, and the height is 12.2 mm. The operation current of the magnet is 6000 A. The location of the hot spot temperature as discussed in [40] is shown in Figure 1.7

1.7 Quench Modeling: Hierarchical Multiscale Models

As presented by Wan Kan Chan and Justin Schwartz, the hierarchical multiscale model described in [76] is based on an experimentally validated model of quenching in a REBCO CC tapes previously reported in [82]. This conductor model is an accurate micrometer-scale model that uses a mixed dimensional modeling approach to address the computational challenges of modeling a high-aspect-ratio multilayer system. The model includes all of the thin layers within a CC, including the REBCO layer, the thin silver and the buffer interlayers, which are addressed with 2D equations and internal 2D boundary conditions (BCs). The remaining relatively thick layers, including the stabilizer and the substrate, are modeled with 3D physics. The interior BCs also couple the 2D and 3D physics. The model can calculate the temperature and voltages within each layer as a function of location and time during a quench and acurately predicts the quench behavior observed in experiments, including the NZPV and the voltage and temperature profiles. Because each layer is modeled without any averaging of material properties, it is easy to model the effects of variations in architecture on the quench behavior, as reported in [83]. The multiscale model described in [76] uses the previously reported conductor model as its basic building block. Using the conductor model throughout an entire magnet, however, would be computationally prohibitive; hence the multiscale magnet model integrates the conductor model with a homogenized model of the entire magnet. Within
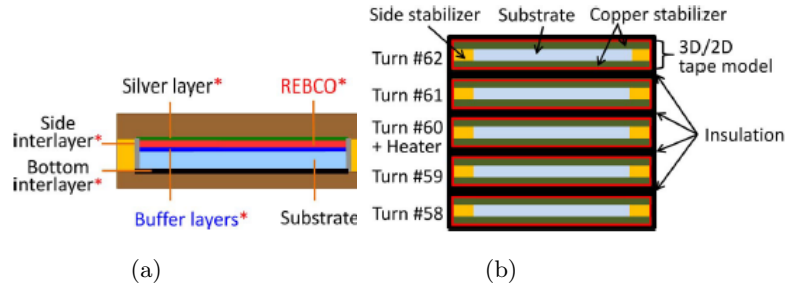
Figure 1.8: (a) Cross-sectional schematic of a typical REBCO CC as used in the model [82]. Starred layers are thin layers modeled with 2-D physics; all other layers are modeled in 3-D [76]. (b) Schematic showing the cross section of a multilayer tape module composed of five layers of CC [76].

the homogenized coil framework, one or more localized micrometer-scale multilayer tape modules are embedded at particular locations of interest. The locations of interest can be varied to account for location-dependent effects such as cooling conditions, the dependence of the critical current density on magnetic field and its orientation, or regions where larger heat loads are anticipated. For example, one localized multilayer tape module can be placed at the edge of the coil and another module at the center of the global homogenized coil. The multilayer module models a small section of the coil in detail and is also built using a hierarchical approach by integrating and coupling multiple single-layer CC tape modules that describe the behavior within each layer of the REBCO CC. The single-layer CC modules are separated by insulation layers that are also physically modeled.

The hierarchical multiscale approach is illustrated in Fig. 1.8a and Fig. 1.9. Fig. 1.8a illustrates a cross-sectional schematic of a typical CC tape model from [82], which is the fundamental building block of the model. These are stacked to create the multilayer modules as shown in Fig. 1.8b. The multilayer modules are then embedded in selected locations of an otherwise homogenized coil model as illustrated by the example shown in Fig. 1.9.

The model is aimed at investigating quench behavior of a coil carrying a direct transport current. In view of the slow NZPV in REBCO CC-based coils, the slowly varying time-derivative term of the magnetic potential is ignored, thereby decoupling the magnetic and electric potentials in Maxwell equations. The governing thermal, electrical and magnetic equations for the
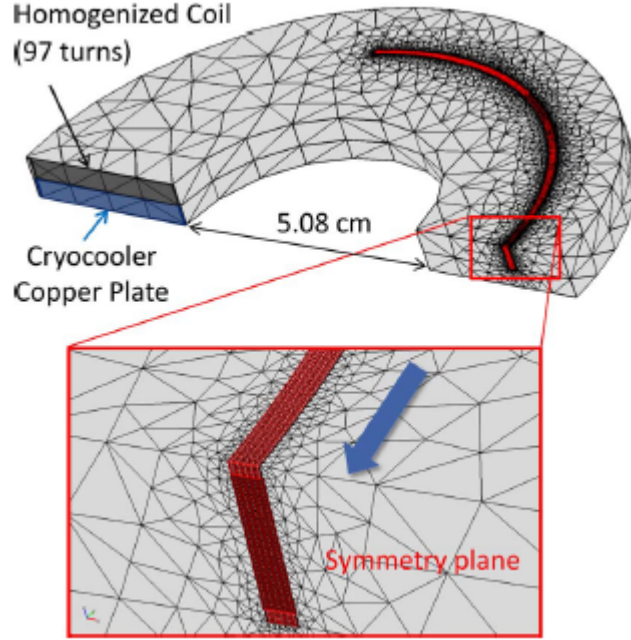
Figure 1.9: Multiscale coil model composed of a homogenized coil, a copper plate, and a localized embedded multilayer tape module. The inset shows a section of the multilayer tape module whose cross section is illustrated in Fig. 1.8b. The arrow shows the direction of the current flow in each turn. The current outflow ends of the tapes are located on the symmetry plane. The current inflow ends are located at the other end of the multilayer tape model. Not shown is the air region, which is a half-rectangle enclosing the half-cylinder coil model, used for the magnetic field calculation [76].

3D domains are then

$$\rho_\alpha\left(T\right) C_\alpha\left(T\right) \frac{\partial T}{\partial t} + \nabla \cdot \left(-K_\alpha\left(T\right)\right) = \mathbf{J} \cdot \mathbf{E} \qquad \text{in } \Omega_\alpha \qquad (1.19)$$

$$\nabla \cdot \left(-\sigma_\alpha\left(T\right) \nabla V\right) = 0 \qquad \text{in } \Omega_\alpha \qquad (1.20)$$

$$\mathbf{J} = \sigma_\alpha\left(T\right) \mathbf{E} \qquad \text{in } \Omega_\alpha \qquad (1.21)$$

$$\mathbf{E} = -\nabla V \qquad \text{in } \Omega_\alpha \qquad (1.22)$$

$$\nabla \times \frac{1}{\mu_0} \nabla \times \mathbf{A} = \mathbf{J} \qquad \text{in } \Omega_\alpha \qquad (1.23)$$

$$\nabla \times \frac{1}{\mu_0} \nabla \times \mathbf{A} = 0 \qquad \text{in } \Omega_{air} \qquad (1.24)$$

The externally applied current is input via a normal flux BC imposed on the current input end of the tape model.

The high-aspect-ratio thin layers, namely, the REBCO, silver, and buffer layers, are modeled with 2-D physics. On the REBCO layer, the thermal physics is approximated with a 2D tangential equation and is discretized

with 2D Lagrange finite elements. Similarly, the electric physics on the REBCO layer is approximated by a 2D tangential equation [82]. Finally, the electrical conductivity of REBCO is approximated by a nonlinear E-J power law equation.

The mutilayer tape module is built by stacking multiple tape models and/or configuring them side-to-side. Regardless of configuration, electrical insulation separates adjacent tapes (Fig. 1.8b illustrates a stack of tapes). The presence of electrical insulation between adjacent tapes is modeled with the same techniques used for a single tape, as described in [82]. For example, the insulation layers are modeled as two pairs of interior boundary conditions BCs (as identity-pair BCs, similar to the implementations of the silver and buffer layers previously mentioned), i.e. one for the thermal physics and the other for the electric.

Bibliography

[1] H. W. Weijers *et al.* "High Field Magnets With HTS Conductors," *IEEE Trans. Appl. Supercond., vol. 20, no. 3, pp. 576-579,2010.*

[2] W. D. Markiewicz, D. C. Larbalestier, H. W. Weijers, A. J. Voran, K. W. Pickard, W. R. Sheppard, J. Jaroszynski, A. Xu, R. P. Walsh, J. Lu, A. V. Gavrilin, P. D Noyes, "Design of a Superconducting 32 T Magnet With REBCO High Field Coils," *IEEE Trans. Appl. Supercond., vol. 22, no. 3, 2012.*

[3] L. Yan, "Recent Progress of Superconducting Magnet Technology in China," *IEEE Trans. Appl. Supercond., vol. 20, no. 3, pp. 123-134, 2010.*

[4] Gupta *et al.*, "High Field HTS R&D Solenoid for Muon Collider," *IEEE Trans. Appl. Supercond., vol. 21, no. 3, pp. 1884-1887, 2011.*

[5] H.W. Weijers *et al.*, "The NHMFL 32 T superconducting magnet," presented at the 13th European Conference on Applied Superconductivity EUCAS 2017, Geneva, Swiss, Sept. 1721, 2017.

[6] M. N. Wilson, Superconducting Magnets. Oxford, U.K.: Clarendon, 1983

[7] M. Oshima, R. J. Thome,W. R.Mann, and R. D. Pillsbury, "PQUENCH A 3-D quench propagation code using a logical coordinate system," *IEEE Trans. Magn., vol. 27, no. 2, pp. 20962099, Mar. 1991.*

[8] L. Rossi and M. Sorbi, "QLASA: A computer code for quench simulation in adiabatic multicoil superconducting windings," *Nat. Inst. Nucl. Phys., Rome, Italy, Tech. Rep. INFN/TC-04/13, 2004.*

[9] Y. Eyssa and M. Markiewicz, "Quench simulation and thermal diffusion in epoxy-impregnated magnet system," *IEEE Trans. Appl. Supercond., vol. 5, no. 2, pp. 487490, Jun. 1995.*

[10] Y. Eyssa, W. D. Markiewicz, and J. Miller, "Quench, thermal, and magnetic analysis computer code for superconducting solenoids," *IEEE Trans. Appl. Supercond., vol. 7, no. 2, pp. 159162, Jun. 1997.*

[11] A. P. Verweij, "CUDI: A model for calculation of electrodynamic and thermal behaviour of superconducting Rutherford cables," *Cryogenics, vol. 46, no. 8, pp. 619626, Jul./Aug. 2009.*

[12] G. A. Levin, W. A. Jones, K. A. Novak, and P. N. Barnes, "The effects of superconductor-stabilizer interfacial resistance on quenching of a pancake coil made out of coated conductor," *Supercond. Sci. Technol., vol. 24, no. 3, p. 035015, Mar. 2011.*

[13] A. Ishiyama, H. Ueda, T. Ando, H. Naka, S. Bamba, and Y. Shiohara, "A criterion for determining stabilizer thickness of YBCO coated conductors based on coil protection," *IEEE Trans. Appl. Supercond., vol. 17, no. 2, pp. 24302433, Jun. 2007.*

[14] A.L. Rakhmanov, V.S. Vysotsky, Yu. Ilyin, T. Kiss, M. Takeo "Influences of voltagecurrent characteristic difference on quench development in low-Tc and high-Tc superconducting devices (Review)," *Physica C 401 (2004) 5765*

[15] V.S. Vysotsky, A.L. Rakhmanov, Yu. Ilyin, "Universal scaling law for quench development in HTSC devices," *Physica C 401 (2004) 5765*

[16] A. M. Miri, C. Sihler, M. Droll, and A. Ulbricht, "Modeling the transient behavior of a large superconducting coil subjected to high voltage pulses," *in Proc. Int. Conf. Power Syst. Transients, Lisbon, Portugal, 1995, pp. 5762.*

[17] A. M. Miri, S. Fink, and W. H. Fietz, "Transient behaviour of superconducting magnet systems of fusion reactor ITER during safety discharge," *Modelling Simul. Eng., vol. 2008, p. 359210, 2008.*

[18] D. Bocian, B. Dehning, and A. Siemko, "Modeling of quench limit for steady state heat deposits in LHC magnets," *IEEE Trans. Appl. Supercond., vol. 18, no. 2, pp. 112115, Jun. 2008.*

[19] Tao Wang, So Noguchi, Xudong Wang, Issei Arakawa, Katsuhiko Minami, Katsutoshi Monma, Atsushi Ishiyama, Seungyong Hahn, and Yukikazu Iwasa, "Analyses of Transient Behaviors of No-Insulation REBCO Pancake Coils During Sudden Discharging and Overcurrent," *IEEE Trans. Appl. Supercond., vol. 25, no. 3, pp. 46034094603409, Jun. 2015.*

[20] Kazuki Katsumata, Tao Wang, Atsushi Ishiyama, So Noguchi, Katsutoshi Monma, Shigeo Nagaya, and Tomonori Watanabe, "Influence of the Turn-to-Turn Contact Electrical Resistance on the Thermal Stability in Meter-Class No-Insulation REBCO Pancake Coils During a Local Normal-State Transition," *IEEE Trans. Appl. Supercond., vol. 27, no. 4, pp. 4602005, Jun. 2017.*

[21] So Noguchi, Ryosuke Miyao, Katsutoshi Monma, Hajime Igarashi, Hiroshi Ueda, and Atsushi Ishiyama, "Current Behavior Simulation in Stacked NI REBCO Pancake Coils During Local Normal-State Transition," *IEEE Trans. Appl. Supercond., vol. 27, no. 4, pp. 4603205, Jun. 2017.*

[22] So Noguchi, Ryosuke Miyao, Katsutoshi Monma, Hajime Igarashi, and Atsushi Ishiyama, "Numerical Investigation of Metal Insulation Technique on Turn-to-Turn Contact Resistance of REBCO Pancake Coils," *IEEE Trans. Appl. Supercond., vol. 27, no. 4, pp. 7700505, Jun. 2017.*

[23] Tao Wang, Kazuki Katsumata, Atsushi Ishiyama, and So Noguchi, "Detection Method for a Local Normal-State Transition in a No-Insulation REBCO Pancake Coil," *IEEE Trans. Appl. Supercond., vol. 27, no. 4, pp. 0601206, Jun. 2017.*

[24] Takahiro Oki, Aika Ikeda, TaoWang, Atsushi Ishiyama, So Noguchi, Katsutoshi Monma, TomonoriWatanabe, and Shigeo Nagaya, "Evaluation on Quench Protection for No-Insulation REBCO Pancake Coil," *IEEE Trans. Appl. Supercond., vol. 67, no. 4, pp. 4702905, Jun. 2016.*

[25] So Noguchi, Katsutoshi Monma, Sadanori Iwai, Hiroshi Miyazaki, Taizo Tosaka, Shunji Nomura, Tsutomu Kurusu, Hiroshi Ueda, Atsushi Ishiyama, Shinichi Urayama, and Hidenao Fukuyama, "Experiment and Simulation of Impregnated No-Insulation REBCO Pancake Coil," *IEEE Trans. Appl. Supercond., vol. 26, no. 4, pp. 4601305, Jun. 2016.*

[26] Aika Ikeda, Takahiro Oki, TaoWang, Atsushi Ishiyama, Katsutoshi Monma, So Noguchi, TomonoriWatanabe, and Shigeo Nagaya, "Transient Behaviors of No-Insulation REBCO Pancake Coil During Local Normal-State Transition," *IEEE Trans. Appl. Supercond., vol. 26, no. 4, pp. 4600204, Jun. 2016.*

[27] N. Schwerg, B. Auchmann, and S. Russenschuck, "Quench simulation in an integrated design environment for superconducting magnets," *IEEE Trans. Magn., vol. 44, no. 6, pp. 934937, Jun. 2008.*

[28] Z. P. Zhao and Y. Iwasa, "Normal zone propagation in adiabatic superconducting magnets. Part 1: Normal zone propagation velocity in superconducting composites," *Cryogenics, vol. 31, no. 9, pp. 817825, Sep. 1991.*

[29] V. Picaud, P. Hiebel, and J.-M. Kauffmann, "Superconducting coils quench simulation, the Wilsons method revisited," *IEEE Trans. Magn., vol. 38, no. 2, pp. 12531256, Mar. 2002.*

[30] K. Koyanagi, M. Ono, S. Hanai, K. Watanabe, S. Awaji, T. Hamajima, T. Kiyoshi, and H. Kumakura, "Design of a 30 T superconducting magnet using a coated conductor insert," *IEEE Trans. Appl. Supercond., vol. 19, no. 3, pp. 16171620, Jun. 2009.*

[31] M. Ristic, J. V. M. McGinley, and F. Lorenzoni, "Numerical study of quench protection schemes for a MgB2 superconducting magnet," *IEEE Trans. Appl. Supercond., vol. 21, no. 5, pp. 35013508, Oct. 2011.*

[32] L. Wang, H. Pan, X. L. Guo, H. Wu, S. X. Zheng, and M. A. Green, "Study on the mechanical instability of MICE coupling magnets," *IEEE Trans. Appl. Supercond., vol. 21, no. 3, pp. 23632366, Jun. 2011.*

[33] K. Higashikawa, T. Kiss, M. Inoue, S. Awaji, K.Watanabe, H. Fukushima, Y. Yamada, and Y. Shiohara, "Significant reduction in volume, stored energy and magnetization loss of high-field magnet coil based on the improvement of critical current characteristics in GdBCO coated conductor," *Phys. C-Supercond. Appl., vol. 469, no. 15, pp. 17761780, Aug.Oct. 2009.*

[34] A. Stenvall, R. Mikkonen, and P. Kovac, "Relation between transverse and longitudinal normal zone propagation velocities in impregnated MgB2 windings," *IEEE Trans. Appl. Supercond., vol. 19, no. 3, pp. 24032406, Jun. 2009.*

[35] X. Du, M. Jin, Z. Zhang, Z. Xu, L. Ye, D. Zhang, X. Li, G. Zhang, and L. Xiao, "Numerical analysis on the quench process and protection of conduction cooled MgB2 magnet," *IEEE Trans. Appl. Supercond., vol. 20, no. 3, pp. 21022106, Jun. 2010.*

[36] P. Ferracin, S. Caspi, L. Chiesa, S. A. Gourlay, R. R. Hafalia, L. Imbasciati, A. F. Lietzke, G. Sabbi, and R. M. Scanlan, "Thermal, electrical and mechanical response in Nb3Sn superconducting coils," *IEEE Trans. Appl. Supercond., vol. 14, no. 2, pp. 361364, Jun. 2004.*

[37] A. Ishiyama, H. Matsumura, W. Takita, and Y. Iwasa, "Quench propagation analysis in adiabatic superconducting windings," *IEEE Trans. Magn., vol. 27, no. 2, pp. 20922095, Mar. 1991.*

[38] P. J. Masson, V. R. Rouault, G. Hoffmann, and C. A. Luongo, "Development of Quench Propagation Models for Coated Conductors", *IEEE Trans. Appl. Supercond., vol. 20, no. 2, pp. 1321-1324, 2008.*

[39] E. Hr, A. Stenvall, J. van Nugteren, and G. Kirby, "Modeling of Minimum Energy Required to Quench an HTS Magnet With a Strip Heater," *IEEE Trans. Appl. Supercond., vol. 25, no. 6, pp. 47015054701505, 2015.*

[40] E. Hr, A. Stenvall, J. van Nugteren, and G. Kirby, "Hot Spot Temperature in an HTS Coil: Simulations With MIITs and Finite Element Method," *IEEE Trans. Appl. Supercond., vol. 25, no. 5, pp. 49011074901107, 2015.*

[41] L. Bottura, "Quench Analysis of Superconducting Magnets. A numerical Study." *Ph.D Thesis, EUR-FU/XII/185/93, April 1993.*

[42] P. Bruzzone, "The index n of the voltagecurrent curve, in the characterization and specification of technical superconductors," *Physica C 401 (2004) 714.*

[43] J. Baixeras, G. Fournet, "Pertes par deplacement de vortex dans un supraconducteur de type II non ideal" *Phys.Chem.Solids 28 (1967) 1541.*

[44] C.R. Walter, Brookhaven National Laboratory Informal Report BNL 18928 (AADD 74-2) 30-1, 1974.

[45] L.F.Goodrich, F.R.Fickett "Critical current measurements: A compendium of experimental results," *Volume 22, Issue 5, May 1982, Pages 225-241*

[46] M. Polk, M. Majoros, "Influence of Cu-Ni matrix on a.c. losses and voltage-current characteristics of fine filament Nb-Ti superconductors," *Cryogenics 27 (1987) 545.*

[47] W.W. Webb, J. Appl. Phys. 42 (1) (1971) 107.

[48] W.W. Webb, "Evidence Against Thermal Activation as the Cause of Flux Creep in Type II Superconductors" *J. Appl. Phys. 42 (1) (1971) 107.*

[49] M. Polak, I. Hlasnik, L. Krempasky, Cryogenics 13 (1973) 702.

[50] G.L. Dorofejev, A.B. Imenitov, E.Yu. Klimenko, Cryogenics 20 (1980) 307.

[51] Decroux M, Antognazza L, Musolino N, de Chambrier E, Reymond S, Triscone J M, Fischer O, Paul W and Chen M "Properties of YBCO films at high current densities: fault current limiter implications" *IEEE Trans. Appl. Supercond., vol. 1, no. 1, pp. 20462049, 2001.*

[52] A.L. Rakhmanov, V.S. Vysotsky, Yu.A. Ilyin, *et al.*,"Universal scaling law for quench development in HTSC devices," *Cryogenics 40 (1) (2000) 19.*

[53] V.S. Vysotsky, Yu.A. Ilyin, T. Kiss, *et al.*, "Thermal quench study in HTSC pancake coil" *Cryogenics 40 (1) (2000) 9.*

[54] V.S. Vysotsky, Yu.A. Ilyin, A.L. Rakhmanov, "Stability and quench development in HTS magnet: influence of cooling and material parameters" *Adv. in Cryog. Eng. 47 (2002) 481.*

[55] Yu. A. Ilyin, Ph.D. Thesis, Kyushu University, Fukuoka, Japan, 2000.

[56] Yu.A. Ilyin, V.S. Vysotsky, T. Kiss, *et al.*, "Stability and quench development study in small HTSC magnet," *Cryogenics 41 (9) (2001) 665.*

[57] Yu. Lvovsky, "Limiting Length in Cooling Design of HTS Magnets," *IEEE Trans. Appl. Supercond. 10 (1) (2000) 1840.*

[58] V.S. Vysotsky, Yu.A. Ilyin, A.L. Rakhmanov, M. Takeo, "Quench development analysis in HTSC coils by use of the universal scaling law," *IEEE Trans. Appl. Supercond 11 (1) (2001) 1824.*

[59] A.C. Rose-Innes, E.H. Rhoderick, Introduction to Superconductivity, Pergamon Press, Oxford, 1969.

[60] A. V. Gavrilin, A. V. Dudarev, and H. H. J. ten Kate, "Quench Modeling of the ATLAS Superconducting Toroids," *IEEE Trans. Appl. Supercond., vol. 11, no. 1, pp. 1693, 2011.*

[61] A. V. Gavrilin, N. Yauagi, S. Imagawa, T. Mito, A. Iwamoto, H. Chikaraishi, S. Hatnaguchi, A. Nishimura, T. Satow, Y. Nakamura, S. Satoh, O. Motojirna, "Analysis of the Normal Transition Event of the LHD Helical Coils," *IEEE Trans. Appl. Supercond., vol. 10, no. 1, pp. 610, 2000.*

[62] A. V. Gavrilin and A. A. Konyukhov, "Computer Simulation and Experimental Study of Quench in Superconducting Epoxy-Impregnated Multi-Layer Coil," *IEEE Trans. Appl. Supercond., vol. 32, no. 4, pp. 2990, 1996*

[63] A. V. Gavrilin, "Computer Simulation of Thermal Process During Quench in Superconducting Winding of Solenoid," *IEEE Trans. Appl. Supercond., vol. 3, no. 1, pp. 293, 1993*

[64] A. V. Gavrilin *et al.*, "Comprehensive quench analysis of the NHMFL 32T all-superconducting magnet," presented at the CHATS Appl. Supercond. 2015, Bologna, Italy, Sep. 1416, 2015.

[65] A. V. Gavrilin *et al.*, "Comprehensive modelling study of quench behaviour of the NHMFL 32 T all-superconducting magnet system. Input data and methodology aspects," presented at the 5th Int. Workshop Numer. Modelling High Temp. Supercond. 2016, Bologna, Italy, Jun. 1517, 2016. [Online]. Available: https://events.unibo.it/htsmodelling2016/program

[66] N. Gvozdenovic, L. W. Mayer, C. F. Mecklenbrauker, and A. L. Scholtz, "PEEC modeling of circular spiral coils," *in Proc. Eur. IEEE Microw. Conf., Nuremberg, Germany, 2013, pp. 11031106.*

[67] S. Noguchi, R Itoh, S. Hahn, and Y. Iwasa, "Numerical simulation of superconducting coil wound with no-insulation NbTi wire," *IEEE Trans. Appl. Supercond., vol. 24, no. 3, Jun. 2014, Art. ID. 4900504.*

[68] K. Yamafuji and T. Kiss, "A new interpolation of the glass-liquid transition of pinned fluxoids in high-Tc superconductors," *Phys. C, Supercond.,vol. 258, no. 34, pp. 197212, Feb. 1996.*

[69] Janne Ruuskanen, Antti Stenvall, and Valtteri Lahtinen, "Predicting Heat Propagation in Roebel-Cable-Based Accelerator Magnet Prototype: One-Dimensional Approach With Coupled Turns," *IEEE Trans. Appl. Supercond., vol. 27, no. 4, pp. 0600205, 2017 .*

[70] G. Kirby *et al.*, "Accelerator quality HTS dipole magnet demonstrator designs for the EuCARD-2, 5 tesla 40 mm clear aperture magnet," *IEEE Trans. Appl. Supercond., vol. 25, no. 3, Jun. 2015, Art. ID. 4000805.*

[71] F. Borgnolutti, A. Badel, T. Benkel, X. Chaud, F. Debray, P. Fazilleau, T. Lecrevisse, and P. Tixador, "Design Study of a 10-T REBCO Insert Solenoid," *IEEE Trans. Appl. Supercond., vol. 26, no. 4, p. 4600404, 2016.*

[72] J. Fleiter and A. Ballarino, "Parameterization of critical surface of REBCO conductors from Fujikura," CERN, Geneva Switzerland, Internal Note, EDMS: 1426239, Sep. 2014.

[73] T. Lcrevisse and Y. Iwasa, "A (re)bco pancake winding with metal as insulation," presented at the 12th European Conference on Applied Superconductivity, Lyon, France, Sep. 610, 2015.

[74] K. L. Kim et al., "Effect of winding tension on electrical behaviors of a no-insulation ReBCO pancake coil," *IEEE Trans. Appl. Supercond., vol. 24, no. 3, Jun. 2014, Art. ID 4600605.*

[75] X. wang et al., "Turn-to-turn contact characteristics for an equivalent circuit model of no-insulation ReBCO pancake coil," *Supercond. Sci. Technol., vol. 26, no. 3, Jan. 2013, Art. ID 035012.*

[76] W. K. Chan, J. Schwartz, "A Hierarchical Three-Dimensional Multiscale Electro-MagnetoThermal Model of Quenching in REBa2Cu3O7 Coated-Conductor-Based Coils," *IEEE Trans. Appl. Supercond., vol. 22, no. 5, pp. 47060104706010, 2012.*

[77] X.Wang *et al.*, "Normal zone initiation and propagation in Y-Ba-Cu-O coated conductors with Cu stabilizer," *IEEE Trans. Appl. Supercond., vol. 15, no. 2, pp. 25862589, 2005.*

[78] A. Stenvall, A. Korpela, R. Mikkonen, and G. Grasso, "Stability considerations of multifilamentary MgB2 tape," *Supercond. Sci. Technol., vol. 19, pp. 184189, 2006.*

[79] J. Lehtonen, R. Mikkonen, and J. Paasi, "A numerical model for stability considerations in HTS magnets," *Supercond. Sci. Technol., vol. 13, pp. 251258, 2000.*

[80] P. Bruzzone, "The index n of the voltage-current curve, in the characterization and specification of technical superconductors," *Phys. C, Supercond., vol. 401, no. 4, pp. 714, Jan. 2004.*

[81] J. van Nugteren *et al.*, "A study of a 5 T research dipole insert-magnet using an anisotropic ReBCO Roebel cable," *IEEE Trans. Appl. Supercond., vol. 25, no. 3, Jun. 2015, Art. ID 4000705.*

[82] W. K. Chan, P. J. Masson, C. Luongo, and J. Schwartz, "Threedimensional micrometer-scale modeling of quenching in high aspect ratio YBa2Cu3O7 coated conductor tapes. Part I: Model development and validation," *IEEE Trans. Appl. Supercond., vol. 20, no. 6, pp. 23702380, Dec. 2010.*

[83] W. K. Chan and J. Schwartz, "Three-dimensional micrometer-scale modeling of quenching in high-aspect-ratio YBa2Cu3O7 coated conductor tapes; Part II: Influence of geometric and material properties and implications for conductor engineering and magnet design," *IEEE Trans. Appl. Supercond., vol. 21, no. 6, pp. 36283634, Dec. 2011.*

31

Chapter 2

Analysis of Quench in the R&D Prototype Coils for the 32 T Magnet: Prototype #1

2.1   Introduction

The 32-T all-superconducting user magnet system presently under test at the National High Magnetic Field Laboratory (NHMFL), US [1], is composed of two series-connected nested high-field HTS inner coils (insert) pancake wound with SuperPower REBCO tapes and a low-temperature superconducting (LTS) outsert magnet composed of five coils broken in 17 electric sections [1], [2]. More details about the magnet configuration and quench tests are discussed in the chapter 4.

In the frame of the R&D activity for the 32-T magnet project, different prototype coils are tested to analyse the quench initiation, propagation and protection of the real 32-T magnet. The first prototype is a foretype of the real insert of the 32-T magnet and in this chapter, an alternative modelling technique is presented and applied to analyse the quench prototype, as discussed in [3]. The model describes the magnet structure with a FEM approach, in which the magnet is split into its constituting pancakes connected through lumped thermal resistances. Each pancake is modelled by means of a 2D FEM-model approach, and its thermal evolution in time during a quench affects the other pancakes by means of the thermal contact distributed over the pancake interfaces. This modelling approach allows a very significant reduction of computation time with respect to a fully 3D computation.

In this chapter, the electromagnetic and electro-thermal stability is studied through a quasi 3D FEM model for the first prototype coils wound in the frame of the 32-T magnet project. In the first prototype, heater spacers located on the pancakes that assemble the prototypes are fired in quench

Table 2.1:
GEOMETRIC PROPERTIES OF TAPE AND INSULATION

Tape geometrical properties		
	Thickness [μm]	**Width** [mm]
Copper (bottom)	50	4.12 ± 0.02
Silver (bottom)	1.8	4.00 ± 0.01
Hastelly C276	50	4.00 ± 0.01
Buffer Layer	0.2	4.00 ± 0.01
REBCO	1.0	4.00 ± 0.01
Turn to turn insulation		
	Thickness [μm	**Width** [mm]
Stainless Steel	25	4.01 ± 0.001
Sol-gel alumina	12	4.01 ± 0.001

case. An alternative modelling technique is delivered and applied to analyse magnets wound with different pancakes connected in series.

The numerical simulations allow one to describe the main features of the quench experiments, such as the increasing coil resistance due to the expansion of a normal zone and the consequent damping of the prototype magnet current. Moreover, the simulations clarify the contributions of the various pancakes to the total coil resistance, showing the relative impact of the magnetic field intensity, higher in the central pancakes, and of the angle between the REBCO tapes and the field direction, which decreases the critical current density, especially in the terminal pancakes. The model finally gives an insight into the modes of propagation of the quench front in the radial, azimuthal and axial directions during these quench tests.

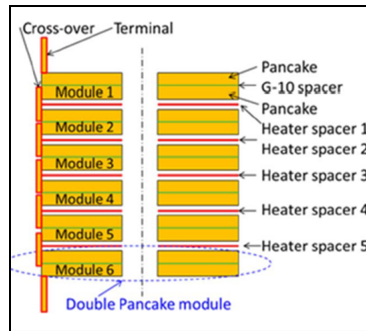## 2.2 Prototype Coil #1 and Experimental Test

Figure 2.1: Sketch of the complete NHMFL prototype coil with double pancake architecture [1].
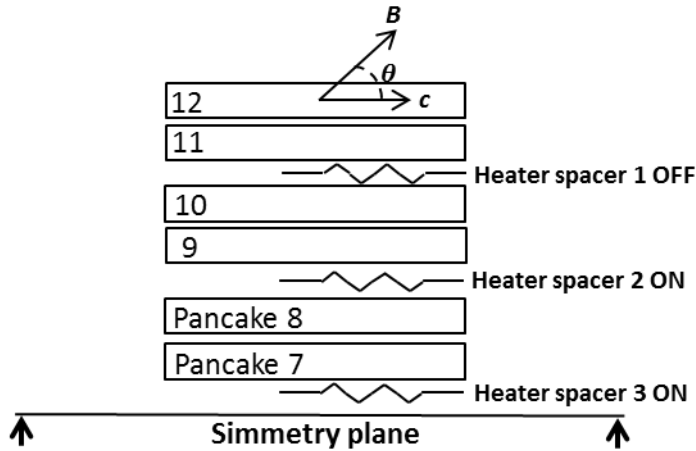
Figure 2.2: Sketch of the simulated portion of the prototype coil: the magnetic field and the heat distribution are symmetric with respect to the central heater spacer (heater spacer 3).
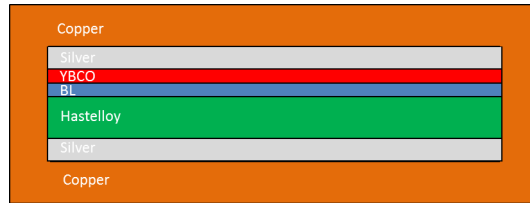

Figure 2.3: Sketch of the cross section of the SuperPower SCS4050 tape used for the NHMFL prototype (not in scale).

The NHMFL prototype coil consists of six double pancake modules, sketched in Fig. 2.1 and in Fig. 2.2. Each module is made of about 244 turns of YBCO tape SCS4050 manufactured by Superpower Inc.. In this configuration, shown in Fig. 2.3, the copper layer completely surrounds the other tape layers. The main properties of the tape are reported in Table 2.1. The turn-to-turn reinforcement is provided by stainless steel cowind (25 m), and electrical insulation by a 6 m alumina layer per side [4]. The pancakes are separated from each other with a G10 layer for electrical stand-off, whereas the modules are separated with heater spacers [5] able to apply external heat disturbances to the coils. The main geometric properties of the pancakes of the prototype coil are reported in Table 2.2. All quench tests were performed at 4.2 K in self-field and in a background magnetic flux density of 15 T generated by a large bore resistive magnet of the NHMFL [6]. In the beginning of the quench tests, the prototype coil was energized up to a 200 A constant current. In the quench experiments analysed here only the heaters of the heater spacers 2, 3 and 4 shown in Fig. 2.2 were used. For each heater spacer, two out of three heaters (see Fig. 2.4) were simulta-

Table 2.2:
GEOMETRIC PROPERTIES OF THE PROTOTYPE COIL

	Inner Radius [mm]	Outer Radius [mm]
Free bore	0	17.4
SS bore tube	17.4	18.75
G-10 winding mandrel	18.8	20
Winding inner radius	20	70
SS Overbanding	70	71

neously fired with a variable current up to the value that drives the quench of the prototype coil. The duration of the heater current pulses was set to 0.8 s. After quench initiation, the coil energy was discharged across the normal zones without energy extraction via external dump resistors. The coil current and overall coil resistance were measured during the dump and used for comparison with the results of the numerical model. Further details on these experiments are provided in [1].

2.3 Model Description

The coupled thermal and electromagnetic model was developed with a FEM approach in the COMSOL Multiphysics environment [7]. The constitutive block of the model is a tape model previously developed and validated both for individual tape and for cable analysis [8], [9]. The unknowns of the problem are the temperature and voltage over each pancake during the quench development. The model consists of three main parts, namely the thermal model, the electrical model and the computation of the magnetic flux density distribution over the prototype coil, which are described in detail in the next sections.

2.3.1 Thermal Model

As already mentioned, the prototype coil consists of twelve pancakes arranged in an array of six modules. The winding made from the superconducting tape and alumina plated stainless steel strip is represented through a single homogenous material, with anisotropic physical properties determined with a homogenization procedure.

Given the planar symmetry of the prototype coil with respect to its central plane (see Fig. 2.2), only the six pancakes of the upper part of the coil were described in the model. Moreover, since for each of the three heater spacers used in the experiments only two heaters were fired simultaneously, an additional symmetry condition for the problem can be applied to reduce the number of degrees of freedom. The symmetry plane in this case is the one in the middle angular position between heaters 1 and 3 (see Fig. 2.4).
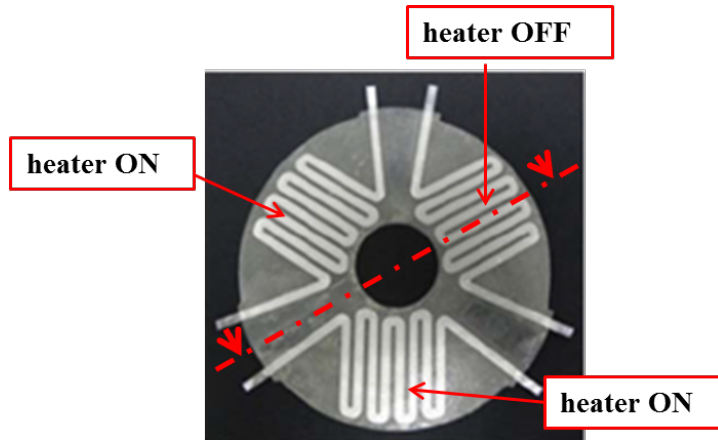
Figure 2.4: Picture of the three heaters mounted on each module: two of them are fired in the quench tests analysed in this work. The quench development is symmetric with respect to the axis reported in the plot.
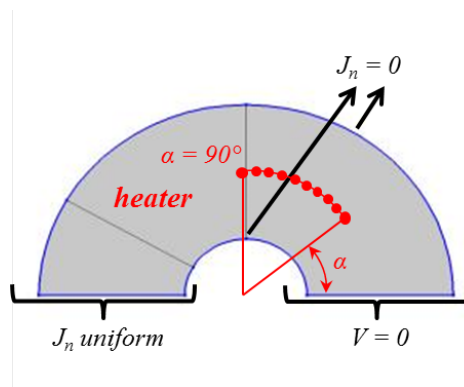

Figure 2.5: This symmetry is represented by appropriate boundary conditions on the electromagnetic model as reported in the figure, where J_n is the component of the current density vector orthogonal to the boundary surfaces. The points considered for the calculation of NZPV are located between the inner and outer radius of the pancake, at different angles with respect to the horizontal axis.

The thermal model is based on the heat balance equations written under the assumption that the temperature is uniform over the height of each pancake. Each pancake is therefore treated as a 2D electrical and thermal element, able to exchange heat with the adjacent pancakes by means of a distributed thermal contact resistance related to the thermal barrier of the G10 layer (RG10) and the interface resistance between the pancake and the G10 layer (R_{cz}). No current transfer is allowed between pancakes, due to the electrical insulation. A conceptual sketch of this modelling approach is illustrated in Fig. 2.6. In the actual implementation in the COMSOL Multiphysics environment only one 2D pancake is modelled and discretized with a mesh. At each mesh point, a set of heat balance equations is written for
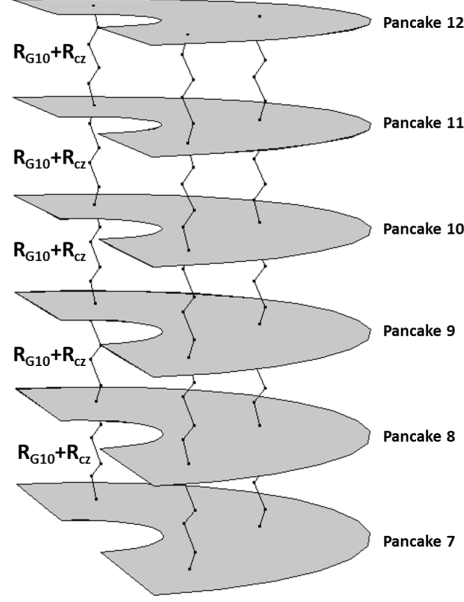
Figure 2.6: Conceptual sketch of the model of the various pancakes described as 2D elements connected via thermal distributed resistances. RG10 is the G10 thermal resistance between pancakes which depends on the G10 layer thickness, R_{cz} is the thermal interface resistance between each pancake and the G10 layer.

an array of temperatures at each mesh point representing the temperatures of all pancakes at that location.

These equations account for heat conduction in the radial and azimuthal directions in the 2D plane of each pancake, heat conduction in the axial direction towards adjacent pancakes, heat generation from the Joule effect, and external power deposition from the heaters. The equations can be written as follows for the i-th pancake ($i = 7, .., 12$):

$$\rho C p \left(T_i(x,y,t)\right) \frac{\partial T_i(x,y,t)}{\partial t} - \nabla \cdot \left(\mathbf{K}\left(T_i(x,y,t)\right) \nabla T_i(x,y,t)\right) =$$
$$= \sigma\left(T_i(x,y,t), B_i(x,y,t), E_i(x,y,t)\right) \cdot \nabla V_i(x,y,t) \cdot \nabla V_i(x,y,t) +$$
$$+ Q_i^z(x,y,t) + Q_i^{heater}(x,y,t) \qquad (2.1)$$

where $T_i(x,y,t)[K]$ is the temperature in the i-th pancake as a function of the position in the pancake plane, $\rho(kg/m^3)$ the homogenized density, $C_p(T_i)[J/(kgK)]$ the temperature dependent homogenized specific heat, $\mathbf{K}(T_i)$ the tensor of anisotropic thermal conductivity, $\sigma(T_i, B_i, E_i)$ the tensor of anisotropic electrical conductivity as a function of temperature T_i, magnetic flux density B_i and electric field E_i, V_i is the electric scalar potential in the i-th pancake. In the heat balance equation system, the axial thermal

37

exchange between the i-th pancake and the two adjacent pancakes is considered:

$$Q_i^z(x,y,t) = \frac{T_{i+1}(x,y,t) - T_i(x,y,t)}{V_P\left(R_{G10}^{i,i+1} + R_{cz}\right)} - \frac{T_i(x,y,t) - T_{i-1}(x,y,t)}{V_P\left(R_{G10}^{i,i-1} + R_{cz}\right)}$$

where V_P is the pancake volume, $R_{i,i-i}^{G10}$ is the G10 thermal resistance between pancakes i and $i1$, which depends on the G10 layer thickness, R_{cz} is the thermal interface resistance between each pancake and the G10 layer.

The heater pulse power $Q_i^{heater}(x,y,t)$ is input only on the pancakes where the heaters are fired and only on a $55°$ sector angle area corresponding to the heater surface. Since a part of the heater power does not actually enter the pancake, only a fraction of the total power was taken as an input. The effective heat flux from the heater was calculated beforehand using a detailed model [10] and was slightly modified by a fitting of the experimental data. The selected fraction is about 90% of the computed heater pulse

As boundary conditions of the problem, adiabatic conditions are assumed at the external surfaces. This choice is motivated by previous analyses reported in [1]. As a matter of fact, a helium bubble formation may significantly hinder the heat exchange to liquid helium, with a strong reduction of the heat transfer coefficient. This bubble formation is due to the fact that the peak field field-gradient product $(B_z dB_z/dz)$ can exceed the limit for trapping helium gas $(2100\,\mathrm{T}^2/\mathrm{m}^1)$ [11].

As for the initial conditions, a uniform temperature distribution set to 4.2 K was assumed for the whole prototype coil.

2.3.2   Electric Model

The electromagnetic model of the coil is based on the current density continuity condition:

$$\nabla \cdot \mathbf{J}_i = 0 \tag{2.2}$$

where $\mathbf{J}_i$ is the current density vector in the i-th pancake. As for the thermal model, the equation is solved for an array consisting of the current densities in each pancake as components.

The current density continuity conditions have been implemented in the FEM model, setting one for each pancake-i ($i = 7,.., 12$):

$$\nabla \cdot (-\sigma(T_i(x,y,t), B_i(x,y,t), E_i(x,y,t))\nabla V_i) = 0 \tag{2.3}$$

where σ is the 2D anisotropic homogenous electrical conductivity of the winding.

Boundary conditions of the electric problem are illustrated in Fig. 2.5. A zero voltage Dirichlet condition is applied to the inlet terminal of the coil. A uniform current density is imposed at the outlet terminal. A null current

density along the normal direction is imposed on all the other coil external surfaces. The adjacent pancakes are also electrically insulated with the G10 plates, so that no current flow is allowed in the model in axial direction.

2.3.3 Magnetic Flux Density Calculation

The calculation of the magnetic flux density generated by the prototype coil (self field) and by the large bore resistive magnet of the NHMFL (background field) were computed through a 3D semi-analytical approach [12]. The total magnetic flux density is axially symmetric with respect to the prototype coil axis. The radial and axial components of the magnetic flux density vector were computed at each point of the mesh in the finite element discretization during the simulations. The magnetic flux density depends on a constant component related to the background field and a coil current dependent component related to the self-field:

$$B_i^r = b_i^r(x_i, y_i) \quad I_{coil} + B_{i,ext}^r \qquad \forall i = 7, \cdots, 12 \qquad (2.4)$$

$$B_i^z = b_i^z(x_i, y_i) \quad I_{coil} + B_{i,ext}^z \qquad \forall i = 7, \cdots, 12 \qquad (2.5)$$

The coefficients b_i^r and b_i^z were computed before the dynamic simulations for each mesh point with an unit current flowing in the coil, and then utilized to determine the field and field angle dependent critical current density during the time dependent simulations. As shown in Fig. 2.7, the tape critical current exhibits a strong dependence on the angle θ (see Fig. 2.2) between the magnetic flux density vector and the c-axis [13]. Thus, the tape orientation with respect to the magnetic field has to be taken into account in full. Due to geometric tolerances and the non-perfectly rectangular cross section of the tape, its c-axis may not be perfectly perpendicular to the axis of the prototype coil. Thus, in the calculation of the angle between the c-axis and the field a tilt angle correction parameter was introduced [10].
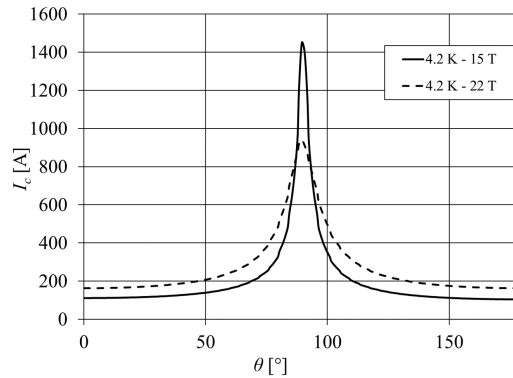

Figure 2.7: Dependence of the YBCO tape critical current at $4.2\,\mathrm{K}$ on the field angle with the tape c-axis..

2.3.4 Coil Constitutive Law

In order to close the system of equations required to describe the whole prototype coil during a quench, the constitutive law of the coil itself has to be taken into account. As a matter of fact, the resistance of the normal zone determines the damp of the coil current during the quench development. The coil constitutive law in the frame of a lumped parameter circuit model is given by the following equation:

$$V_{term} = R_{joint}I_{coil}(t) + R_{NZ}I_{coil}(t) + L\,\frac{dI_{coil}}{dt} \qquad (2.6)$$

where L = 0.44 [H], is the prototype coil inductance; $V_{term} = R_{joint} \cdot I_{coil}(t = 0s)$, is the overall voltage of the coil, which is kept constant during the quench; R_{NZ} is the total resistance of the prototype coil, given by the sum of the resistances of the normal zones developed in each pancake. This resistance is computed at every time step through a numerical integration of the following equation:

$$R_{NZ}(t) = \frac{4}{I_{coil}^2(t)} \sum_{i=7}^{12} \int_{V_i} \mathbf{E}_i(x,y,t)\mathbf{J}_i(x,y,t)dV_i \qquad (2.7)$$

where V_i represents the part of the i-th pancake represented in the 2D model, and the factor 4 accounts for the fact that only 6 out of 12 pancakes are modelled and that only a half of each pancake is discretized for the above-mentioned symmetry conditions.

2.3.5 Homogenization Procedure

A non-linear power law is introduced as a constitutive electric characteristic for the superconducting layer. The critical surface of the superconducting YBCO layer as a function of temperature, magnetic flux density and field angle is described through the parameterization provided in [13].

To avoid discretizing each layer of the tape, a homogenization procedure is applied to calculate the longitudinal (in the azimuthal direction) and transverse (in the radial direction) components of the anisotropic electrical and thermal conductivities [9], [14], [8]. As for the longitudinal direction, all the tape layers are assumed to be in parallel. The electric field is taken uniform over each layer of the YBCO tape, and

$$E_c \left(\frac{I_{YBCO}(x,y,t)}{I_c\left(T(x,y,t),B(x,y,t),E(x,y,t)\right)} \right)^n =$$
$$= \frac{I_{coil}(t) - I_{YBCO}(x,y,t)}{\sum\limits_{\substack{j,\\i\neq k}} \sigma_j\left(T_j(x,y,t),B_j(x,y,t),E_j(x,y,t)\right)S_j} \qquad (2.8)$$

where I_{coil} is the prototype coil current, I_{YBCO} is the current in the YBCO layer and I_c its critical current, σ_j the electrical conductivity of the j-th layer of the superconducting tape as a function of temperature, magnetic flux density and electric field, S_j is the surface of the j-th layer. The sum is extended to all the tape layers except the k-th one corresponding to the YBCO.

A homogenized longitudinal (azimuthal) conductivity is therefore computed for the i-th pancake as:

$$\sigma_i^{hom}\left(T_j(x,y,t), B_j(x,y,t), E_j(x,y,t)\right) = \frac{I_{coil}(t)}{\left(\sum_i S_i\right) E_i(x,y,t)} \qquad (2.9)$$

where σ_i^{hom} is the homogenized longitudinal electrical conductivity of the i-th pancake.

Since the turns are electrically insulated from each other by the alumina layers, the electrical conductivity of the homogenous material is taken extremely low (10×10^{-8} S/m) in the radial direction (homogenized transverse electrical conductivity).

A similar procedure is adopted for the calculation of the homogenized thermal conductivities in the azimuthal and radial directions. The thermal resistances are assumed to be in parallel to calculate the longitudinal homogenized thermal conductivity and in series for the homogenized transverse one. In the calculation of the longitudinal homogenized thermal conductivity, the stainless steel layer of the co-wind was taken into account, whereas the alumina layers were neglected due to their low thermal conductivity. The alumina layer was taken into account in the calculation of the transverse thermal conductivity only.

The magnetic field and temperature dependent material properties used in the homogenization procedure are taken from [15] and [16].

2.4   Results of Quench Analysis

The model presented was applied to the analysis of temperature, magnetic flux density, coil current and resistance evolution during the quench tests of the NHMFL prototype coil.

In the simulation results presented here, pulses of the heater current up to maximal values of 14 A, 16 A and 19 A were considered, with a total duration of about 0.8 s. The total simulation time was set to 3 s. The total computation time for one simulation is about 20 h on a workstation with 64 GB RAM and 2.3 GHz processor.

The profiles of the corresponding heater currents are plotted in Fig. 2.8. The comparison between experimental and numerical results was considered to set the value of the two free parameters of the model, namely the axial thermal interface resistance between adjacent pancakes, and the tilt

angle correction between magnetic field vector and the tape surface. The distributed axial thermal interface resistance R_{cz} was set to $10 \times 10^{-2} \, \mathrm{m^2 K/W}$, and the tilt angle to $2°$.
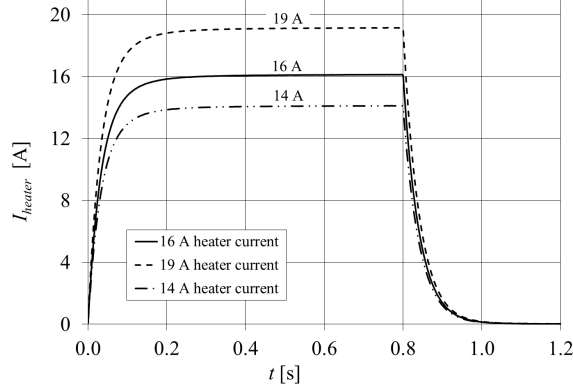

Figure 2.8: Time evolutions of the heater currents for the pulses with $14 \, \mathrm{A}$, $16 \, \mathrm{A}$ and $19 \, \mathrm{A}$ maximal current. The pulse duration is set to $0.8 \, \mathrm{s}$.
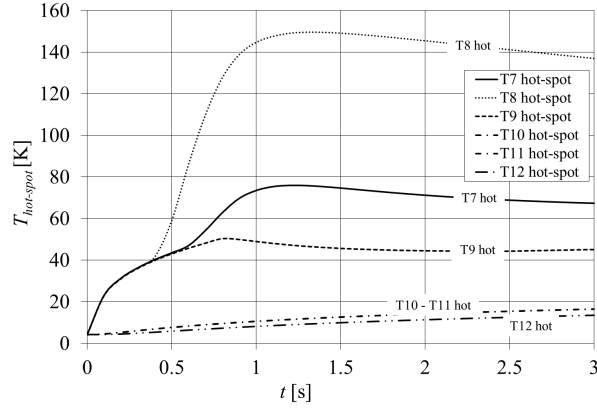
2.4.1 Temperature Evolution

Figure 2.9: Evolution of the hot spot temperature of pancakes 7, 8, 9, 10, 11, 12 during the quench with $16 \, \mathrm{A}$ heater pulse current.

The evolution of the computed hot spot temperature of each pancake during the quench is shown in Fig. 2.9. It is worth noting that the peak temperature in each pancake has a similar initial growth during the external heat pulse for the two groups of pancakes (7, 8, 9) and (10, 11, 12), with the first group reaching higher temperatures. Before the end of the external heat pulse, about 0.4 s, the temperature of pancake 8 rises to significantly higher temperatures than that of the other pancakes. The maximum temperature
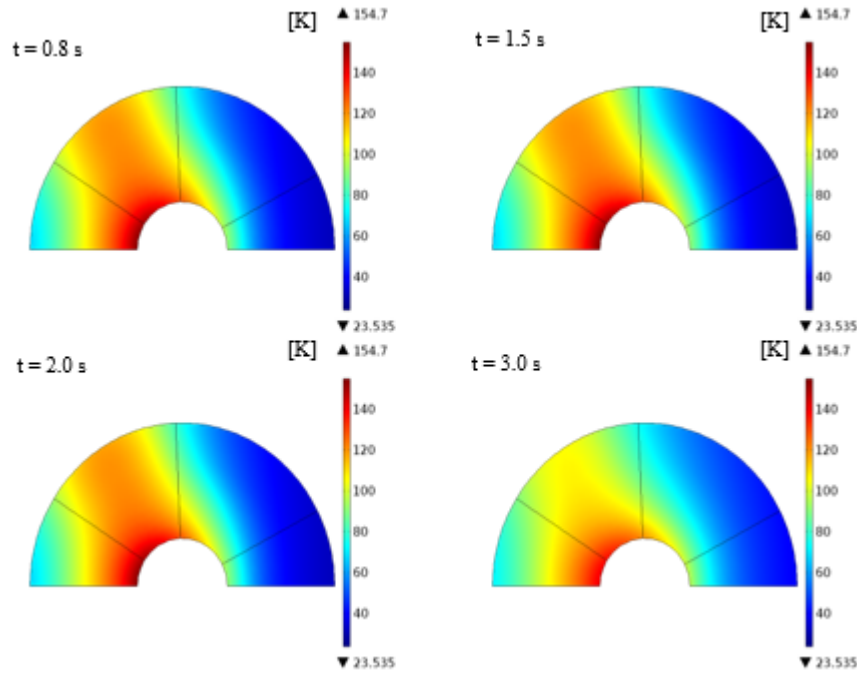
42

Figure 2.10: Temperature distribution over pancake 8 during the quench test with a 16 A heater current pulse at various time instants: 0.8 s (end of the pulse), 1.5 s, 2.0 s, 3.0 s.

of the hot spot in pancake 8 reaches over 150 K. Pancakes 10, 11 and 12 exhibit a similar behaviour, with hot spot temperatures that steadily increase up to about 15-18 K at the end of the simulation. The fact that these pancakes reach lower peak temperatures is related to the indirect heating through conduction from the other pancakes, since in this specific quench test the heaters in heater spacer 1 are not fired. As a matter of fact, other simulations performed with heater 1 on (not reported here) give higher peak temperatures in pancake 11 than in all other pancakes.

The spatial evolution of the temperature distribution for pancake 8 is shown in Fig. 2.10 at different time steps, namely at the end of the pulse (0.8 s) and at selected time instants during the simulations (1.5 s, 2.0 s, 3.0 s). The pancake region included between two out of three heaters (which for symmetry condition is located close to the x-axis) is the one that reaches the highest temperatures during the quench. To compare the evolution of the temperature of pancake 8 to that of the other pancakes, the temperature distribution in all pancakes at t = 1.5 s is shown in Fig. 2.11. As already mentioned, pancakes 7, 8, and 9 at the centre of the prototype coil exhibit higher temperatures than pancakes 10, 11, 12 at the top of the coil. The temperature distribution on pancakes 10-12 is rather uniform, whereas large gradients can be observed for the temperature distribution over pancake 8. Further stress analysis is required to determine the impact of these
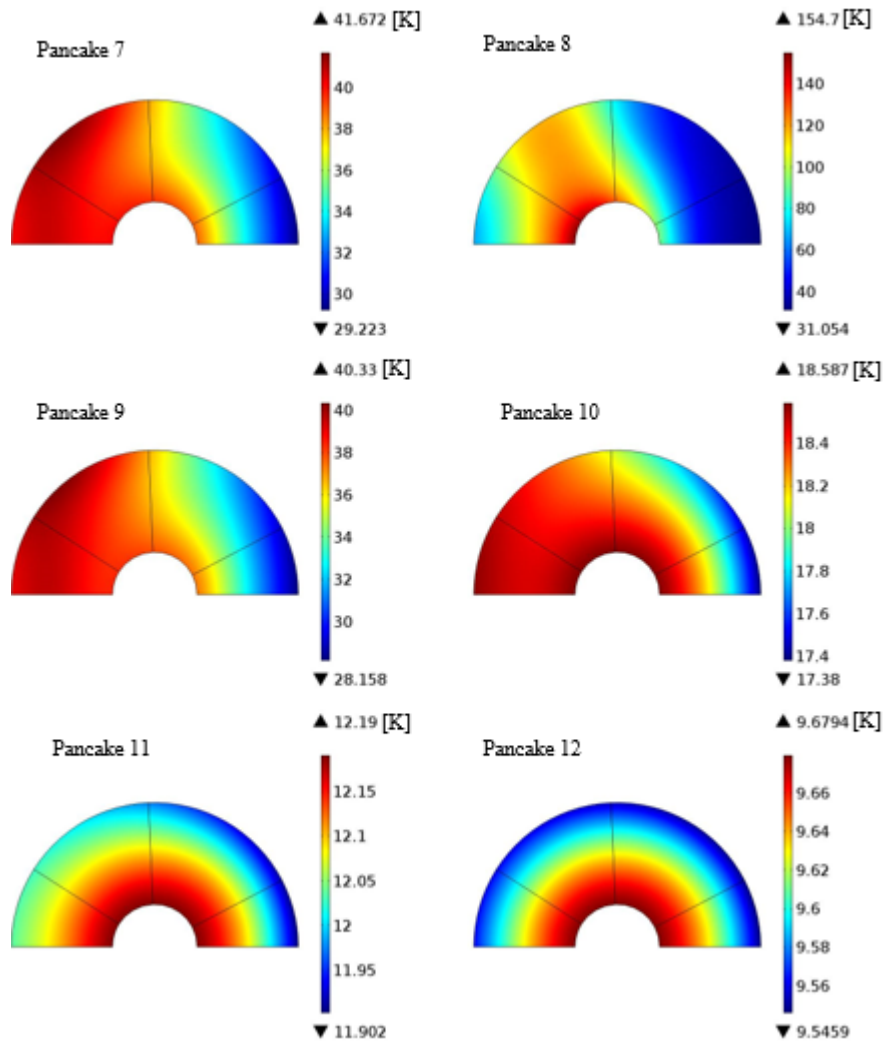
Figure 2.11: Temperature distribution over all simulated pancakes (7 through 12) at t = 1.5 s during the quench test with a 16 A heater current. The highest temperature is reached on pancake 8.

temperature gradients, which is beyond the scope of this work.

2.4.2 Magnetic Flux Density and Field Angle

During the quench tests, the damping of the coil current affects the magnetic field profile over the winding and consequently the critical current density. The distribution of the magnetic flux density over pancake 7 is presented in Fig. 2.12 at the time instants 0.1 s, and 2.0 s. As for the angle between the magnetic flux density vector and the tape *c*-axis, the largest deviation
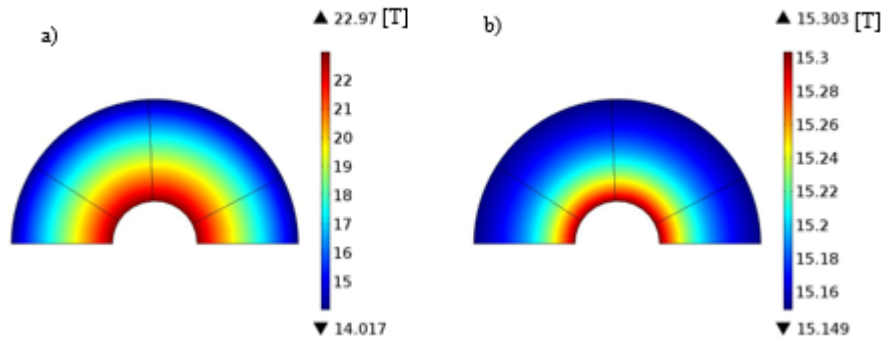
Figure 2.12: Distribution of the magnetic flux density on pancake 7 during the quench test with a 16 A heater current at (a) t = 0.1 s and (b) t = 2.0 s.
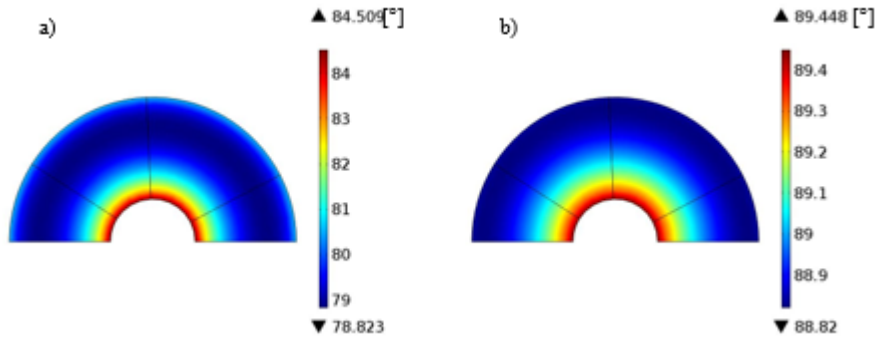

Figure 2.13: Distribution of the field angle on pancake 12 during the quench test with a 16 A heater current at (a) t = 0.1 s and (b) t = 2.0 s.

from a 90 angle can be observed on pancake 12. The field angle evolution on pancake 12 during quench is presented in Fig. 2.13. The effect of actual field angle values with due regard for the coil actual layouts on the quench behaviour analysis results is a very delicate and extremely important matter that we tried to show and underline in this work. Further, more detailed study is required to clarify the effect to more extent and proceed with generalizations and recommendations.

2.4.3 Comparison between Numerical and Experimental Results

The evolution of the resistance of all pancakes during quench is shown in Fig. 2.14 where the overall resistance of the coil is also presented. The resistance of pancakes 7, 9, 10, 11, 12 are much smaller than that of pancake 8 due to the different evolution of the normal zones in the various pancakes discussed in Section 2.4.1. The total computed resistance of the prototype
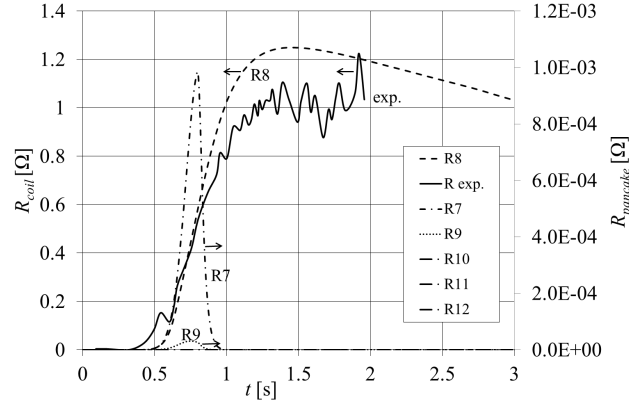
Figure 2.14: Contribution of the resistances of individual pancakes 7 through 12 on the total prototype resistance during the quench test with a 16 A maximal heater current (the arrows indicate the reference y-axis corresponding to each curve). During the analysed quench, the resistances of pancakes 10, 11, 12 are negligible
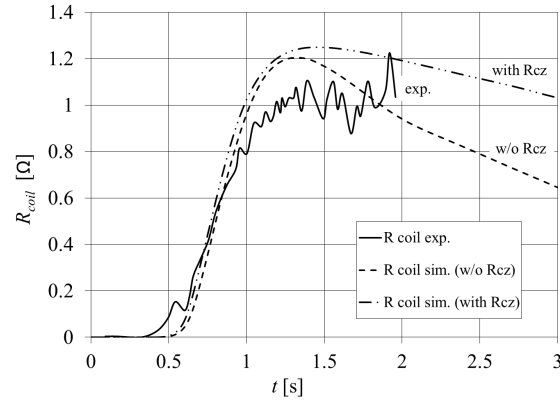

Figure 2.15: Comparison of computed (R coil sim.) and measured (R coil exp.) prototype coil overall resistance during a quench with 16 A maximal heater current. R_{cz} is the thermal interface resistance between each pancake and the G10 layer. The coil currents refer to the primary axis; the coil resistances refer to the secondary y-axis.

coil practically corresponds to that of pancake 8. This simulated resistance compares well with the one calculated from the coil current and voltage measurements taking into account the coil inductance value. However, some delay between the rising of the experimentally obtained resistance and that of the numerical one can be observed in Fig. 2.14. The impact of the variation of the R_{cz} parameter is shown in Fig. 2.15 by a comparison of the computed and measured overall resistance of the prototype coil. Increasing the value of this parameter from 0 to $10 \times 10^{-2}\,\mathrm{m^2K/W}$ determines a different reduction of the normal zone during the coil current decay process. The overall coil resistance decays more slowly in the simulation performed accounting for the non-zero R_{cz} resistance than in the simulation performed neglecting

it. The contact thermal resistance is a free parameter of the model. It is one of the possible ways to handle imperfection of the transverse contacts. Its advantage is that it has a physical meaning. The actual values of R_{cz} to be used depend on a number of factors, such as the pancake side surface flatness and quality, the clamping pressure and its distribution over the pancake surface, etc. What values (low or high) are preferable is not fully clear yet, and certainly, it is not univocal. This parameter is likely determined by the quench heaters' characteristics (the size and heating power and duration) and seems to be rather specific to a particular magnet design. As a conse-
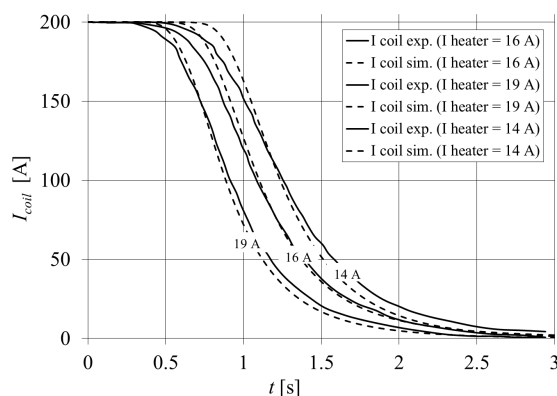

Figure 2.16: Comparison of measured and computed prototype coil currents during the quench tests with 14 A, 16 A and 19 A maximal heater currents.

quence of the normal zone propagation, the prototype coil current decreases in time. The measured current decay is compared in Fig. 2.16 with the results of simulations for three different pulses of the heater current, reaching the maximal values of 14 A, 16 A and 19 A. The same values of parameters obtained for the simulations with a 16 A maximal heater current were adopted in the simulations with maximum heater currents of 14 A and 19 A, obtaining a good agreement in both the cases. The already mentioned delay in the development of the normal zone in the numerical computation with respect to the experimental results determines some delay of the damping of the computed coil current with respect to the measured one.

2.4.4 Normal Zone Propagation Velocity

In order to analyse the propagation of the normal zone, the temperature evolution at different locations on the prototype coil was compared to the local value of the current sharing temperature. The analysis was focused on pancake 8 due to its significant contribution to the total normal zone resistance. The calculation points are located at the average distance between the inner and outer radius of the pancake, at different angles α (90°, 85°, 80°, 75°, 70°, 65°, 60°, 55°, 50°, 45°) with respect to the x-axis (see Fig. 2.5).

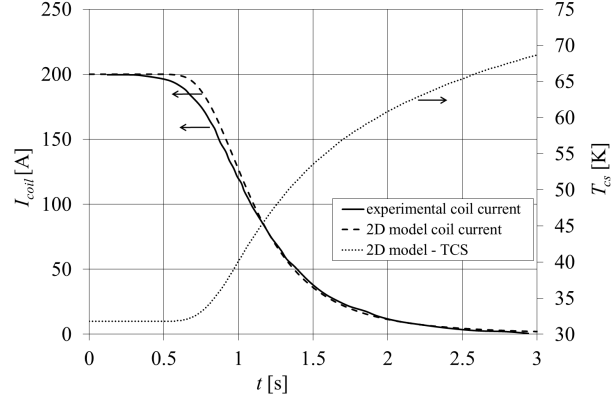The current sharing temperature (see Fig. 2.17) exhibits the same value in

Figure 2.17: Evolution in time of the current sharing temperature at selected locations of pancake 8 during the quench test with 16 A peak heater current. The current sharing temperature increases due to the drop of the self-field during quench.
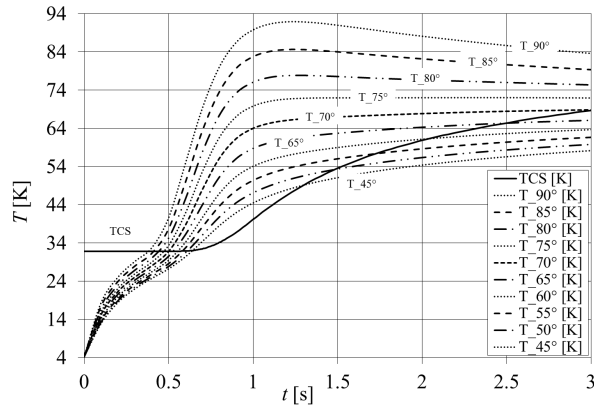

Figure 2.18: Temperature evolution at the selected locations of pancake 8 (see figure 4(b)) during a quench test with 16 A peak heater current. The normal zone propagation velocity (NZPV) is defined here as the velocity of propagation of the front at which the temperature equals the current sharing temperature.

all these positions, since the magnetic field intensity and angle with respect to the tape c-axis is assumed to be the same. The comparison between the computed temperature at these locations and their common current sharing temperature is plotted in Fig. 2.18. Since the current sharing temperature varies with position and in time during the simulation, a definition of the Normal Zone Propagation Velocity (NZPV) is not trivial. The NZPV is computed here as the propagation velocity of the front at which the temperature corresponds to the current sharing one. The ratio between the distance of the computation points and the time interval of the quench front propagation determines the value of the NZPV. This intersection occurs at

the current sharing temperature values in a small range of $1\,\mathrm{K}$ around $31\,\mathrm{K}$, so that the difference in the current sharing temperature does not affect practically the quench propagation velocity calculation results. The calculated values of NZPV are in the range from 9 to $15\,\mathrm{cm/s}$, with an average value of about $12\,\mathrm{cm/s}$, which is similar to the values presented in [9] [17].

2.5 Conclusion

A novel approach to the analysis of quench in HTS REBCO coils made of multiple pancakes was developed in the framework of a quasi-3D FEM model. Instead of applying a fully 3D model, this approach is based on the connection of several pancakes described with a 2D electro-thermal nonlinear FEM model through distributed thermal resistances in the axial direction. No electrical connection between different pancakes is modelled given their electrical stand-off. The winding material is described as a homogenous material with anisotropic thermal and electrical conductivities that accounts for the intrinsic anisotropy of the superconducting tape, the impact of the turn-to-turn insulation on the thermal resistance. The homogenization procedure adopted was previously validated both for individual tapes and for stacks of tapes in superconducting HTS cables.

The model developed accounts for all the main physical phenomena occurring during a quench in the coil, including the temperature dependent properties and the impact of the variable temperature, magnetic flux density, field angle on the superconductor critical current.

The model was applied to analyse quench experiments performed on a prototype coil developed at the NHMFL in USA in the framework of research activities launched for the manufacturing of a fully superconducting 32 T magnet. The main features of the experimental results can be satisfactorily described by the model. The computed and measured prototype coil currents and total resistances during quenches are in good agreement for different quench tests, thus confirming the validity of the proposed approach. The simulation results show the relative impact of the resistances developed in the normal zone of each pancake on the overall coil resistance and quench behaviour, which is a relevant information to detect the most critical pancakes and locations in the coil. The model also gives an insight into the features of a normal zone propagation in the coil that occurs at average velocities about $0.12\,\text{m/s}$.

Bibliography

[1] H. W. Weijers, W. D. Markiewicz, A. J. Voran, S. R. Gundlach, W. R. Sheppard, B. Jarvis, Z. L. Johnson, P. D. Noyes, J. Lu, H. Kandel, H. Bai, A. V. Gavrilin, Y. L. Viouchov, D. C. Larbalester, D. V. Abraimov, "Progress in the Development of a Superconducting 32 T Magnet With REBCO High Field Coils," *IEEE Trans. Appl. Supercond., vol. 24, no. 3, 2014.*

[2] W. D. Markiewicz, D. C. Larbalestier, H. W. Weijers, A. J. Voran, K. W. Pickard, W. R. Sheppard, J. Jaroszynski, A. Xu, R. P. Walsh, J. Lu, A. V. Gavrilin, P. D Noyes, "Design of a Superconducting 32 T Magnet With REBCO High Field Coils," *IEEE Trans. Appl. Supercond., vol. 22, no. 3, 2012.*

[3] M. Breschi, L. Cavallucci, P. L. Ribani, A. V. Gavrilin, and H. W. Weijers "Analysis of quench in the NHMFL REBCO prototype coils for the 32T Magnet Project," *Supercond. Sci. Technol. 29 (2016) 055002 (11pp).*

[4] J. Lu, H. Kandel, K. Han, W. R. Sheppard, D. M. McRae, A. Voran, K. W. Pickard, R. E. Goddard, Y. L. Viouchkov, H. W. Weijers, W. D. Markiewicz, "Insulation of Coated Conductors for High Field Magnet Application," *IEEE Trans. Appl. Supercond., vol. 22, no. 3, 2012.*

[5] P. D. Noyes, W. D. Markiewicz, A. J. Voran, W. R Sheppard, K. W. Pickard, J. B. Jarvis, H. W. Weijers, A. V. Gavrilin, "Protection Heater Development for REBCO Coils," *IEEE Trans. Appl. Supercond., vol. 22, no. 3, 2012.*

[6] https://nationalmaglab.org/user-facilities/dc-field .

[7] COMSOL Multiphysics Users Guide, COMSOL, Burlington, MA, USA, 2012.

[8] M. Casali, M. Breschi, P. L. Ribani, "Two-Dimensional Anisotropic Model of YBCO Coated Conductors," *IEEE Trans. Appl. Supercond., vol. 25, no. 1, 2015.*

[9] M. Breschi, M. Casali, L. Cavallucci, G. De Marzi, G. Tomassetti, "Electro Thermal Analysis of a Twisted Stacked YBCO Cable in Conduit Conductor," *IEEE Trans. Appl. Supercond., vol. 25, no. 3, 2015.*

[10] A.V. Gavrilin, et. al., "Comprehensive quench analysis of the NHMFL 32T all-superconducting magnet", presented at CHATS AS 2015, Bologna, Italy, 14-16 September, 2015.

[11] H.Bai, W. D. Markiewicz, H. W. Weijers, A. Voran, P. D. Noyes, B. Jarvis, W. R. Sheppard, Z. L. Johnson, S. R. Gundlach, S. T. Hannahs, "Impact of Trapped Helium Gas Bubble in Liquid Helium on the Cooling in High Magnetic Field," *IEEE Trans. Appl. Supercond., vol. 25, no. 3, 2015.*

[12] M. Fabbri, P. L. Ribani, "A Priori Error Bounds on Potentials, Field, and Energies Evaluated With a Modified Kernel," *IEEE Trans. Magn., vol. 37, no. 4, 2001.*

[13] D. K. Hilton, A. V. Gavrilin, U. P. Trociewitz, "Practical fit functions for transport critical current versus magnitude and angle data from (RE)BCO coated conductors at fixed low temperature and in high magnetic fields," *Supercond. Sci. Technol. 28 (2015) 074002 (9pp).*

[14] W. K. Chan, "A Hierarchical Three-Dimensional Multiscale Electro-Magneto-Thermal Model of Quenching in REB2Cu3O7- Coated-Conductor-Based Coils," *IEEE Trans. Appl. Supercond., vol. 22, no. 5, 2012.*

[15] P. Bauer, H. Rajainmaki, E. Salpietro, "EFDA Material Data Compilation for Superconductor Simulation," European Fusion Development Agreement.

[16] J. Lu, E. S. Choi, and H. D Zhou, "Physical Properties of Hastelloy C-276TM at cryogenic temperatures," *Journal of Applied Physics, 103:064908 1-6, 2008.*

[17] E. Haro, J. Jarvela, A. Stenvall, "Variation of Quench Propagation Velocities in YBCO Cables," *J. Supercond. Nov Magn (2015) 28:1705-1710.*

Chapter 3

Analysis of Quench in the R&D Prototype Coils for the 32 T Magnet: Prototype #2

3.1 Introduction

In the previous chapter, the first prototype composed by 12 REBCO pancakes is studied during quench initiation and propagation as a foretype of the 32 T magnet insert composed of two coils and 120 pancakes [1], [2]. In the 2015, as a part of the research activity for the 32-T magnet developed at the NHMFL, HTS insert dual-coil prototypes have been tested in the LTS outsert, mimicking the design magnet operation and quench behavior. The tests on the coupled insert/outsert system were performed at 4.2 K, using a set of custom-made quench protection heaters to be employed in the actual insert.

In this chapter, we describe the coupled electromagnetic-thermal numerical model presented in [3] and we apply it to analyze the dual-coil insert prototype, assembled from two coaxial nested HTS coils of equal length and introduced into the multicoil LTS outsert bore. Since the development of a complete 3D model of the system of multiple insert and outsert coils would require a huge computational effort, in this chapter, we followed a reduced dimensionality approach introduced in [4], based on the quasi-3-D model described in the chapter 2. The presence of a double coil composed of 24 pancake and the requirement to couple the HTS insert with the LTS outsert imposed to reduce the degrees of freedom to limit the computational effort. The model described in the previous chapter is therefore adjusted and the current density continuity condition presented in section 2.3.2 is not solved for the study of the second prototype here discussed. The insulated structure of the prototype nevertheless allows the computation of the terminal voltage of each pancake of the insert during the experimental quench test.

The six modules (i.e., 12 pancakes) which compose each of the two insert coils are discretized as 2D elements with a FEM model implemented in the COMSOL Multiphysics environment [5]. The thermal model allows one to account for the inductive coupling of the two series-connected HTS insert coils and for their mutual interaction with the LTS outsert. Therefore, the model permits accounting for variations of the outsert transport current in time, which occur when a real quench in one of the LTS outsert sections triggers an action of the quench protection system.

In the modeling of devices made of (hundreds of) meters of 2G REBCO tapes, a parameterization of the superconducting layer critical surface is usually adopted, albeit remarkably complicated. In some cases, the corresponding parameters are derived from measurements performed on short samples, with typical lengths in the range of 5 to 20 cm [6], [7]. However, remarkable inhomogeneities of the critical current have been observed along the tapes [8] [9], which may affect the magnet quench behavior and the insert protection system efficiency. In this chapter, those inhomogeneities have been simulated by means of correction factors used as fitting parameters.

The model developed has been applied to the analysis of the normal zone resistances in both HTS insert prototype coils and of the temperature evolution during the quench tests. A comparison of numerical and experimental results is presented concerning both the currents in the HTS coils and the terminal voltages of the outsert modules. An interesting aspect of the mutual inductive interaction between the insert and outsert coils is the energy exchange between these two coil systems. The simulations enabled us to quantitatively assess the extent of this energy exchange, and to compare it to the energy dissipated in the normal zones due to the Joule losses in these resistive regions.

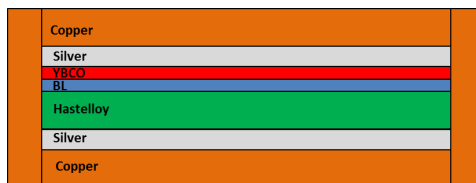## 3.2 Prototype Coil #2 and Experimental Tests

Figure 3.1: Illustration of the cross section of the SuperPower SCS4050 tape used for the NHMFL prototype (not in scale).

As anticipated in the introduction, the quench tests were performed on a REBCO insert prototype manufactured by the NHMFL. The prototype is comprised of two short nested coils wound with Super Power REBCO tape. The tape structure is explained in Fig. 3.1; the main geometrical parameters
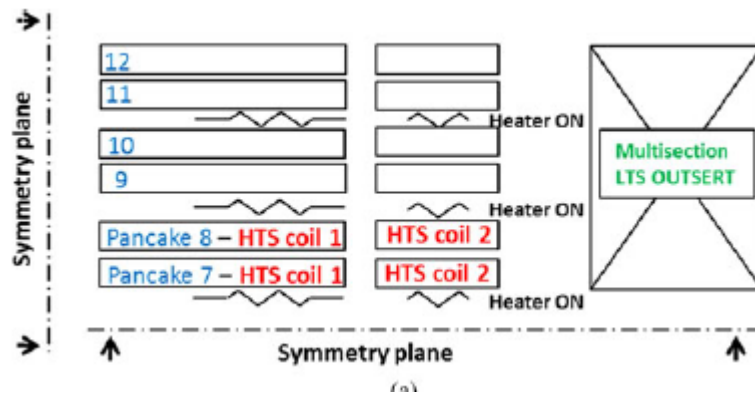
Figure 3.2: Structure of the two insert HTS coils introduced in the bore of the NHMFL multisection LTS outsert. The heater disks containing various seriesconnected heater elements are located between the different insert coil modules and are fired simultaneously for quench initiation.
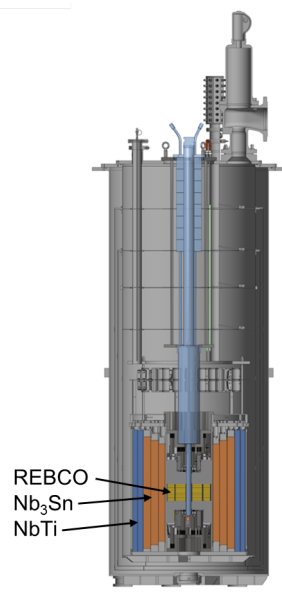
Figure 3.3: Illustration of the two HTS inserts and the LTS outsert [8].

of the tape and its insulation, representing sol-gel alumina plated stainless steel thin strips, are reported in Table 3.1. The two insert coils are made of twelve pancakes each, paired in six modules, as shown in Fig. 3.2. The prototype is in effect distinguished from the actual insert by the number of modules only: the prototype coils are much shorter than those of the actual insert. The electrical insulation between pancakes is provided by G-10 sheets. The main properties of the inner and outer coils of the insert

55

prototype, indicated here as coil 1 and coil 2 respectively, are reported in Table 3.2. The heaters used to initiate a protected quench are composed of seriesly- connected heater elements embedded between thin G-10 and kapton disks (Fig. 3.4). In particular, three heater elements are used on each heater disk in coil 1 (the inner coil), whereas eight heater elements are installed on each disk of coil 2 (the outer coil). Five heater disks are introduced between the six modules of coil 1, respectively; coil 2 is manufactured with the same configuration. The magnet system is a pool-cooled one at 4.2 K, the insert and outsert are designed to be energized independently, using individual power supplies.
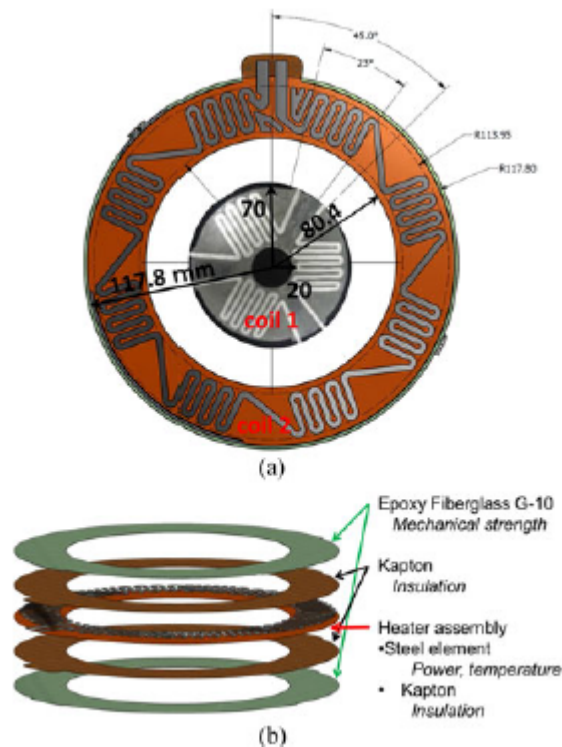

Figure 3.4: Illustration of the NHMFL HTS insert double coil with indication of the heater elements. (a) Three equally spaced heater elements are located on the inner coil, whereas eight heater elements are used to initiate quench in the outer coil. (b) Detailed configuration of the heater layers [8].

The LTS 5-coil outsert, manufactured by Oxford Instruments, is divided electrically into seventeen sections (for quench protection purpose), and it can be separately discharged to outer dump resistors in the case of a quench. The LTS outsert is equipped with an active quench protection system that intervenes after detecting two subsequent events. The terminal voltage on one of the outsert sections should exceed a given threshold voltage (+/- 8 volts) and, after that, the voltage on one of the sections should exceed (-/+

Table 3.1:
GEOMETRIC PROPERTIES OF TAPE AND INSULATION

Tape geometrical properties		
	Thickness [μm]	**Width** [mm]
Copper (bottom)	50	4.12 ± 0.02
Silver (bottom)	1.8	4.00 ± 0.01
Hastelly C276	50	4.00 ± 0.01
Buffer Layer	0.2	4.00 ± 0.01
REBCO	1.0	4.00 ± 0.01
Turn to turn insulation		
	Thickness [μm]	**Width** [mm]
Stainless Steel	25	4.01 ± 0.001
Sol-gel alumina	12	4.01 ± 0.001

Table 3.2:
GEOMETRIC PROPERTIES OF THE HTS INSERT

	Inner **Radius** [mm]	**Outer** **Radius** [mm]	**Number of** **turns/pancake**
Coil 1	20	70	203
Coil 2	80.4	117.8	152

8 volts). In this case, the quench protection system is triggered; otherwise the "signal" is reckoned as a too weak or false one and the system does not react.

Different quench tests were performed particularly by firing simultaneously all the heater elements of all the heaters in both insert coils. Two quench experiments are analysed in this work, representative for the two cases of technical interest without intervention and with intervention of the outsert quench protection system (see Table 3.3). In the first test case, the HTS insert is energized with a 173 A transport current, while the LTS outsert transport current is set at 134 A. In these conditions, as can be inferred from Fig. 3.5, the magnetic flux density on the insert coil is in the range from 5 T to 16.1 T. The quench in the insert is initiated by a 19 A current pulse in the heaters. The pulse has a shape close to a rectangular one in time and lasts about 1.5 s. In this experiment the quench protection system does not intervene, since the induced voltages do not overcome the threshold value mentioned above. The transport current in the outsert circuit therefore is kept constant during the quench in the HTS insert. The development of normal zones in the insert coils causes the appearing and consequent increasing of the insert resistance, which in its turn determines the insert transport current decay rate.

In the second test case the HTS insert is initially energized with a 222 A

Table 3.3:
PROPERTIES OF EXPERIMENTAL QUENCH TESTS

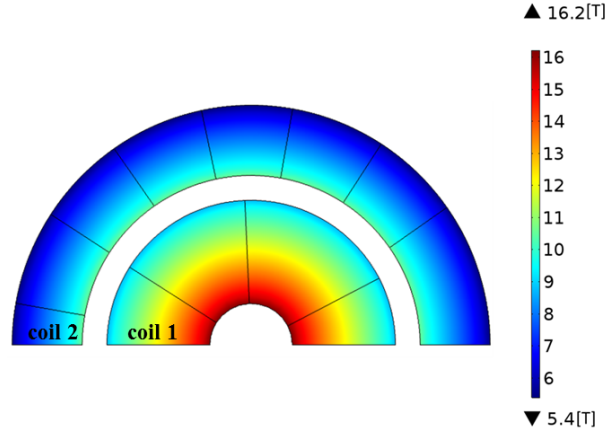|	Quanch case #1	Quanch case #2
Insert current	173 A	222 A
Outsert current	134 A	214 A
Energy	1.75 MJ	4.38 MJ

Figure 3.5: Magnetic flux density modulus distribution on the pancake 6 of the insert; the highest field is found on the inner coil 1.

transport current, while the LTS outsert initial current is set at 214 A. The quench in the insert is initiated by the same type of heater current pulse applied in the previous experiment, with an effective current value of 19 A. In this test, the induced voltages in the outsert meet the threshold criterion for activating the quench protection system that ends up triggering the outsert fast discharge. The currents in the 17 sections of the outsert are therefore variable during this test; their evolutions in time are plotted in Fig. 3.6.

3.3   Model Description

An electrothermal quasi-3-D FEM model for the quench analysis of the HTS coils is coupled in this chapter with a lumped parameter electrical circuit that describes the mutual inductive coupling between the dual coil insert and the multisection outsert. The unknowns of the problem are the temperatures at each mesh node of both the HTS insert coils and the transport current in the insert. Only the insert geometry is directly implemented in the FEM electrothermal model and discretized, since the impact of the multisection outsert coil is accounted for through the circuit model mentioned above. Both the electrothermal model and the lumped parameter circuit
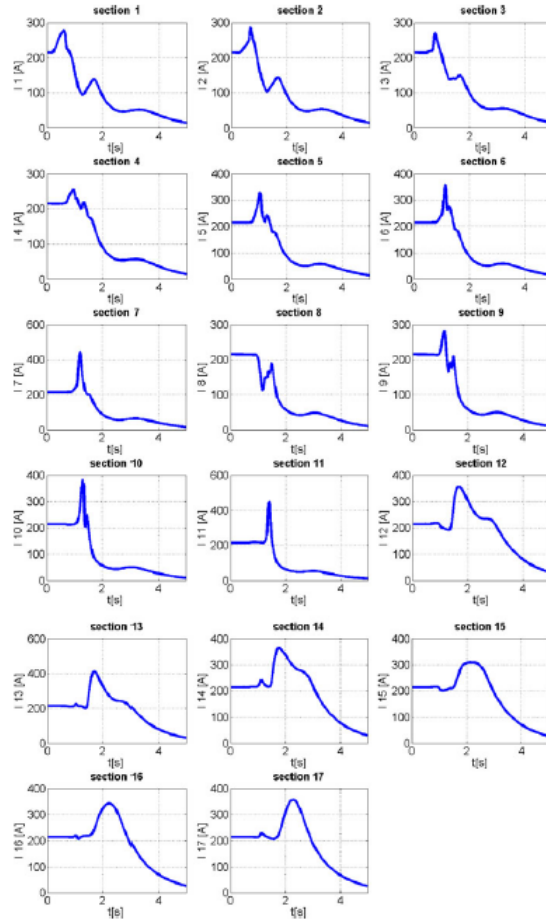
Figure 3.6: Current profile in the various sections of the outsert magnet in the second quench test case with 222 A in the insert and 214 A in the outsert.

are described in detail in the next sections.

3.3.1 Thermal Model

The superconducting tape and its insulation are represented through a homogeneous material with anisotropic physical properties. The homogenization procedure applied enables one to determine longitudinal and transverse electrical and thermal conductivities. The electrical conductivity in the azimuthal direction is calculated as a function of the position, magnetic field, and temperature, assuming all the tape layers to be in parallel and the nonlinear power law is introduced as a constitutive characteristic of the superconducting layer. Under these assumptions, the current sharing between the REBCO and the other layers is taken into account. As a matter of fact, the increasing temperature in the pancake decreases the critical cur-
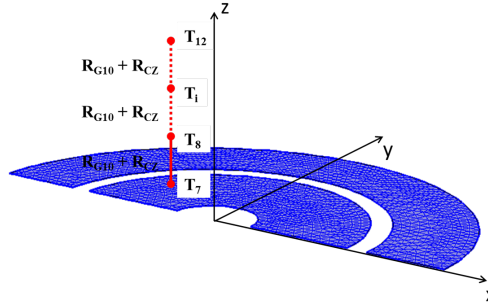
Figure 3.7: Conceptual scheme of the quasi-3-D FEM model implemented in COMSOL Multiphysics.

rent density in the REBCO layer, thus decreasing the current flowing in this layer under the assumption of equal longitudinal electric field between the superconducting and normal layers. In the homogenized approach, this determines a variation of the equivalent electric conductivity of the homogenized material, which in turn determines a change in the computed Joule heating power. The homogenized electrical conductivity in the radial direction is set to an extremely low value, since the turns are electrically insulated owing to the presence of alumina coating of the steel strips.

The quasi-3-D FEM approach is based on the assumption that the temperature is uniformly distributed along the axial direction of each pancake. All the pancakes of the insert coils can, therefore, be modeled as 2-D geometrical elements. The various electrically insulated pancakes can then exchange heat through a set of distributed thermal resistances. Given the symmetry conditions of the pancake geometry and of the heaters configuration, the 2-D mesh only covers half of the pancake surface, as shown in Fig. 3.7. At each point of the mesh, a set of heat balance equations is written for the array of temperatures $T_i(x, y, t), i = 1, ...12$, corresponding to the time t and to the position of the i-th pancake given by the coordinates x, y. A detailed description of the thermal model is provided in [4].

Adiabatic boundary conditions are applied onto the external surface of each coil and a uniform temperature distribution over both insert coils at 4.2 K is assumed as the initial condition.

Calculation of the magnetic flux density generated by the HTS insert and the LTS outsert are performed through a 3-D numerical method [8]. The total magnetic flux density is axially symmetric with respect to the insert axis. The radial and axial components of the magnetic flux density vector are computed at each point of the 2-D mesh and at each time step during the simulations.
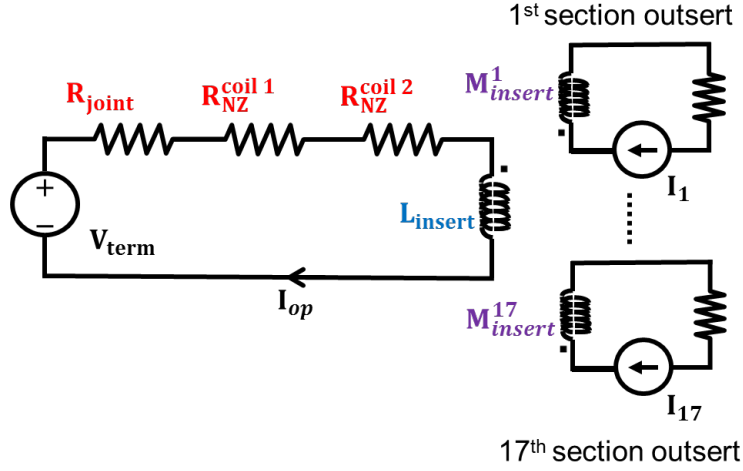
Figure 3.8: Sketch of the lumped parameter circuit of the inductively coupled insert-ousert magnet system.

3.3.2 Insert-Outsert Inductive Coupling Model

The operation current I_{op} in the HTS insert is obtained from the solution of the lumped parameter circuit model describing the mutual induction coupling between the insert and the outsert (see Fig. 3.8):

$$V_t(t) = \left(R_{NZ}^{coil1}(t) + R_{NZ}^{coil2}(t) + R_{joint} \right) I_{op}(t) + L^{in} \frac{dI_{op}}{dt}(t) + \sum_{j=1}^{17} M_j^{in} \frac{dI_j}{dt}(t)$$

(3.1)

where L_{in} is the self-induction coefficient of the HTS insert (composed of the two series connected coils); M_j^{in} the mutual coefficient between the HTS insert and the j-th section of the multisection outsert; I_j is the current of the j-th section of the outsert; V_t is the overall voltage of the insert coil, which is kept constant during the quench; R_{NZ}^{coil1} and R_{NZ}^{coil2} are the total resistances of the insert coils 1 and 2 due to the presence of the normal zones. These resistances are computed at every time step through a numerical integration

$$R_{NZ}^{coil1}(t) = \frac{2}{I_{op}^2(t)} \sum_{i=1}^{12} \int_{V_i} \frac{J^2(t)}{\sigma_i^{coil1}(t, x, y)} dV_i$$

(3.2)

$$R_{NZ}^{coil2}(t) = \frac{2}{I_{op}^2(t)} \sum_{i=1}^{12} \int_{V_i} \frac{J^2(t)}{\sigma_i^{coil2}(t, x, y)} dV_i$$

(3.3)

where V_i represents the part of the i-th pancake represented in the 2-D model, and the factor 2 accounts for the fact that only half of each pancake is modeled thanks to the aforementioned simmetry condition.

61

Table 3.4:
CRITICAL CURRENT PARAMETRIZATION [10]

T[K]	4.2	20	30	40
α_0	1.30	1.22	1.56	0.79
α_1	0.81	0.12	0.41	0.47
b_0	8870	1985	4783	583
b_1	18456	809	312	196
β_0	13.80	1.63	2.78	0.60
β_1	13.8	1.63	2.78	0.60
γ_1	0.18	0.05	0.67	0.38
c_1	2.15	2.11	5.10	26.09
ϵ_1	0.60	0.83	0.80	0.50

3.3.3 Critical Current Parametrization

Figure 3.9: Picture of the SuperPower SCS4050 tape cross section and insulting material in the layer of the Prototype.

A nonlinear power law is used as a constitutive electric characteristic of the superconducting layer, with the critical current expressed as a function of temperature T, magnetic flux density B, and field angle θ with respect to the tape. The critical surface is described through the parametrization provided in [11] and [10]. The parameter values are reported in Table 3.4

$$I_c(B,\theta) = \frac{b_0}{(B+\beta_0)^{\alpha_0}} + \frac{b_1}{(B+\beta_1)^{\alpha_1}} \left[\omega_1^2(B)\cos^2(\theta-\phi_1) + \sin^2(\theta-\phi_1)\right]^{-1/2}$$

(3.4)

where

$$\omega_1(B) = c_1 \left[B + \left(\frac{1}{c_1}\right)^{\frac{1}{\epsilon_1}}\right]^{\epsilon_1}$$

As discussed in [8] and [10], the broad face of the HTS tape of the insert coils is not perfectly aligned with the z-axis (tilting, dishing, etc.). This is due to the fact that the tapes are not flat (see Fig. 2.9). The misalignment of the turns is taken into account by slightly modifying the field angle between the radial and axial component of the magnetic flux density through a tilt angle correction coefficient. The tilt angle applied in this chapter is included in a range from zero to two degrees

Recent measurement performed at NHMFL [8] pointed out a stochastic variation of the tape critical current along the turns of the insert in a range of ± 25%. This effect is of the greatest importance in the insert coil behavior, due to the very significant variation of I_c along each tape and from tape to

tape as well. In this chapter, these non-uniformities are taken into account by means of correction factors of the critical current that are averaged over each pancake. The values of the correction coefficients were found through several iterations by fitting the simulation results to the experimental ones. In any case, the critical currents values do not deviate more than ± 25% from those provided by the critical surface parameterization.

The set of correction coefficients identified with this procedure is not necessarily the only one; there may be other parameter combinations that allow reaching a similar agreement. Indeed these nonuniformities represent a remarkable difference with respect to LTS coils, where the conductor properties are much more homogeneous, and require new modeling approaches. The approach followed here is, therefore, a first-order approximation to deal with this challenging problem.

3.4   Results of Quench Analysis

3.4.1   Comparison Between Numerical and Experimental Results

The quench induced by the heaters in the HTS insert determines an increase of the overall insert resistance, with a consequent decay of its transport current and increase of the terminal voltages across each module. The numerical model simulates the first 3 s of the quench process, during which the experimental data are recorded.

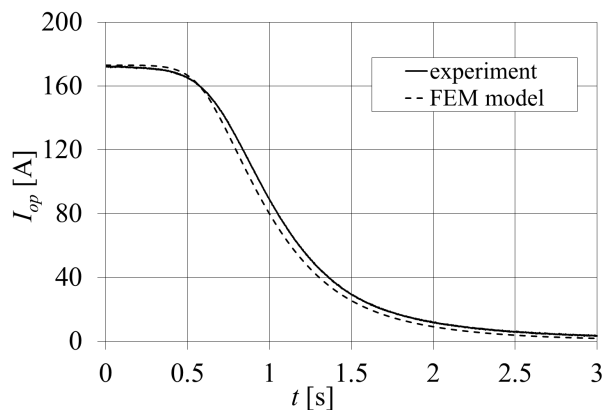**Quench Test With Constant Outsert Current**

Figure 3.10: Comparison between computed and measured values of the insert operation current during the quench test case 1, with 173-A initial current in the insert and 134-A constant current in the outsert.
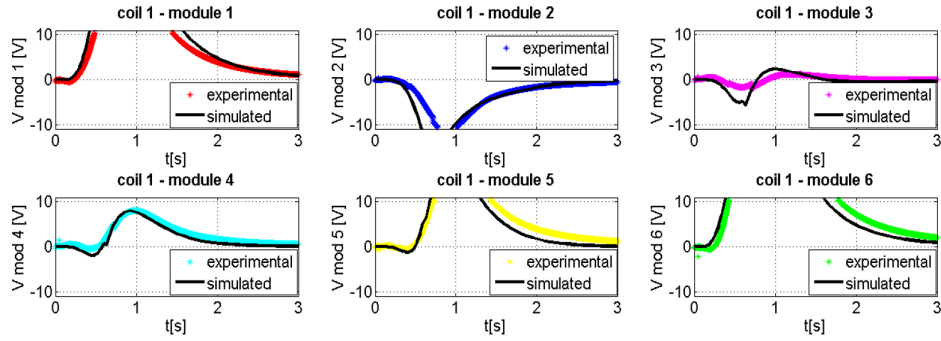
Figure 3.11: Experimental and computed values of the terminal voltages across the modules of coil 1 in the quench test case #1.
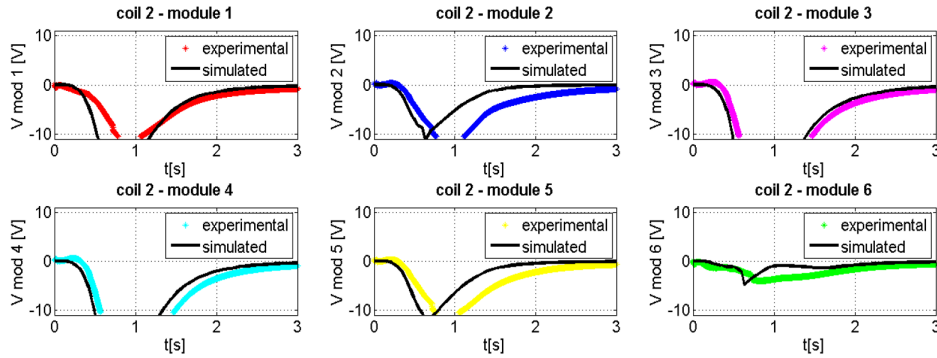

Figure 3.12: Experimental and computed values of the terminal voltages across modules of coil 2 in in the quench test case #1.

As for the first quench test case described in Section 3.2, the comparison between the numerical and experimental results on the insert operation current is reported in Fig. 3.10. A good agreement is found between the measured and computed transport current, which represents the global behavior of the insert coil. The maximal relative error between the numerical and experimental values of the transport current ranges is 48 %, with an average error of 16 %. In order to analyse in more detail the local quench behaviour, a comparison between numerical and experimental results on the terminal voltages across each module is presented in Figs. 3.11 and 3.12 for coil 1 and coil 2, respectively. The experimental and simulated voltage signals exhibit a good agreement. The data acquisition system is set to record voltage signals only in the range $[10/+10]$ V. All comparisons are, therefore, reported for voltage values below this threshold. The terminal voltages provide useful information about the quench initiation and propagation inside the insert coil. In coil 1, the modules 1, 5, and 6 exhibit an earlier transition to the resistive state and quench propagation occurs
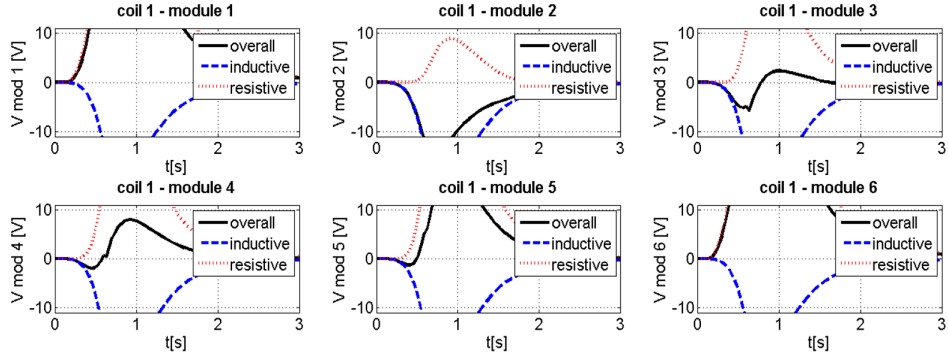
64

Figure 3.13: Computed values of the resistive and inductive components of the terminal voltages across modules of coil 1 in the quench test case #1.
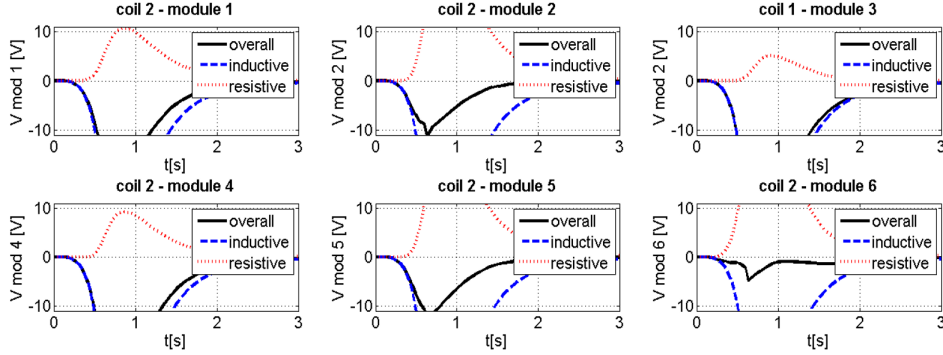

Figure 3.14: Computed values of the resistive and inductive components of the terminal voltages across modules of coil 2 in the quench test case #1.

before all other modules. This phenomenon can be explained by considering the effect of the field angle on the critical current of the superconductive tapes. Since the field angle in these modules, located at the two ends of the coil axial length, is greater than for the other modules, the corresponding reduction of critical current is more significant. This effect is predominant with respect to the impact on critical current of the magnetic flux density, which is greater in the central modules. As shown in Fig. 3.13, the voltage recorded on module 2 of coil 1 exhibits instead a predominant inductive behaviour, with a negative value due to the decay of the coil transport current that overcomes the positive resistive contribution.

It is worth noting that all terminal voltages of the modules of coil 2 also exhibit a predominant inductive behavior, as shown in Fig. 3.14. Also, in this case, the resistive components due to the voltage build-up across the normal zones are less than the corresponding inductive components of the module. This interpretation of the quench evolution in coils 1 and 2 is also confirmed by analysing the computed temperature distributions over the
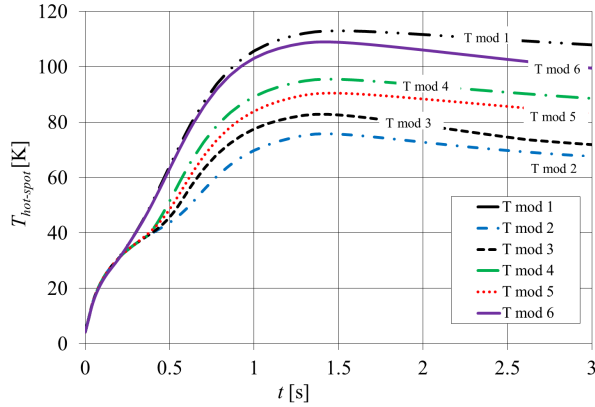
Figure 3.15: Computed values of the hot-spot temperature of each module of coil 1 during the quench test case #1.

modules. The hot-spot temperature of each module of coil 1 and coil 2 in this quench test is shown in Figs. 3.15 and 3.16, respectively. It can be noticed that in coil 1, the maximal hot-spot temperature is reached in the three most critical modules (1 and 6), whereas the hot-spot temperature of module 2 is the lowest. Similar observations can be made when considering the temperature distributions over the pancake cross section, which are more directly correlated to the overall normal zone resistance. As shown in Fig 3.17, the temperatures reached in module 6, and, in particular, on pancake 11, are higher than those reached in module 2, pancake 3. It can be noted that the temperature distribution on pancake 12, also owing to module 6, significantly differs from that of pancake 11, and is characterized by lower temperature values distributed more uniformly. This is due to the fact that this pancake is not directly heated by the heaters (see Fig. 3.2), but only by the heat propagation from the neighbouring pancake 11. As
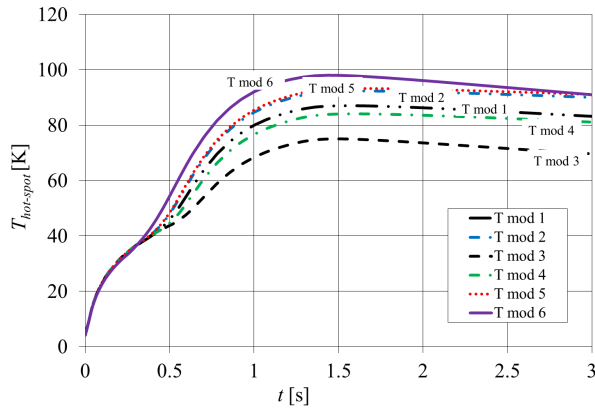

Figure 3.16: Computed values of the hot-spot temperature of each module of coil 2 during the quench test case #1.
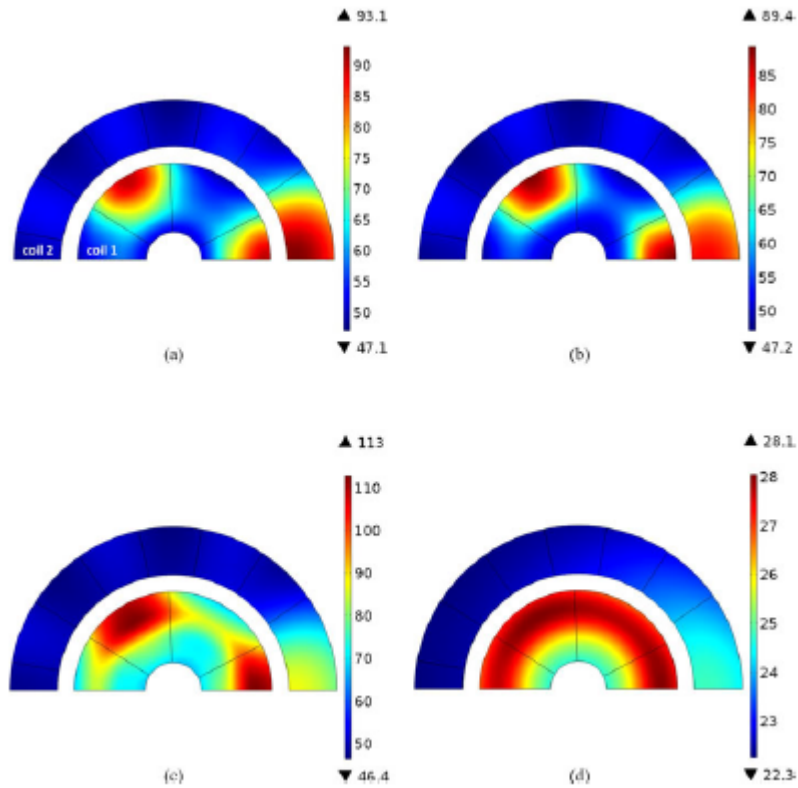
66

Figure 3.17: Computed temperature distribution in pancakes (a) 5, (b) 6, (c) 11, and (d) 12 at t = 1.5 s during the quench test case #1. (a) Pancake 3 (module 2) at 1.5 s. (b) Pancake 4 (module 2) at 1.5 s. (c) Pancake 11 (module 6) at 1.5 s. (d) Pancake 12 (module 6) at 1.5 s.

already remarked considering the hot-spot temperatures, the temperature distributions shown in Fig 3.17 indicate that the values reached in coil 1 are significantly higher than those reached in coil 2. As expected, the peak temperatures on all pancakes are reached in the locations corresponding to the central part of the heaters. The normal zone propagation velocity in the HTS insert is in the range from 0.1 to 0.2 m/s. These values are extremely small in comparison with the typical values of quench propagation velocity in LTS coils, that can range up to about 100 m/s [12], [13], [4]. Thus, the proportion of pancake surface covered by the heaters and the contact/interface quality become the key factors to be properly addressed in the design of the quench protection system

Quench Test With Variable Outsert Current

In the second quench test described in Section 3.2, which was performed with a 222-A transport current in the insert and 214-A transport current in the outsert, the outsert quench protection system is triggered by the
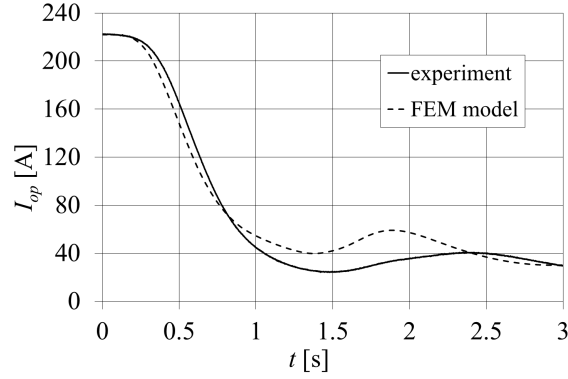
Figure 3.18: Comparison between the numerical and experimental values of the operation current in the insert coil during the quench test case #2
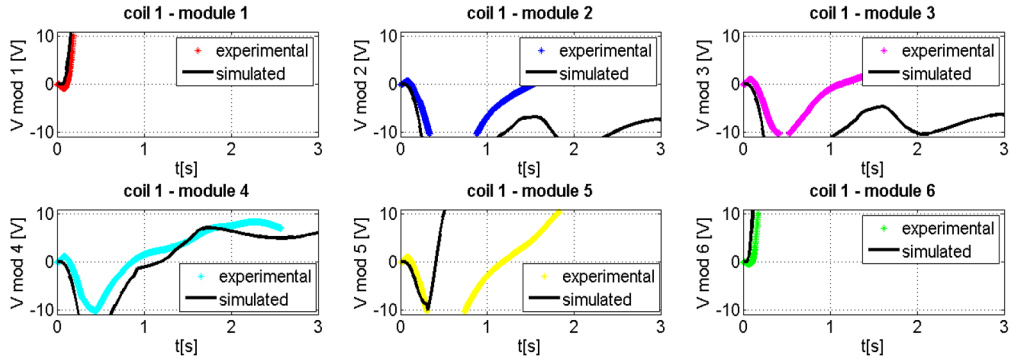
Figure 3.19: Experimental and computed values of the terminal voltages across the modules of coil 1 in the quench test case #2.

induced voltages. The currents in the outsert during the quench are, therefore, variable in time; their evolution is described through a numerical model specifically developed at the NHMFL [8]. The currents in the 17 sections of the outsert have then been used as an input for the computations performed with the model presented here. The time evolution of the transport currents in the various sections of the outsert magnet is reported in Fig. 3.6.

The comparison between numerical and experimental data of transport current in the HTS insert during the quench is reported in Fig. 3.18. The relative error between the numerical and experimental values of transport current ranges from $0.01\,\%$ to $80\,\%$, with an average value around $28\,\%$. The quasi-3-D FEM model computes a transport current in the insert which starts decreasing before the corresponding experimental values. Both the experimental and numerical data exhibit a local maximum almost at the end of the current decay at about $2\,\mathrm{s}$. This maximum occurs slightly earlier in the computations, compared to the experiment, which is probably determined by uncertainties regarding the input data for the computations [8]. The

68
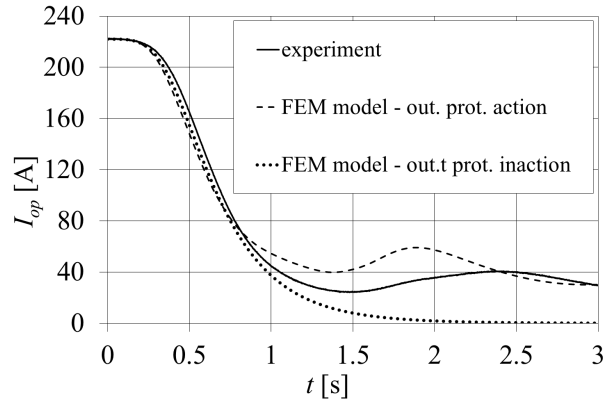
Figure 3.20: Operation current in the insert coil during the quench test case #2 in the two cases of action and inaction of the outsert quench protection system.
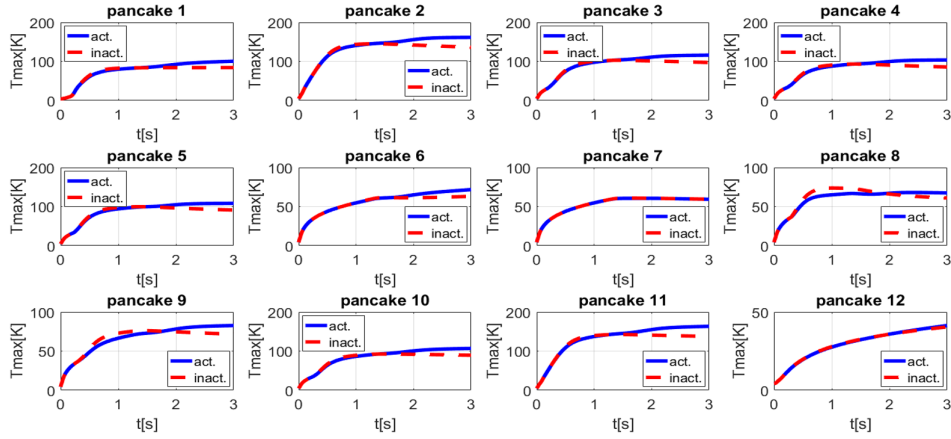
Figure 3.21: Maximum temperature reached in the pancakes of the insert during the quench test case #2 in the two cases of action and inaction of the outsert quench protection system.

local bump is related to the inductive coupling between the insert and the outsert. As shown in Fig. 3.6, some sections of the outsert exhibit a similar bump of the operation current around the same time instant. The variation in time of these currents is in turn related to the intervention of the outsert protection system. When the induced voltage exceeds the threshold criterion on a given section, the quench protection system is triggered, albeit with a predetermined delay specified for each section.

The experimental and computed voltages at the terminals of the coil 1 modules are reported in Fig. 3.19, and they exhibit a good qualitative agreement. The quantitative agreement is rather good in the first phases of the quench, and then becomes less accurate; in this phase, the aforementioned discrepancies on the insert transport current affect the computed terminal

voltages. It can be noticed that also in this case, the modules 1 and 6 of coil 1 exhibit a fast increase of the voltage, thus confirming that the two ends of the coil are its most critical locations and a protected quench starting points in these experiments. This quench study, therefore, confirms that the effect of the field angle is predominant on that of the magnetic field intensity.

In order to better understand the impact of the quench in the outsert on the quench behavior of the insert, an additional simulation was carried out in which, starting from the same initial currents in the insert and in the outsert as in case #2, the outsert is supposed not to exhibit any quench. In this simulation, the outsert current is, therefore, kept constant at the value of 214 A. The comparison between the results of the two simulations with variable and constant outsert current is shown in Fig. 3.20. The lack of intervention of the outsert quench protection system determines a higher magnetic flux density on the insert during the quench. In these conditions, the critical current in the insert turns is less than in the case of quenching outsert, which determines a faster increase of the insert resistances. Consequently, the insert current damps faster in the case of constant current in the outsert.

The maximal temperatures in the pancakes in these two cases are plotted in Fig. 3.21. In most pancakes, including pancakes #2 and #11, which are the most solicited ones, the triggering of the outsert protection system determines a higher peak temperature at the end of the simulation. This result is related to the higher value of transport current in the insert in this phase. In pancakes #8 and #9, a slightly higher hot-spot temperature is computed during the initial phase of quench in the case of no triggering of the outsert protection system. In any case, the impact of the quench in the outsert on the peak temperatures in the insert is very limited, and should not have any practical effect.

3.4.2 Energy Exchange Between Insert and Outsert During Quench

A detailed analysis of the numerical results of quench test case #1 allows one to determine the energy exchange between the insert and outsert coils during the experiment and the amount of the magnetic energy that is dissipated in the normal zones of the insert.

The overall energy balance can be written as

$$\Delta E_m(t) = E_m(0) - E_m(t) = E_{nz}(t) - E_{out}(t) \qquad (3.5)$$

where $\Delta E_m(t)$ is the variation of the total magnetic energy of the coupled insert-outsert system from the initial value $E_m(0)$, to its value at time instant t, $E_m(t)$. On the right-hand side of equation 3.5, $E_{nz}(t)$ is the total energy dissipated in the normal zone resistance of the insert coils 1 and 2 from the beginning of the test to instant t, and $E_{out}(t)$ is the total energy delivered or

70

absorbed by the protection system of the outsert. In the balance equation 3.5, the energy input from the heaters is assumed negligible with respect to the total magnetic energy.

The magnetic energy E_m can be expressed as the sum of the various components related to the self and mutual induction between the coils

$$
\begin{aligned}
E_m(t) &= \frac{1}{2} L^{in} I_{op}(t)^2 + \sum_{j=1}^{17} M_j^{in} I_j(t) I_{op}(t) + \sum_{j=1}^{17} \frac{1}{2} L_j^{out} I_j(t)^2 I_{op}(t) + \\
&+ \sum_{i=1}^{17} \sum_{\substack{j=1 \\ i \neq j}}^{17} M_{ij}^{out} I_i(t) I_j(t) \qquad\qquad (3.6)
\end{aligned}
$$

where L_{out}^j is the self-induction coefficient of the j-th section of the outsert and M_{ij}^{out} is the mutual induction coefficient between the i-th and j-th section of the outsert.

The energy dissipated in the normal zone resistances of the insert can be expressed as the sum of the contributions of the two coils:

$$
E_{nz}(t) = \int_0^t R_{nz}^{coil1}(\tau) I_{op}(\tau) d\tau + \int_0^t R_{nz}^{coil2}(\tau) I_{op}(\tau) d\tau \qquad (3.7)
$$

The energy absorbed by the outsert magnet from the protection system can be determined calculating the voltages v_j^{out} at the terminals of the j-th section of the outsert:

$$
\begin{aligned}
E_{out}(t) &= \sum_{j=1}^{17} \int_0^t v_j^{out}(\tau) I_j(\tau) d\tau \qquad\qquad\qquad\qquad (3.8) \\
&= \sum_{i=1}^{17} \int_0^t \left(L_j^{out} \frac{dI_j}{d\tau}(\tau) + \sum_{\substack{j=1 \\ i \neq j}}^{17} M_{ji}^{out} \frac{dI_i}{d\tau}(\tau) + M_j^{in} \frac{dI_{op}}{d\tau}(\tau) \right) I_j(\tau) d\tau.
\end{aligned}
$$

The evolution in time of the three main terms of the total energy of the system is plotted in Fig. 3.22. The graph shows the time evolution of the energy taking as a reference the magnetic energy at the initial time $E_m(0)$, equal to 1.75 MJ. As observed in Section IV-A, the quench initiation and propagation determine an increase of the overall resistance of the insert and the subsequent damping of its transport current. Since the outsert current is kept constant, only the first two terms of the magnetic energy expression in 3.6 vary during the quench experiment. Fig. 3.22 shows that only a small part of the total magnetic energy, less then 1 %, is dissipated during the transient due to the joule effect in the normal zones of coils 1 and 2. As mentioned above, the coil 1 exhibits a predominant resistive behaviour, thus dissipating more energy than coil 2. It is worth noting that

the largest quote of the energy variation is absorbed by the power supply of the multisection outsert. This mechanism allows to maintain its transport current constant during the experimental test. The energy transfer through inductive coupling is, therefore, able to release most of the magnetic energy of the insert and of the mutual energy between insert and outsert to the outsert power supply, thus avoiding its deposition in the insert coils.

The energy balance allows one to estimate the numerical error of the model developed, by determining the residual of the equation 3.5. In the calculations performed in this chapter, utilizing the mesh described in the next section, this residual is limited below $0.6\,\%$.
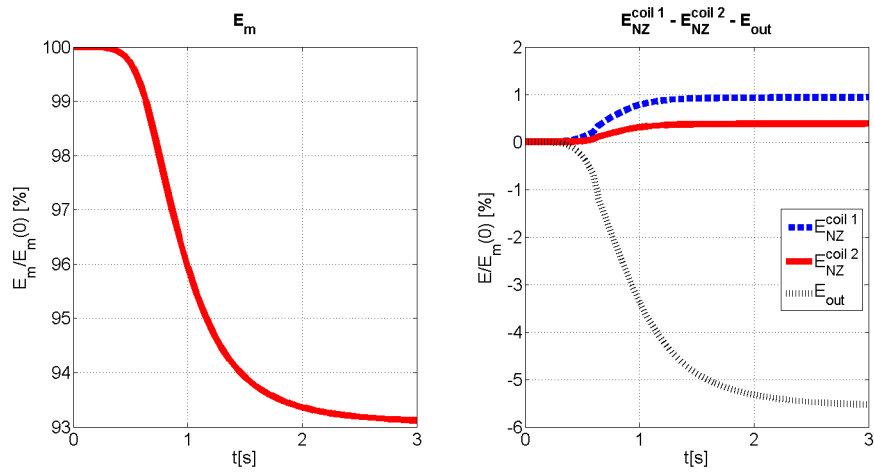

Figure 3.22: Energy exchange between the different coils of the analyzed magnet system during the quench case #1. (a) Evolution in time of the ratio between the total magnetic energy at time t and its initial value 1. (b) Evolution in time of the energy dissipated in the normal zones of coils 1 and 2, and of the energy absorbed from the outsert coil to its power supply.

3.5 Conclusion

An electrothermal model based on a reduced dimensionality approach has been developed in the COMSOL Multiphysics environment to analyze quench in a coupled magnetic system composed of an HTS REBCO dual-coil insert and a multisection LTS outsert. This is the very first implementation of a COMSOL model for a full-scale comprehensive quench analysis of a real sophisticated multicoil superconducting magnet having a complex quench protection system.

The magnetic system was tested at NHMFL in the framework of R&D activities of the NHMFL 32-T magnet project. In the modeling of the HTS insert, its 12 pancakes are described as 2-D elements, connected to each other by means of a distributed thermal resistance. In the meshing of the FEM model, only one pancake is discretized, solving the equations for an array of variables containing the temperatures of all pancakes. An anisotropic homogenization procedure was adopted to reduce the degrees of freedom and model the whole magnet. The critical current dependence on magnetic field and field angle with respect to the tape are included appropriately in the model. The stochastic variations of the tape critical current along the turns of the insert is considered by the implementation of correction factors averaged over each pancake. The introduced correction factors are a first approximation approach enabling one to handle this issue.

The FEM model is complemented by a lumped parameter model of the circuit, enabling one to describe the mutual inductive interactions between the insert and outsert coils.

The comparison of the numerical and experimental results on the decay of the insert current and of the terminal voltages across the insert modules (double pancakes) shows a good agreement in the quench test with constant current in the outsert. A rather good agreement is obtained and the qualitative behaviour of the quench phenomenon is correctly described also in the case of a variable current in the outsert coil sections. Reaching this agreement, however, required to assess the deviations of the critical currents in each turn of the insert coils from their nominal value. In this chapter, these deviations have been kept in the frame of the ± 20% oscillation experimentally observed on tape samples. In addition, variations of some other input parameters are supposed to be taken into account also.

The analysis performed here shows that the quench propagation is more rapid in the pancakes characterized by high values of the field angle, located at the top and bottom of the insert. The computed temperature distributions show that the hot spots of these pancakes reach higher temperatures than the hot spots in the pancakes located in the middle of the insert axial length do. This result indicates that in the present case, the effect of the field angle on the critical current is more significant than that of the magnetic flux density, which reaches higher values in the pancakes located in the

middle of the insert.

The numerical model also allows one to give an insight in the evolution of the magnetic energy of the coupled insert-outsert system during a quench. In the quench case analyzed here, a minor part of the total energy is dissipated in the normal zones of the insert, whereas the greatest quote of the total energy is released from the outsert to its power supply.

Bibliography

[1] H. W. Weijers, W. D. Markiewicz, A. J. Voran, S. R. Gundlach, W. R. Sheppard, B. Jarvis, Z. L. Johnson, P. D. Noyes, J. Lu, H. Kandel, H. Bai, A. V. Gavrilin, Y. L. Viouchov, D. C. Larbalester, D. V. Abraimov, "Progress in the Development of a Superconducting 32 T Magnet With REBCO High Field Coils," IEEE Trans. Appl. Supercond., vol. 24, no. 3, 2014

[2] W. D. Markiewicz, D. C. Larbalestier, H. W. Weijers, A. J. Voran, K. W. Pickard, W. R. Sheppard, J. Jaroszynski, A. Xu, R. P. Walsh, J. Lu, A. V. Gavrilin, P. D Noyes, "Design of a Superconducting 32 T Magnet With REBCO High Field Coils," IEEE Trans. Appl. Supercond., vol. 22, no. 3, 2012.

[3] M. Breschi, L. Cavallucci, P. L. Ribani, A. V. Gavrilin, and H. W. Weijers "Modeling of Quench in the Coupled HTS Insert/LTS Outsert Magnet System of the NHMFL," IEEE Trans. Appl. Supercond., vol. 27, no. 5, 2017.

[4] M Breschi, L Cavallucci, P L Ribani, A V Gavrilin and H W Weijers, "Analysis of quench in the NHMFL REBCO prototype coils for the 32T Magnet Project", Supercond. Sci. Technol. 29 (2016) 055002 (11pp)

[5] COMSOL Multiphysics Users Guide, COMSOL, Burlington, MA, USA, 2012.

[6] X. Wang, U. P. Trociewitz.J. Schwartz, "Self-field quench behaviour of YBa2Cu3O7 coated conductors with different stabilizers," Supercond. Sci. Technol. 22 (2009) 085005 (13pp)

[7] M. Casali, M. Breschi, P. L. Ribani, "Two-Dimensional Anisotropic Model of YBCO Coated Conductors," IEEE Trans. Appl. Supercond., vol. 25, no. 1, 2015

[8] A.V. Gavrilin, et. al., " Comprehensive Modelling Study of Quench Behaviour of the NHMFL 32 T All-Superconducting Magnet System. Input Data and Methodology Aspects.", presented at HTS Modelling 2016, Bologna, Italy, 15-17 June, 2016 (https://events.unibo.it/htsmodelling2016/program).

[9] L Rossi , X Hu, F Kametani, D Abraimov, A Polyanskii, J Jaroszynski and D C Larbalestier, "Sample and length-dependent variability of 77 and 4.2K properties in nominally identical RE123 coated conductors," Supercond. Sci. Technol. 29 (2016) 054006 (9pp).

[10] A.V. Gavrilin, et. al., "Comprehensive quench analysis of the NHMFL 32T all-superconducting magnet", presented at CHATS AS 2015, Bologna, Italy, 14-16 September, 2015.

[11] D. K. Hilton, A. V. Gavrilin, U. P. Trociewitz, "Practical fit functions for transport critical current versus magnitude and angle data from (RE)BCO coated conductors at fixed low temperature and in high magnetic fields," Supercond. Sci. Technol. 28 (2015) 074002 (9pp)

[12] F. Trillaud, H. Palanki, U.P. Trociewitz, S.H. Thompson, H.W. Weijers, J. Schwartz, "Normal zone propagation experiments on HTS composite conductors," Cryogenics 43 (2003) 271279

[13] M. Breschi, M. Casali, L. Cavallucci, G. De Marzi, G. Tomassetti, "Electro Thermal Analysis of a Twisted Stacked YBCO Cable in Conduit Conductor," IEEE Trans. Appl. Supercond., vol. 25, no. 3, 2015.

Chapter 4

Analysis of Quench in the 32 T Magnet

4.1 Introduction

The R&D activity at the NHMFL for the development of the 32 T magnet started in 2007 with the development of the fist SuperPower test coils able to generate 27 T in a background magnetic filed of 19 T generated by a resistive magnet. In 2008, the first prototypes were assembled at the NHMFL and in 2009 the 32 T project was finally funded and officially started, see Table 4.2. The first tests on all superconducting prototypes were performed during the years 2012 -2015. In 2015 the prototypes were tested in the LTS outsert developed by the Oxford Instrument. After preliminary tests during the 2016 at the liquid nitrogen temperature, in 2017 the first tests on the final configuration of the 32 T magnet are performed.

In the previous chapters, the quench tests in the prototypes developed in 2015 and 2016 were analysed and discussed. The first prototype coil developed to analyse the insert of the 32 T magnet is modelled by a quasi 3D FEM approach in chapter 2. In chapter 3, the HTS insert and the coupling with the LTS outsert is widely analysed to determine the overall quench behaviour of a coupled HTS and LTS magnet.

In this chapter, the quasi 3D FEM model is extended to analyse the structure of the 32 T magnet with particular reference to the quench propagation between the different pancakes of the magnet. A set of heater spacers is located between the pancakes in order to initiate quench and determine the transition of the whole magnet. In the test case selected for the present analysis, the HTS insert composed by two REBCO coils is energized with 173 A current and the quench is initiated by heaters in the insert. The contribution of the different pancakes to the transition of the magnet is also studied and discussed to analyse the global quench behaviour of the insert.

Table 4.1:
PROJECT TIME LINE OF THE R&D ACTIVITY
ON THE 32 T MAGNET [5]

	2007	2008	2009	2010	2011	2012	2013	2014	2015	2016	2017
First SP test coil 27 T and 19 T resistive	X										
Second SP test coil		X									
Firs NHMFL test coil 33 T and 31 T resistive		X									
32 T project funded (partially)			X								
More test coils		X	X	X	X	X					
First HTS quench heaters tested						X					
Specification negotiation with SuperPower					X	X	X				
32 T conductor receipt&QA							X	X	X		
Prototype coils						X	X	X	X		
LTS Outsert ordered						X					
LTS Outsert qualified at Oxford Instruments								X			
Prototype testing in LTS outsert									X		
HTS DP winding									X		
HTS coil assembly									X	X	
HTS + LTS integration into cryostat										X	
First LN2 test										X	
Electronics										X	X
4.2 K testing											X

78

4.2 The 32 T Magnet Structure

As described in [1] and [2], the 32 T magnet is composed of a 15 T large-bore LTS outer magnet and a separately powered set of seriesly connected REBCO double pancake coils (40 pancakes for the coil 1 and 72 for the coil 2), generating an additional field of 17 T, see Table . A sketch of the complete structure of the magnet is detailed in Figure 4.1
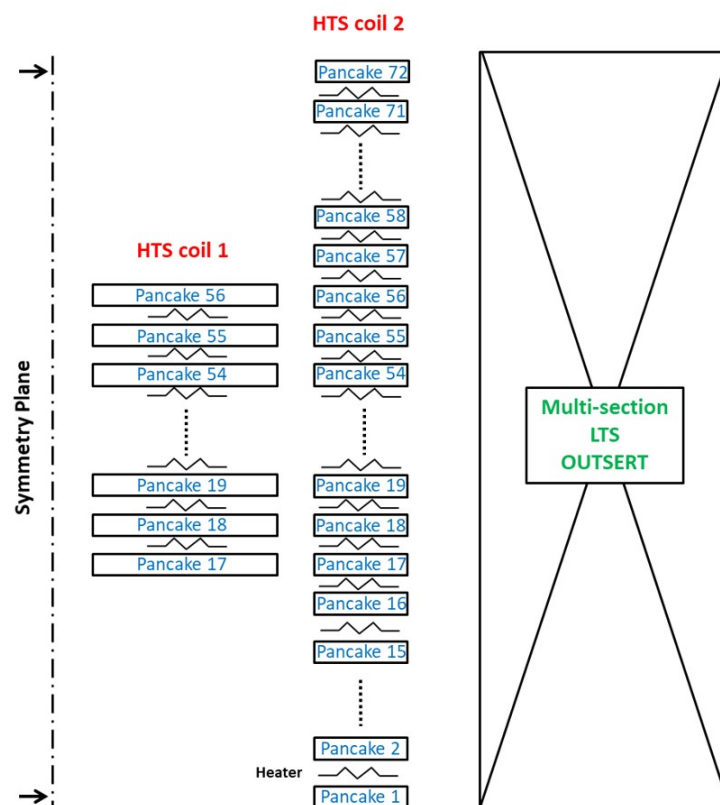

Figure 4.1: Scketch of the 32 T magnet developed at the NHMFL

4.2.1 LTS Outer Magnet

The LTS Outer magnet, shown in Figure 4.2, and its cryostat are provided by the Oxford Instruments and it has passed all acceptance criteria in both factory testing and commissioning tests at the NHMFL. Acceptance criteria included a demonstrated tolerance to a manually induced full-field quench, the ability to ramp from zero to 15.0 T in 60 minutes immediately after re-cooling to 4.2 K, and reach a peak central field of 15.3 T stand-alone. Quench protection system of the LTS outer magnet consists of both a classic passive diode-resistor network and an active system with quench detection, a

Table 4.2:
32 T MAGNET [1]

Parameter	Value
Central Field	32 T
LTS Outsert Field	15 T
HTS Insert Field	17 T
Central Bore	34 mm
Ramp time	1 h
Operating temperature	4.2 K
Stored Energy	8.3 MJ
System weight	2.6 ton

power unit and quench heaters embedded in the coils. The Outsert quench protection can also be triggered manually and by a TTL signal from the REBCO quench detection unit. All LTS coils consist of monolithic conductors, featuring an operating current of 268 A and a self-inductance of 194 H.
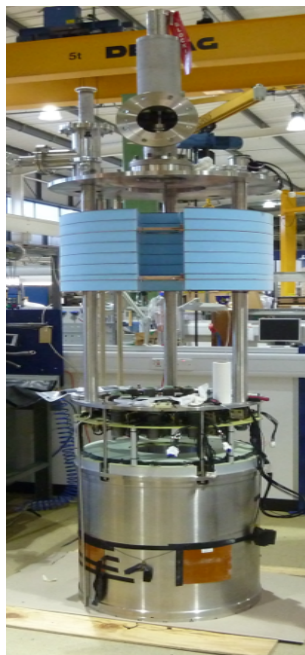

Figure 4.2: Completed LTS Outsert at Oxford Instruments (late 2014) [1]

4.2.2 HTS Insert Magnet

As presented in [2], the REBCO insert coil, shown in Figure 4.3, is composed by two concentric double pancake coil stacks of un-insulated 4-mm

Table 4.3:
REBCO INSERT COILS
TECHNICAL PARAMETERS [1]

	Coil 1	Coil 2
Inner Radius [mm]	20	82
Outer Radius mm]	70	116
Height [mm]	178	318
Number of pancakes	40	72
$I_{operation}$ [A]	174	174
Conductor length [km]	2.9	6.8
Inductance [H]	2.6	9.9
Field contribution [T]	10.7	6.3
Co-wind thickness [μm]	25	50

wide REBCO tape co-wound with insulated stainless steel tape as turn-to-turn insulation [7]. The detail of the structure and operating conditions of the REBCO insert coils are reported in Table 4.3. As discussed in [4] - [7], the choice of two HTS coil stacks represents a balance between the need to limit the radial build per coil (and thereby among others the radial field component) and avoiding an excessive amount of coil components during assembly. Pancake-to-pancake insulation within a module is provided by 0.25 mm G-10 sheets. Each module is vacuum-impregnated with paraffin to reduce the volume of helium within the windings and enhance the mechanical stability of the windings. Quench heaters are sandwiched between protective layers of Kapton and G-10, embedded between double pancake modules. A battery-powered network of such heaters provides quench protection. Sufficiently powerful heaters, in the order of 50 kW for all 32 T heaters combined, can protect HTS coils even in the case of zero normal zone propagation velocity [8], [9], assuming the copper current density in the HTS conductor and the decay rate of the outer magnet in case of a quench are not exceedingly high. The REBCO quench detection unit monitors voltages between different sections of the coils (balance voltage) and is set to trigger at 100 mV, and by a TTL signal from the LTS quench detection system.

4.3 Self-Field Experimental Test

In this chapter, the quasi 3D FEM model described in the chapter 3 is applied to analyse the REBCO insert coils of the 32 T magnet if the insert is energized with 173 A. As in the quench case on the prototypes analysed, the heaters between pancakes (see Figure 4.1) are immediately fired simultaneously for a total duration of 0.8 s. The heaters used to initiate a protected quench are composed of seriesly- connected heater elements embedded be-

(a) Coil 1

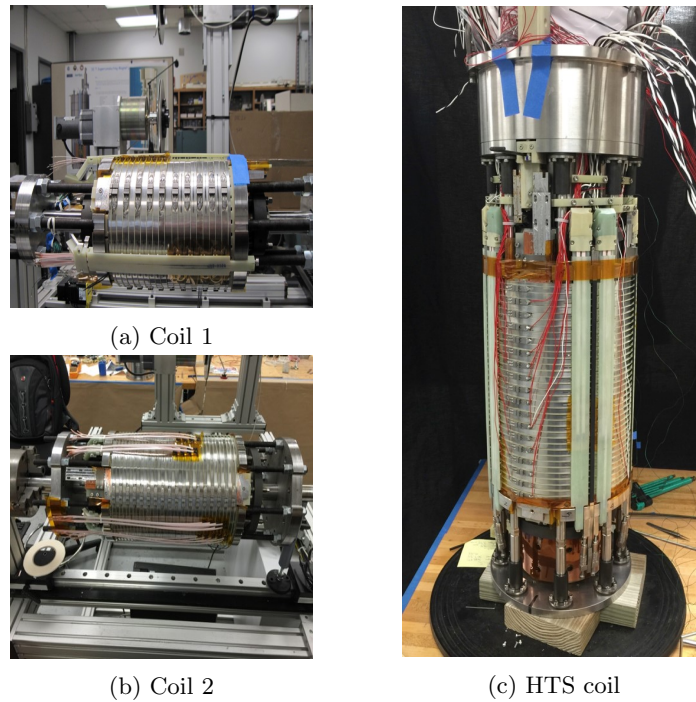(b) Coil 2   (c) HTS coil

Figure 4.3: Detail of the 32 T magnet insert: (a) Coil 1, (b) Coil 2 and (c) complete HTS insert [1]

tween thin G-10 and kapton disks. The structure is the same applied in prototype #2 and shown in the Figure 3.4 of chapter 3. In this experimental case, the outsert is off in order to preliminary test the insert without the coupling with the LTS outsert magnet.

The implementation of the 32 T magnet structure in the quasi 3D FEM model requires the discretization of one single mesh and the resolution of the heat balance equation (see chapter 3) for an array of temperatures, one for each pancake of the coil: $[T_1, ..., T_{72}]$. As shown in Figure 4.1, the variables $T_1, ..., T_{16}$ and $T_{56}, ..., T_{72}$ are solved on a grid corresponding to the 2D geometry of the 2. The variables $T_{17}, ..., T_{55}$ are solved on the mesh grid of both coil 1 and coil 2.

4.4 Result of Self-Field Quench Test

4.4.1 Current Decay

The heat flux introduced by the heaters on the pancakes determines their transition to the normal state. As a consequence of the normal zone propagation, the prototype coil current decreases in time. The current decay computed by the quasi 3D FEM model is shown in Figure 4.4 and compared with the simulation of the experiment performed at the NHMFL by

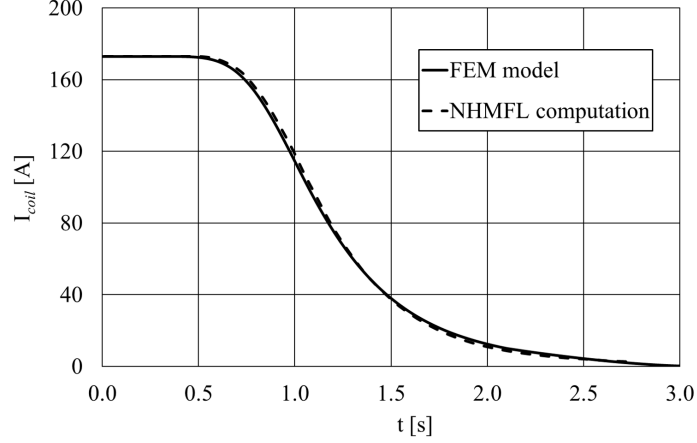the equivalent network circuit model developed by A. Gavrilin [1], [3] and described in chapter **??**

Figure 4.4: Operation current during the quench case at 173 A in the insert coil of the 32 T magnet. The damping of current is computed according to the FEM model presented (see chapters **??** and 3) and the equivalent network circuit developed at the NHMFL [1]- [3]

4.4.2 Pancakes Voltages and Temperatures

The calculation of the resistances of each pancake of the insert, and of its current allow the computation of the terminal voltages of each pancake during the experimental tests as shown in equation 4.1.

$$\Delta V_i(t) = R_i(t)I_{op}(t) + \sum_{j=1}^{N} M_{ij} \frac{dI_{op}}{dt} \qquad (4.1)$$

where ΔV_i is the terminal voltage of the i-th pancake, R_i the resistance of the i-th pancake according to equation 3.2 in chapter 3, I_{op} is the operating current of the seriesly connected pancake and M_{ij} is the mutual induction coeffcient between the i-th and j-th pancake. In Figure 4.5 the terminal voltage distribution between pancakes is shown at t = 1.05 s, a few instants after the heat pulse peak.

Figure 4.6 and Figure 4.7 show the terminal voltages profiles of each pancake of coil 1 during the quench experiment. The two pancakes at the upper and lower position of the coil, namely pancakes #17 and #56, are not directly in contact with the heaters and hence the terminal voltages are dominated by the inductive effect. The resistive effect is predominant in the pancakes from #18 to #31 and from #43 to #55. The behaviour is clearly shown in Figure 4.5. The pancakes in the central zone of the magnet, namely from pancake #32 to #42, subjected to the most intense magnetic flux density, are dominated by the inductive coupling. The result confirms

the conclusion drawn in the previous chapters, i.e. the influence of the field angle on the critical current density and on the quench propagation is of paramount importance. The combination of both field angle and magnetic field intensity determine the most stressed pancakes of the coil 1.

In Figures 4.8 and 4.9, the terminal voltage profile of coil 2 pancakes are shown. As a matter of fact, the pancakes of coil 2 are dominated by the inductive effect. The quench of the magnet is affected more by the transition of the coil 1 than by of coil 2, the contribution of the coil 2 is less relevant.
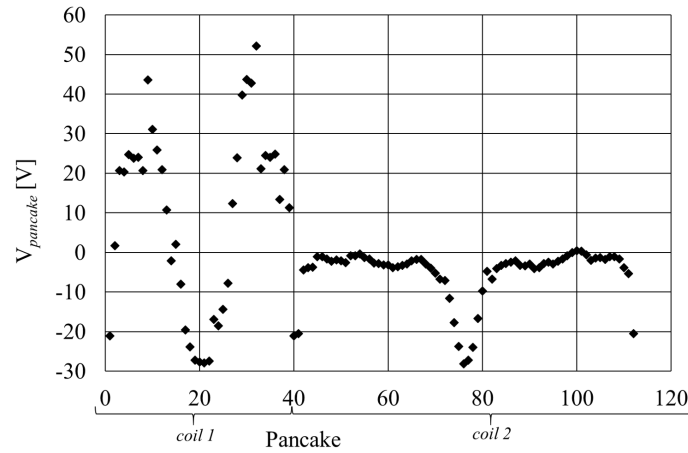
Figure 4.5: Terminal voltage distribution of the coil 1 and coil 2 at t = 1.05 s.

In the Figure 4.10 to Figure 4.15, the temperature distribution on each pancake of coil 1 and coil 2 is shown at t = 1.05 s, a few instants after the heat pulse peak. The heater area is more thermally stressed and the coil 1 is generally characterized by larger hot areas, hence confirming the dominant effect of coil 1 on the quench behaviour of the 32 T magnet.

84
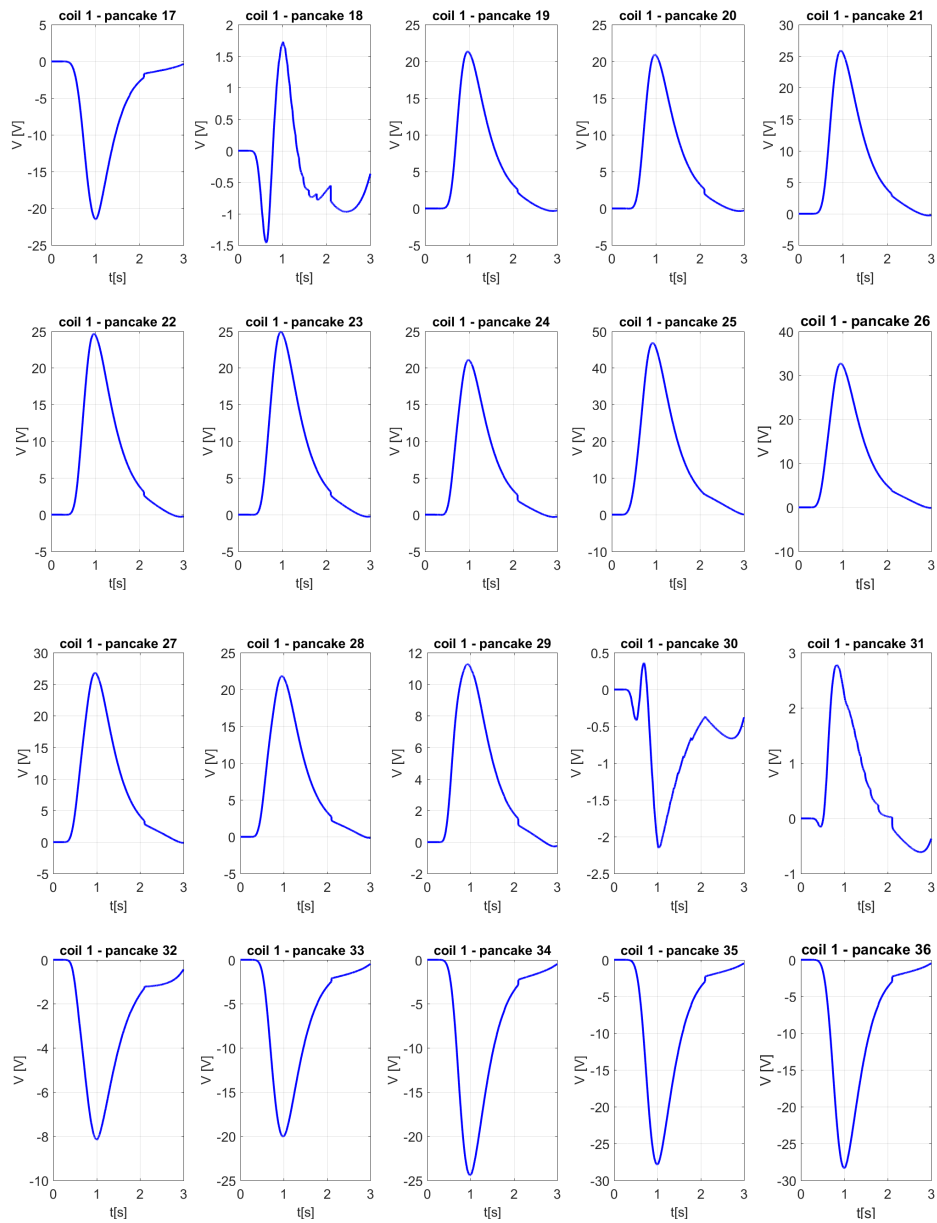
Figure 4.6: Terminal voltage profile of each pancake of coil 1 from pancake #17 to pancake #36
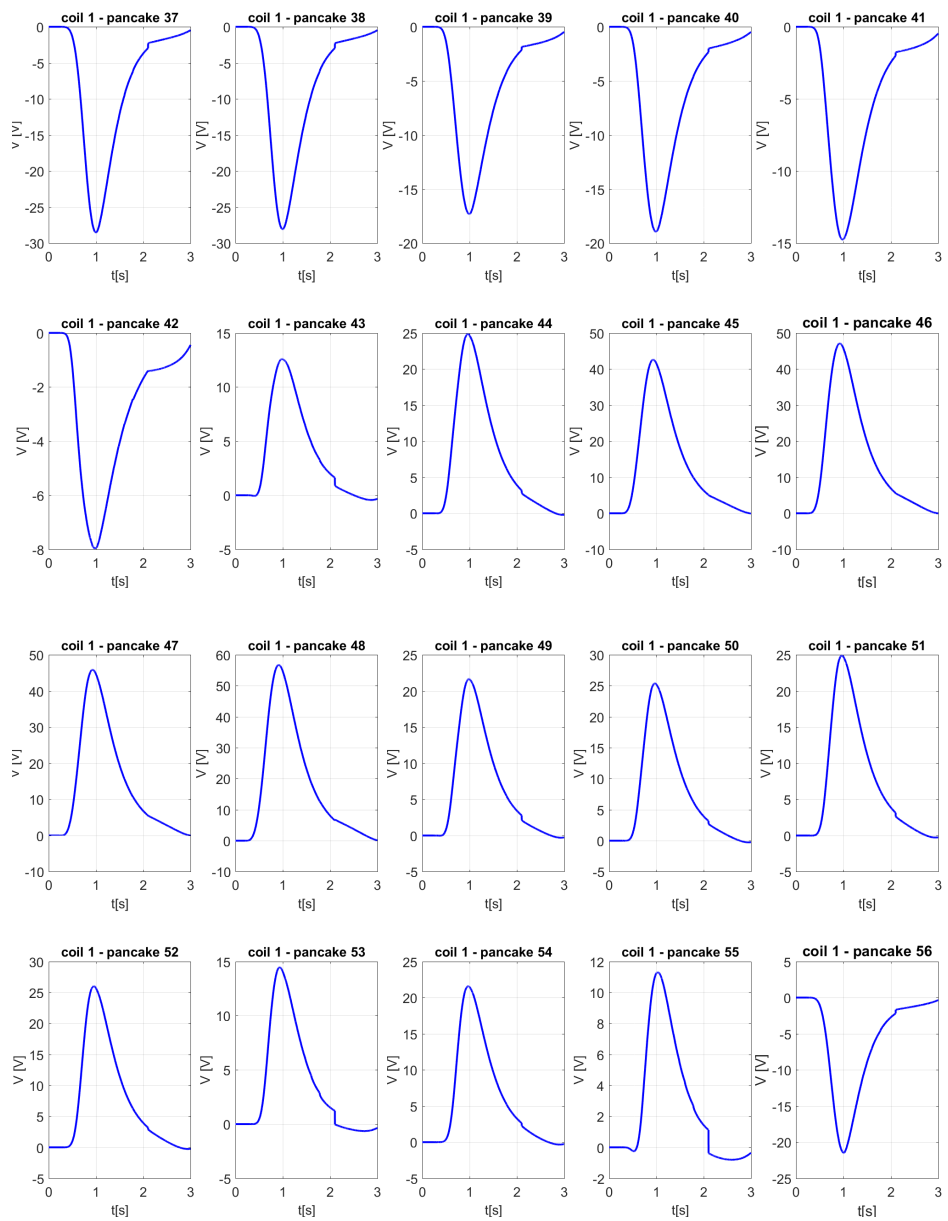
Figure 4.7: Terminal voltage profile of each pancake of coil 1 from pancake #37 to pancake #56
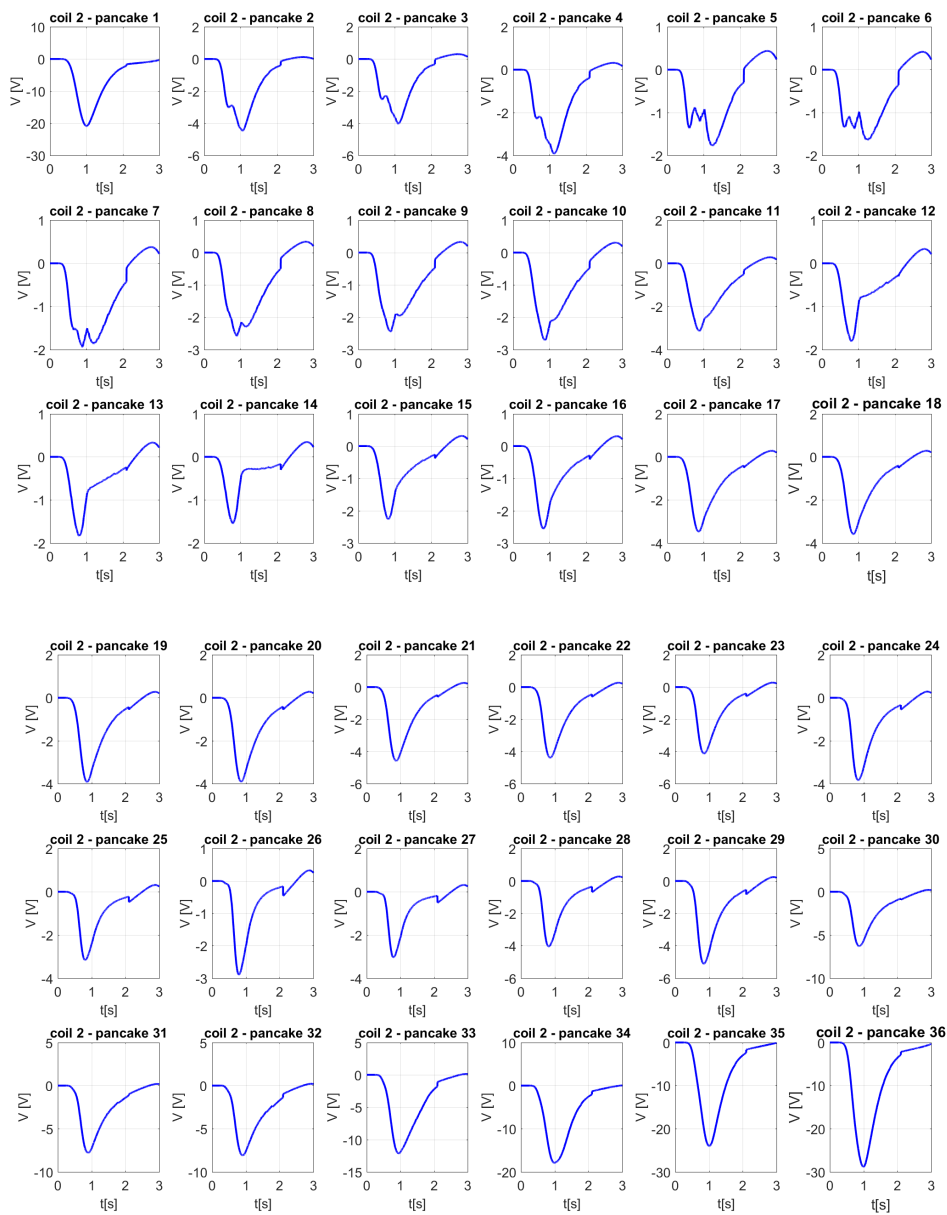
Figure 4.8: Terminal voltage profile of each pancake of coil 2 from pancake #1 to pancake #36
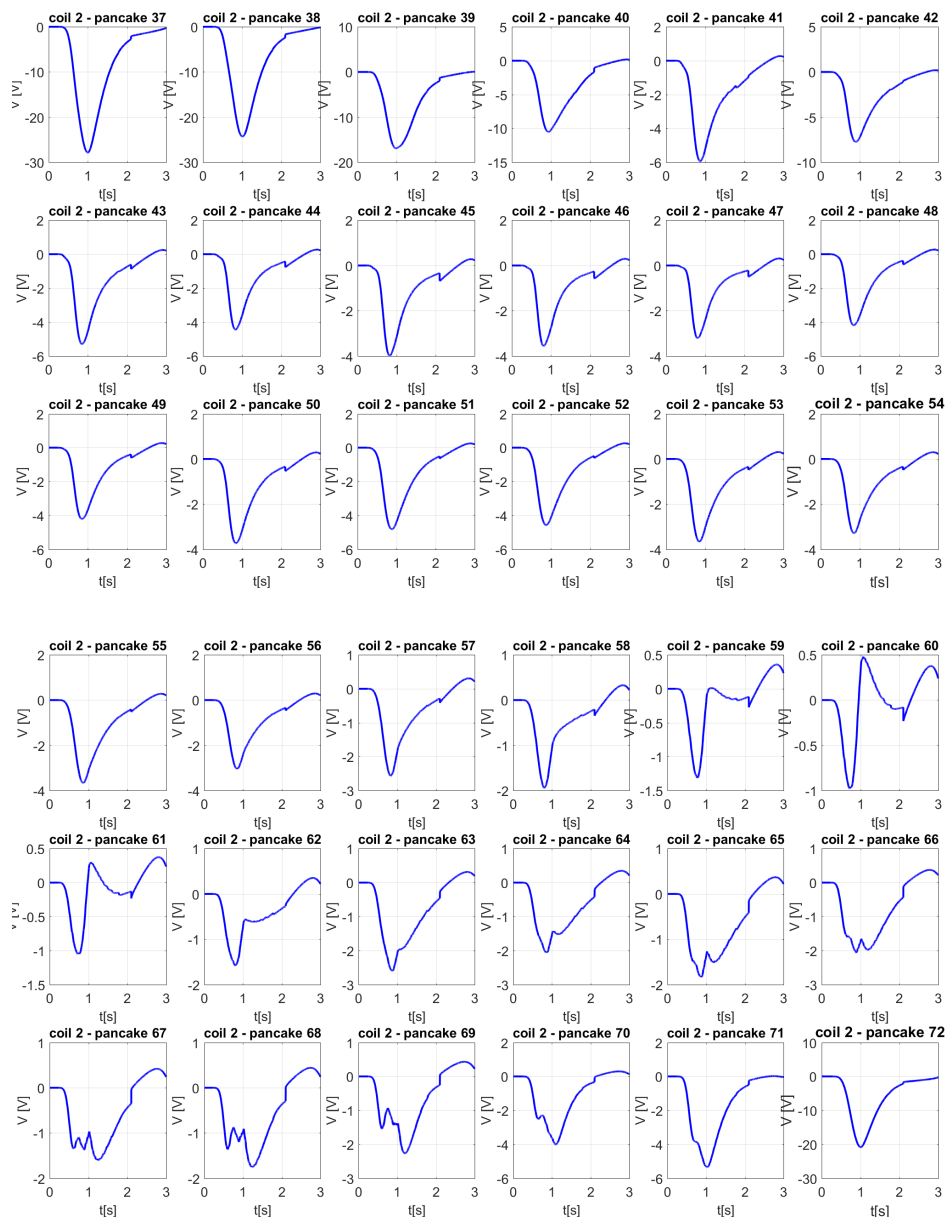
Figure 4.9: Terminal voltage profile of each pancake of coil 2 from pancake #37 to pancake #72
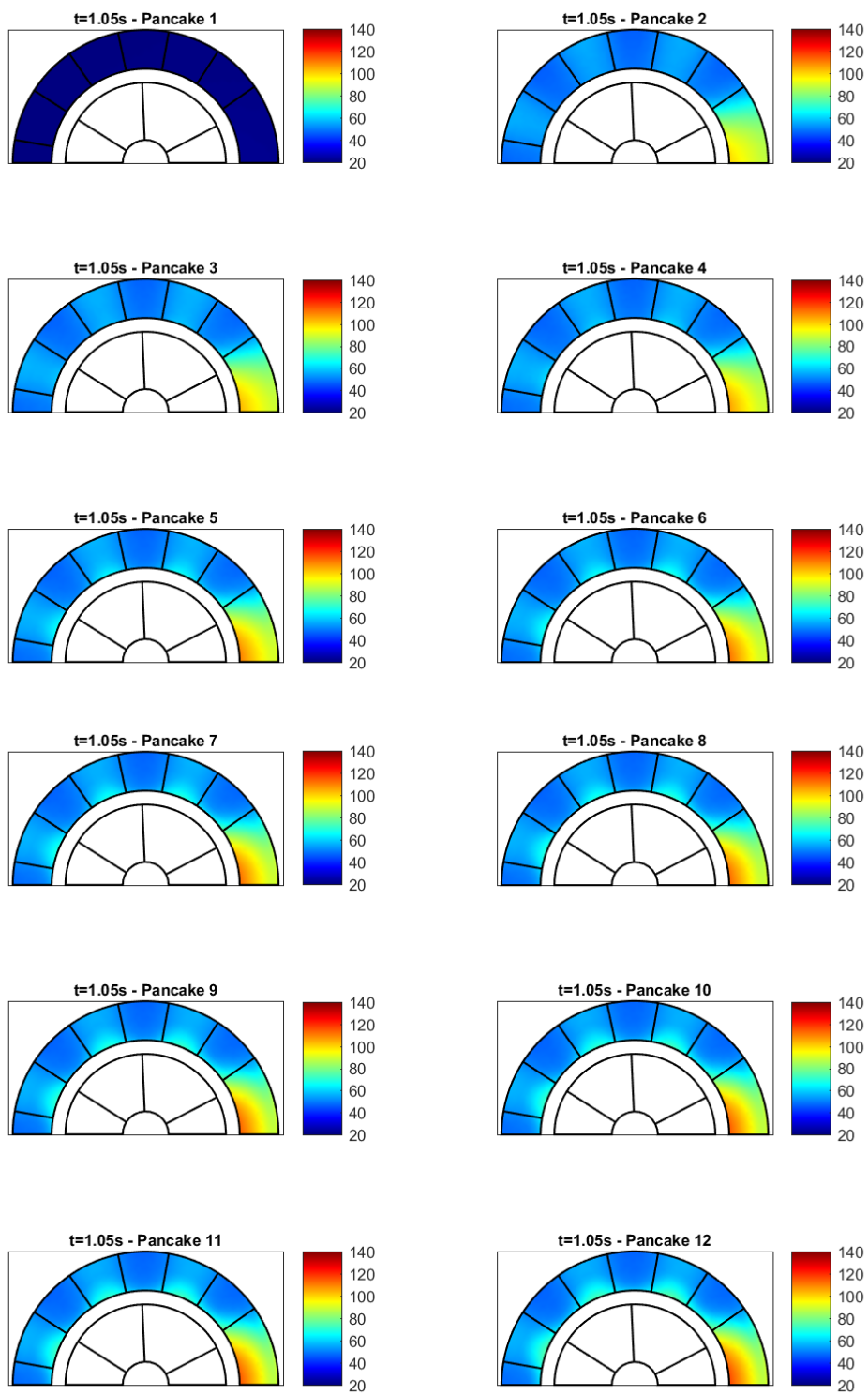
Figure 4.10: Temperature distribution of coils 1 and 2 form pancake #1 to pancake #12

89
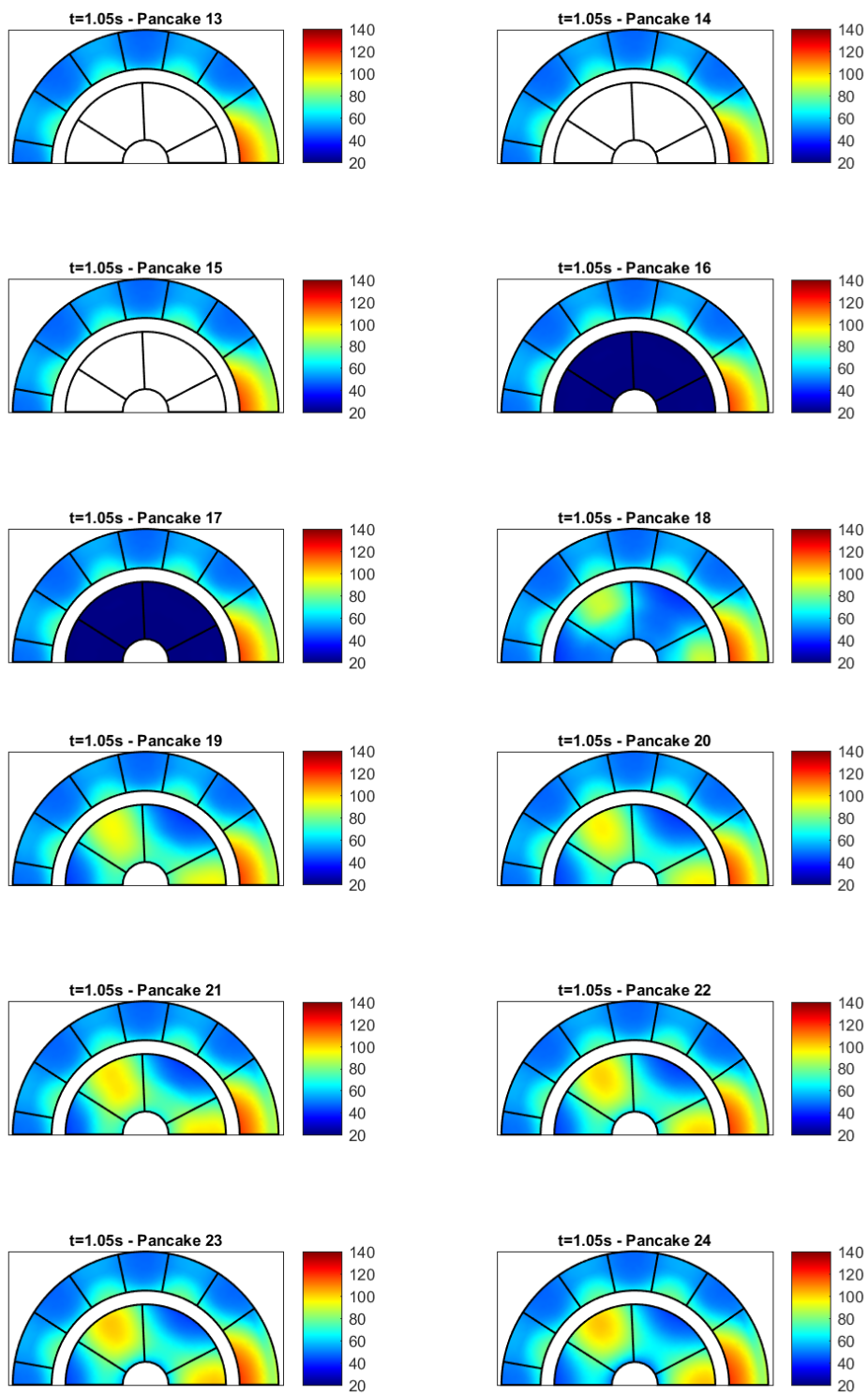
Figure 4.11: Temperature distribution of coils 1 and 2 form pancake #13 to pancake #24

Figure 4.12: Temperature distribution of coils 1 and 2 form pancake #25 to pancake #36

Figure 4.13: Temperature distribution of coils 1 and 2 form pancake #37 to pancake #48

92
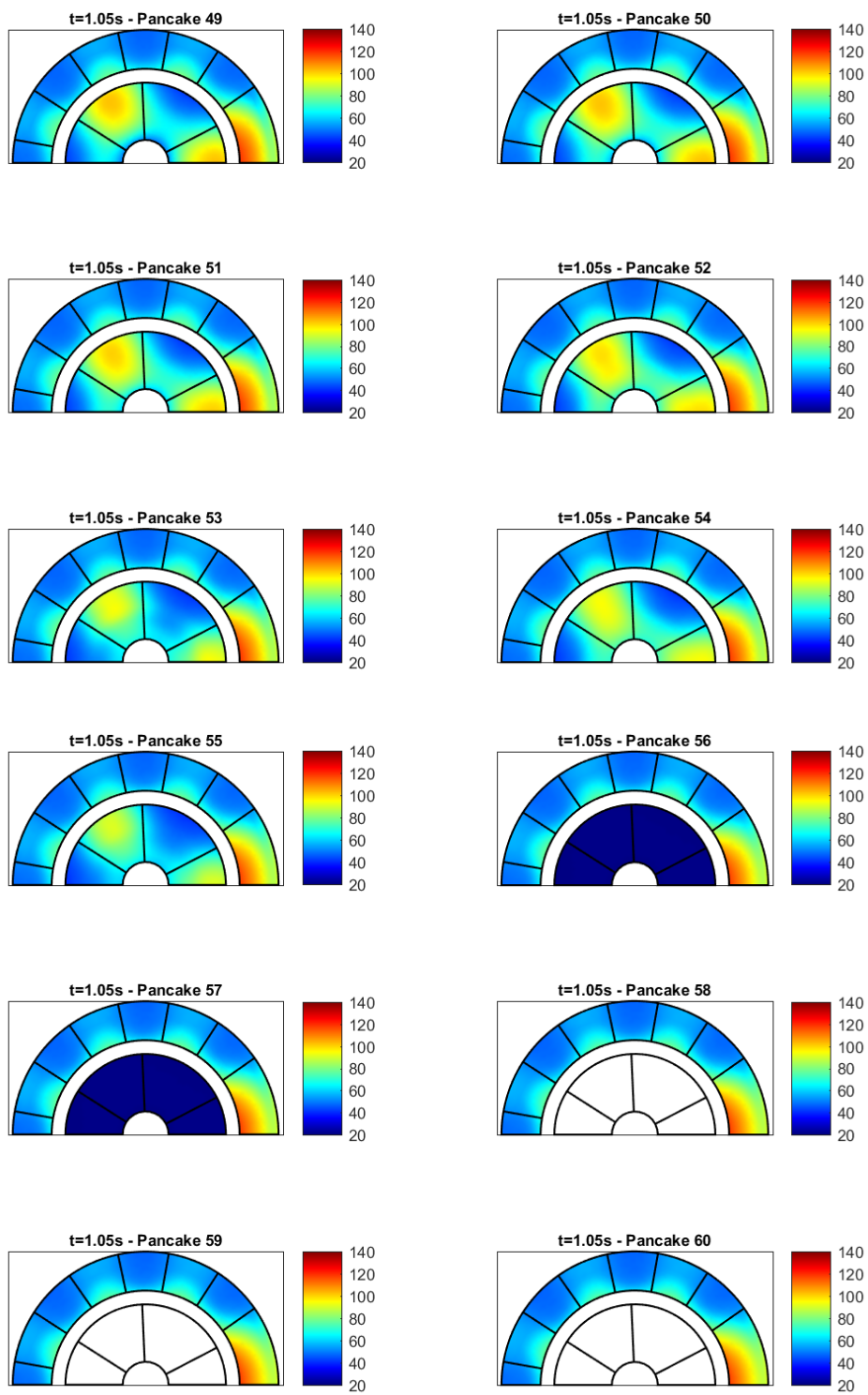
Figure 4.14: Temperature distribution of coils 1 and 2 form pancake #49 to pancake #60
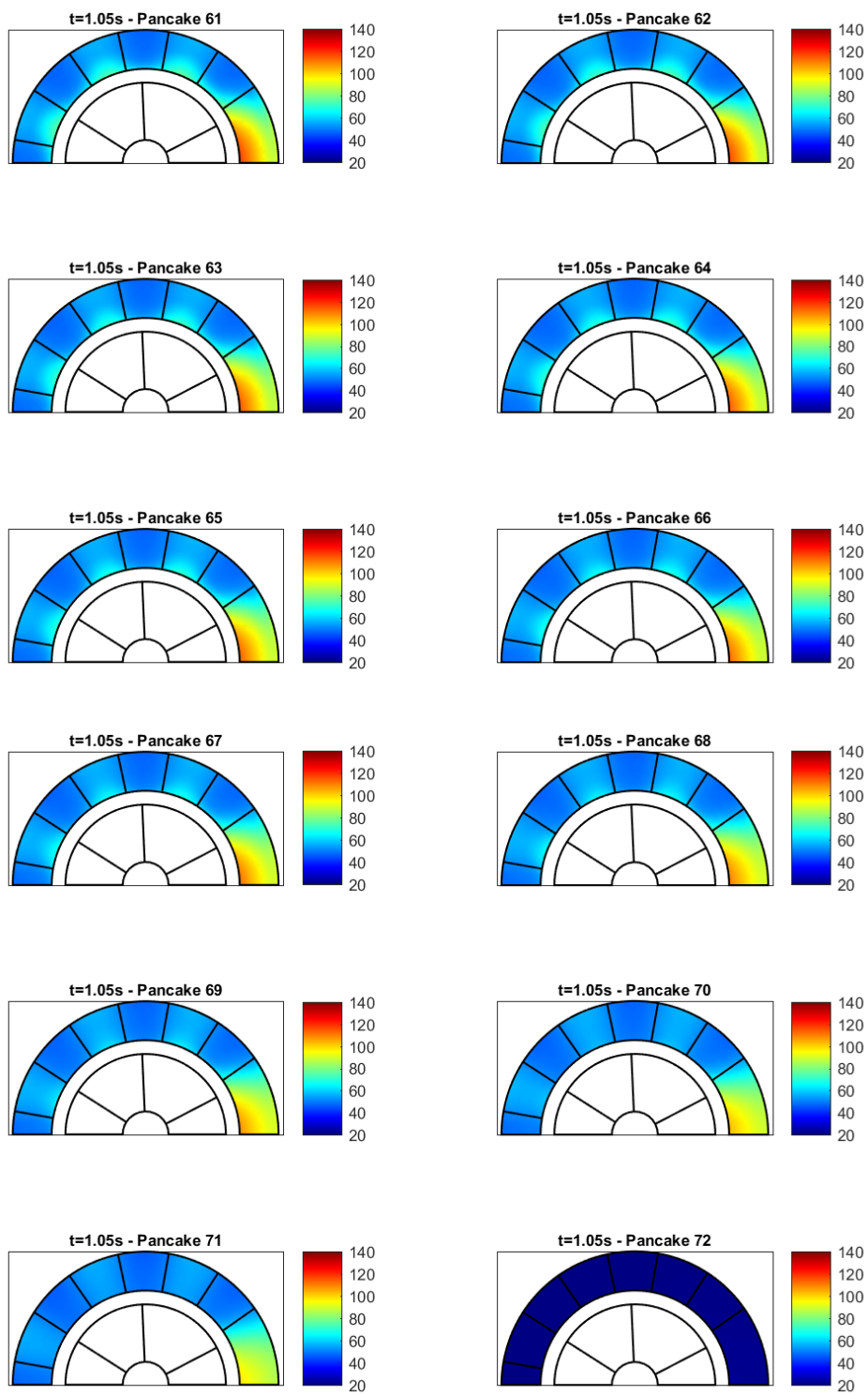
Figure 4.15: Temperature distribution of coils 1 and 2 form pancake #61 to pancake #72

4.4.3 Voltage to Ground

The computation of the voltage to ground is of paramount importance to analyse the global behaviour during the quench of the HTS insert, to design the power supply and the insulation of the magnet and to set the volta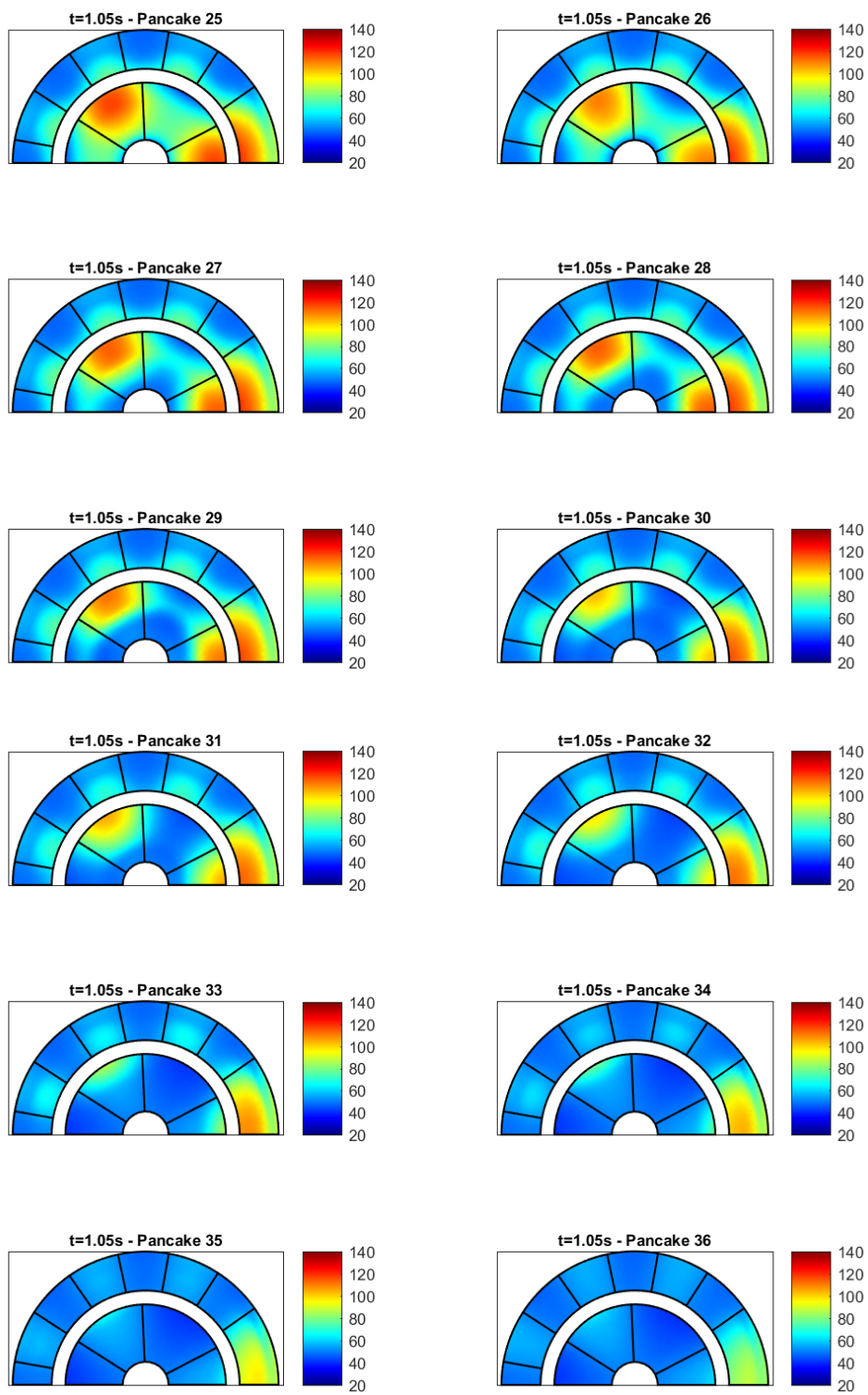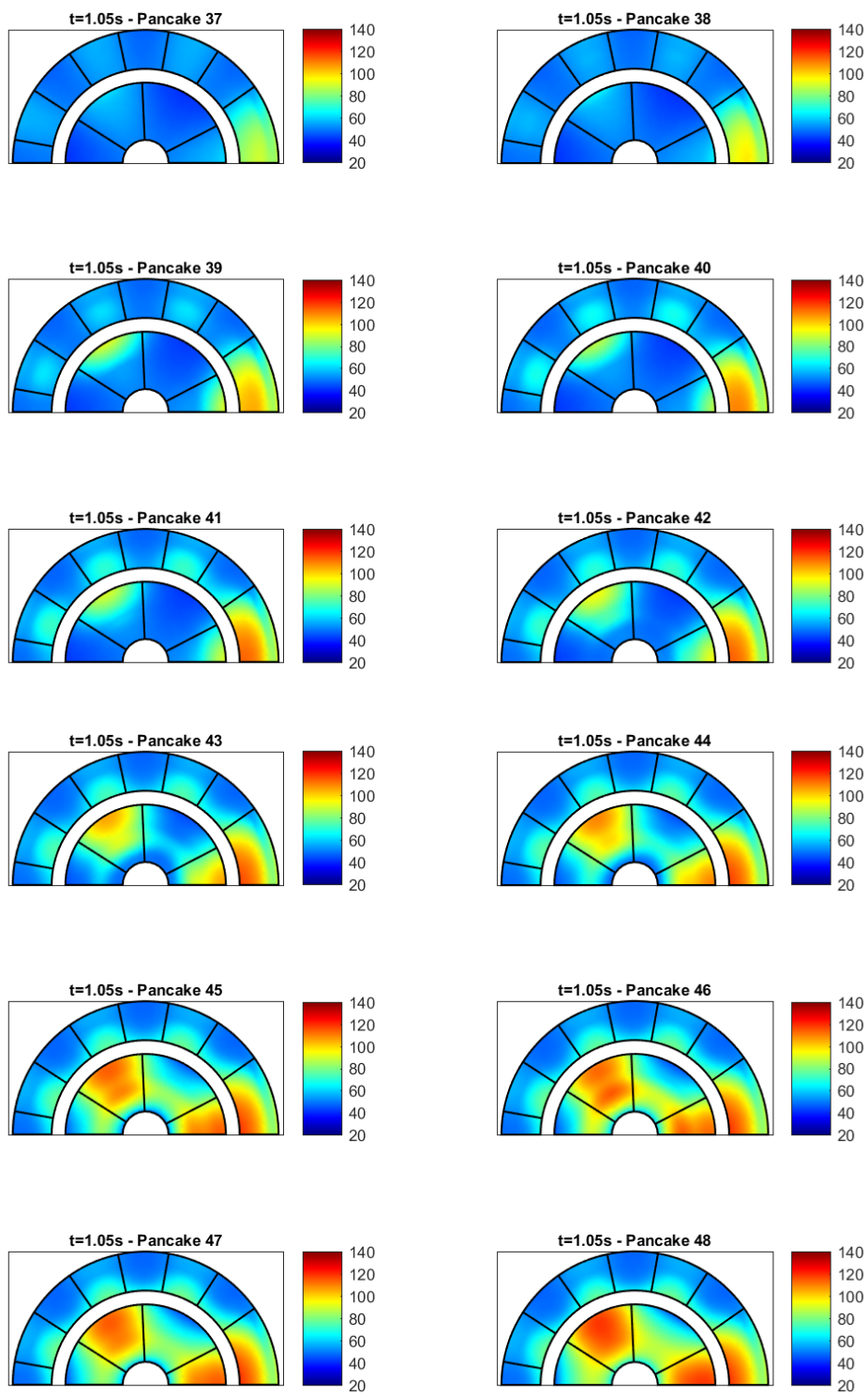ge threshold of the quench detection unit. The first step for the calculation is the computation of the terminal voltages across the pancakes of coil 1 and coil 2 vs time. The terminal voltage of all pancakes of coil 1 and coil 2 are then summed up. In Figure 4.16, the voltage to ground profile is shown. As expected by the constitutive law of the coil described in the equation 3.1 and equation 2.6, the voltage to ground profile is around zero and can be considered as an estimation of the numerical error of the numerical computation.

The voltage to ground distribution between the pancakes at t = 1.05 s is shown in Figure 4.17. The Figure confirms the dominant effect of coil 1 on the global quench behaviour of the magnet.
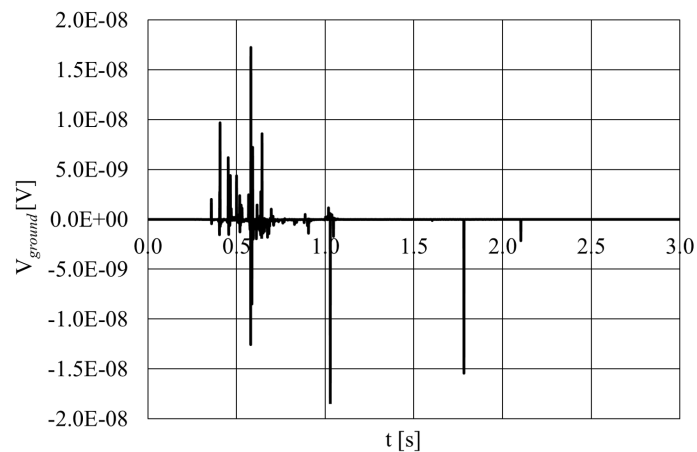
Figure 4.16: Voltage to ground during the quench case at 173 A in the insert coil of the 32 T magnet

4.5 Conclusion

The study of the 32 T magnet insert confirms the possibility of the quasi 3D FEM model to analyse large scale superconducting magnets composed of coil 1 of 40 pancakes and coil 2 of 72 pancakes, a total amount of 112 pancakes. The anisotropic homogenization technique and the reduced dimensionality approaches applied to the analysis of the prototypes presented in the previous chapters is also able to produce reliable results in this last case.

The temperature distribution gives an insight of the hotter areas of each
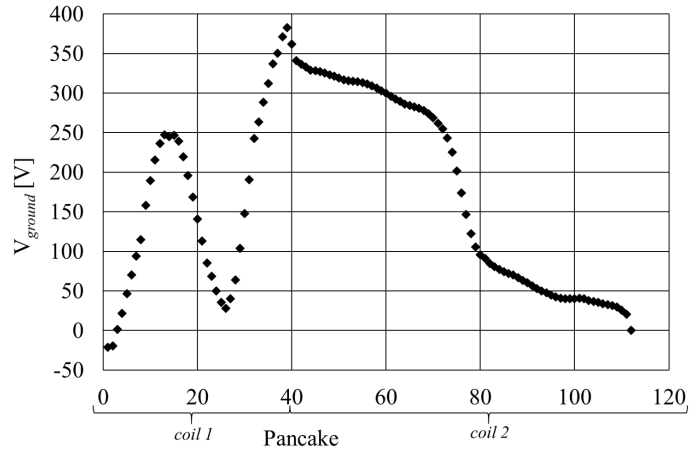
Figure 4.17: Voltage to ground distribution in the insert coil during quench at

pancake during the quench propagation and of the maximum temperature locations during the quench. The terminal voltage of each pancake is computed to globally study the quench development in the magnet. The details of the terminal voltage profile during the quench initiation and propagation clearly show the more stressed pancakes of the insert. The result confirms the conclusions pointed out by the quench studies of the previous experiment: the influence of the field angle on the critical current of the REBCO tapes and consequently on the quench of the HTS coils is of paramount importance. The combination of both field angle and magnetic field intensity determines the most stressed pancakes. The analysis of the results shows the different impact of coil 1 and 2 on the quench of the insert: the coil 1 has a dominant effect on the quench of the global magnet.

The results performed in these quench test confirm the ability of the model to analyse the complete structure of the 32 T magnet in a reasonable computational effort.

Bibliography

[1] H.W. Weijers *et al.*, "The NHMFL 32 T superconducting magnet," presented at the 13th European Conference on Applied Superconductivity EUCAS 2017, Geneva, Swiss, Sept. 1721, 2017.

[2] H. W. Weijers, W. D. Markiewicz, A. V. Gavrilin, A. J. Voran, Y. L. Viouchkov, S. R. Gundlach, P. D. Noyes, D. V. Abraimov, H. Bai, S. T. Hannahs, and T. P. Murphy "Progress in the Development and Construction of a 32-T Superconducting Magnet," *IEEE Trans. Appl. Supercond., vol. 26, no. 4, pp. 4300807, June 2016.*

[3] A. V. Gavrilin *et al.*, "Comprehensive modelling study of quench behaviour of the NHMFL 32 T all-superconducting magnet system. Input data and methodology aspects," presented at the 5th Int. Workshop Numer. Modelling High Temp. Supercond. 2016, Bologna, Italy, Jun. 1517, 2016. [Online]. Available: https://events.unibo.it/htsmodelling2016/program

[4] H. W. Weijers *et al.*, "Progress in the development of a superconducting 32 T magnet with REBCO high field coils," *IEEE Trans. Appl. Supercond., vol. 24, no. 3, Jun. 2015, Art. ID 4301805.*

[5] A. Voran *et al.*, "Design and testing of terminals for REBCO coils of 32 T all superconducting magnet," *IEEE Trans. Appl. Supercond., vol. 24, no. 3, Jun. 2013, Art. ID 4601204*

[6] H. Bai *et al.*, "Impact of trapped helium gas bubble in liquid helium on the cooling in high magnetic field," *IEEE Trans. Appl. Supercond., vol. 25, no. 3, Jun. 2015, Art. ID 4300104.*

[7] J. Lu *et al.*, "Insulation of coated conductors for high field magnet applications," *IEEE Trans. Appl. Supercond., vol. 22, no. 3, Jun. 2012, Art. ID 7700304.*

[8] W. D. Markiewicz, "Protection of HTS coils in the limit of zero quench propagation velocity," *IEEE Trans. Appl. Supercond., vol. 18, no. 2, pp. 13331336, Jun. 2008.*

[9] W. D. Markiewicz, "Quench protection of HTS superconducting magnets," U.S. Patent 7 649 720 B2, 2010.

Chapter 5

Analysis of Quench on REBCO Roebel Cables for the EuCard-2 Project

5.1 Introduction

The Roebel bar technique [1] was applied in superconductivity for the first time to reduce the AC losses in the NbTi Roebel cable of the EURATOM toroidal filed [2]. Roebel bars from HTS materials were introduced for 1G BSCCO tapes and were then developed for HTS transformers [3]. The advantages of the Roebel cables are related to their possibility to carry large transport current with a compact design and a mechanical flexibility. The continuous transposition of the strands reduces the coupling and AC losses ensuring a better current sharing between the strands [4].

The scientific community is studyng with great interest the application of Roebel cables for magnet devices, as in the EuCARD-2 magnet [5] [6], and for AC power devices, as in the development of 1 MVA 3-Phase superconducting transformer [7]. The computation of AC and coupling losses is one of the main challenges for the design of Roebel cables. Therefore, several electromagnetic models are developed for both DC and AC operating conditions, analysing the cable in the frame of a 2D [8] or 3D structure [9] [10] and [11] [12].

The computational models mentioned above neglect the analysis of the thermal behaviour and the study of quench propagation and initiation, fundamental steps in the design, project and protection of HTS superconducting devices [13] [14]. Different studies involving multi-strand quenches in Roebel cables have been published in research theses, for LTS in [15] and for HTS [16].

In this chapter, the same numerical technique used for the modelling of quench in the 32-T magnet is adopted for the analy- sis of quench in HTS
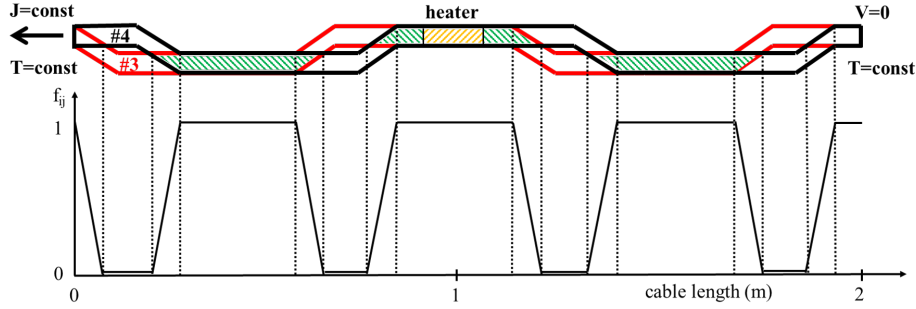
Figure 5.1: Conceptual sketch of heater position, electrical boundary conditions and of the f_{ij} function. For the sake of simplicity only tapes #3 and #4 are represented.

Roebel cables. The homogenization procedure, the discretization of a single mesh grid and solved for an array of variables is here applied at the single tape level. The model, developed in collaboration with the University of Southampton, is able to describe the contact between the different strands of the Roebel cable and to account for the current and thermal heat flux redistribution if a quench is initialized in one or more tapes. The electro-thermal model allows computing the minimum quench energy and the normal zone propagation velocity which defi
ne the thermal and electrical stability of the Roebel cable.

5.2 Model Description

The hereby described thermal and electromagnetic model developed for the analysis of quench in HTS Roebel cables solves the heat balance equation and the current density continuity condition. The thermal and electrical contact between the different tapes is modelled by the introduction of a distributed electrical contact conductance and a distributed thermal contact resistance per unit surface.

In the actual implementation, only one 1D tape is discretized with a mesh extended along the length of the cable. A set of thermal and electrical equations is written for an array of variables and solved for the implemented mesh: the elements of the array are the temperature and electrical potentials of all tapes.

The tape is described as a homogeneous conductor: the different layers of the tape are homogenized to determine uniform thermal and electrical material properties.

5.2.1 Thermal Model

As already mentioned, only one tape is discretized and a set of heat balance equations is solved for an array of temperatures $[T_1, \cdots, T_{N_t}]$ representing

99

the temperatures of all the number of tapes N_t.

The thermal equation can be written for the i-th tape as $(i = 1, \cdots, N_t)$:

$$\rho \, C_p(T_i(x,t)) \, \frac{\partial T_i(x,t)}{\partial t} - \frac{\partial}{\partial x} \left(k(T_i(x,t)) \, \frac{\partial T_i(x,t)}{\partial x} \right) =$$

$$\sigma_i \left(T_i(x,t), E_i(x,t) \right) \left(\frac{\partial V_i(x,t)}{\partial x} \right)^2 + \sum_j Q^J_{i,j}(x,t) +$$

$$+ \sum_j Q^c_{i,j}(x,t) + Q^h_i(x,t) \tag{5.1}$$

where $T_i(x)$ is the temperature in the i-th tape as a function of the position, $\rho \; [\mathrm{kg/m^3}]$ the homogenized density, $C_p(T_i) \; [\mathrm{J/(kg\,K)}]$ the temperature dependent homogenized specific heat, $k(T_i) \; [\mathrm{W/(m\,K)}]$ the temperature dependent longitudinal thermal conductivity, $\sigma_i \left(T_i(x,t), E_i(x,t) \right) \; [\mathrm{S/m}]$ is the homogenized longitudinal electrical conductivity as a function of the temperature and electric field of the i-th tape. In the heat balance equation, the term $Q^J_{i,j}$ represent the Joule power due to the current exchange between the i-th and j-th tapes in contact:

$$Q^J_{i,j} = \sum_j \frac{1}{2} \, f_{i,j}(x) \, \sigma^c_{el} \, \frac{(V_i - V_j)^2}{\delta} \tag{5.2}$$

where $f_{i,j}(x)$ is a function oscillating between zero and one that takes in account the contact area between the i-th and the j-th tapes. The function is equal to one if the two tapes overlap while zero if they are not in contact. A conceptual sketch of the contact area between two tapes and of the f_{ij} function is shown in Figure 5.1. The parameter $\sigma^c_{el} \; [\mathrm{S/m^2}]$ is the distributed electrical contact conductance per unit surface between the two tapes and δ the thickness of the tape. The term $Q^J_{i,j}$ is computed supposing that the Joule power due to current exchange is equally split between the i-th and j-th tapes. The thermal power $Q^c_{i,j}$ exchanged between the i-th tape and the adjacent tapes is modelled as:

$$Q^c_{i,j} = \sum_j f_{i,j}(x) \frac{T_i - T_j}{R^c_{th} \, \delta} \tag{5.3}$$

where $R^c_{th} \; [\mathrm{m^2\,K/W}]$ is the distributed thermal contact resistance per unit surface between the two tapes and δ the thickness of the tape.

The thermal disturbance introduced by a heater located at half length of tape #4, as shown in Fig. 5.1, is modelled by the term $Q^h_i(x,t)$.

As boundary conditions, the temperature is fixed at the two terminals of each tape that compose the cable. The same temperature is introduced as initial condition.

5.2.2 Electrical Model

The electrical model of the Roebel cable is based on a set of equations solved for an array of variables representing the electric potentials $[V_1, \cdots, V_{N_t}]$ of all the tapes computed with respect to a reference location located at the end of the cable where the electric potential is set to zero. On the other terminal the current density is imposed at a fixed value, see Figure 5.1.

The current density continuity condition can be written for the i-th tape as ($i = 1, \cdots, N_t$):

$$\frac{\partial}{\partial x}\left(-\sigma_i\left(T_i(x,t), E_i(x,t)\right)\frac{\partial V_i(x,t)}{\partial x}\right) = \sum_j f_{i,j}(x)\ \sigma_{el}^c\ \frac{V_j(x,t) - V_i(x,t)}{\delta} \tag{5.4}$$

These equations take into account the current redistribution between the tapes in contact via the distributed electrical contact conductance per unit surface σ_{el}^c.

5.2.3 Homogenization Procedure

In order to avoid the discretization of each layer of a tape, a homogenization procedure is applied to calculate the longitudinal thermal and electrical conductivities. The electrical conductivity σ_i of the i-th tape is computed assuming all the number of layers (N_l) of the tape as in parallel connection. The homogenized electrical conductivity is determined by:

$$\sigma_i = \frac{I_c(T_i)}{E_c\ S_{tot}}\ \left(\frac{1}{E_c}\frac{\partial V_i(x,t)}{\partial x}\right)^{\frac{1-n}{n}} + \sum_{j=1}^{N_l} \sigma_j(T_i(x,t))\ \frac{S_j}{S_{tot}} \tag{5.5}$$

where $I_c(T_i)$ is the critical current as a function of the temperature in the i-th tape [22], E_c is the critical electric field set to $1 \times 10^{-4}\,\mathrm{V/m}$, n is the n-value of the power law set to 20, S_{tot} is the total cross section of the tape, S_j is the cross section of the j-th layer of the tape and σ_j is the electrical conductivity as a function of the temperature in the i-th tape.

A similar procedure is adopted for the calculation of the longitudinal thermal conductivity k_i of the i-th tape.

5.3 Results

The model previously described is applied in this section to the study of quench on a 2 m-long Roebel cable composed by 15 tapes with a twist pitch of 226 mm. The tapes of the cable are produced by the company Brucker (USA) for the EuCARD2 project and the cables is assembled by the Karlsruhe
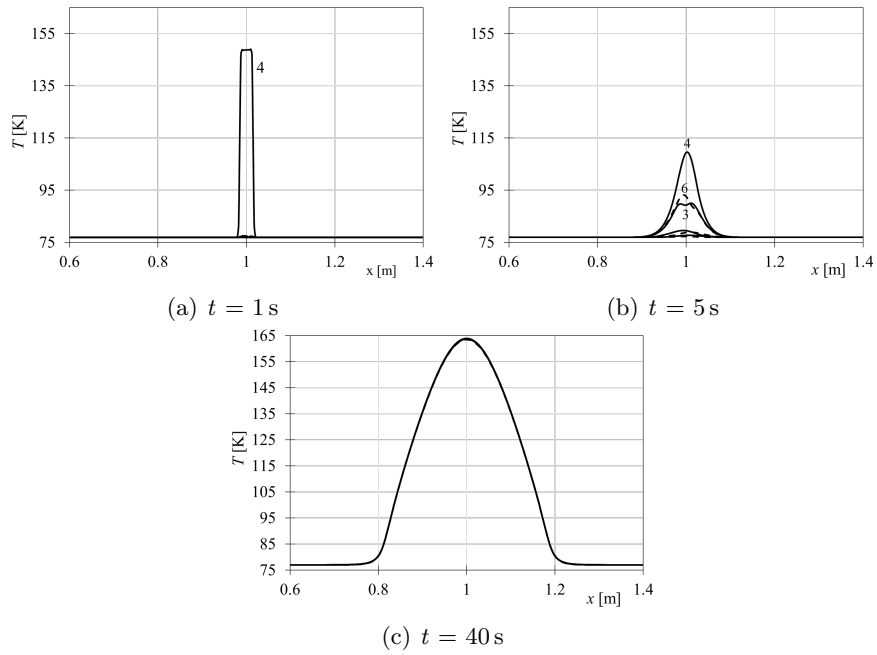
(a) $t = 1\,\mathrm{s}$

(b) $t = 5\,\mathrm{s}$

(c) $t = 40\,\mathrm{s}$

Figure 5.2: Temperature distribution along the tapes at (a) $t = 1\,\mathrm{s}$, (b) $t = 5\,\mathrm{s}$ and (c) $t = 40\,\mathrm{s}$.
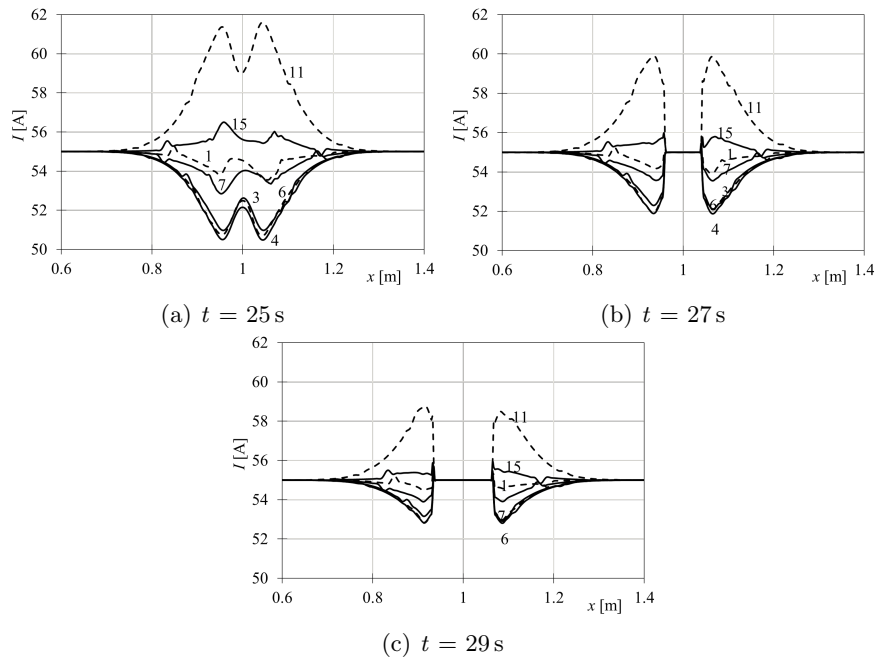
(a) $t = 25\,\mathrm{s}$

(b) $t = 27\,\mathrm{s}$

(c) $t = 29\,\mathrm{s}$

Figure 5.3: Current distribution along the tapes at (a) $t = 25\,\mathrm{s}$, (b) $t = 27\,\mathrm{s}$ and (c) $t = 29\,\mathrm{s}$.

102
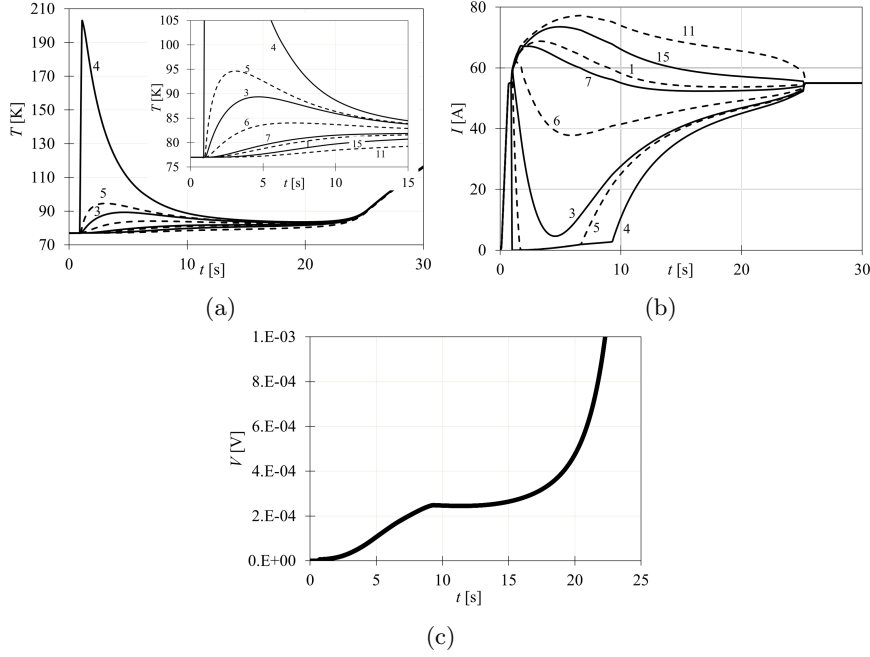
Figure 5.4: (a) Tape temperature, (b) tape current evolution and (c) electric potential evolution in time at $x = 1\,\text{m}$ during a quench simulation with transport current of $55\,\text{A}$ and input energy of $128\,\text{J}$.

Institute of Technology KIT (Germany). The original 2G YBCO tape has a critical current of $130\,\text{A}$ at $77\,\text{K}$ and self-field. This value is homogeneous along the tape length within a range of $\pm\,10\%$. The punched strand exhibits a reduction of performance, with a critical current $I_c \sim 65\,\text{A}$ at $77\,\text{K}$ in self field [22] [23]. These experimental values are implemented in the model [22].

In the present study, the distributed electrical contact conductance σ_{el}^{c} is set to $1 \times 10^{12}\,\text{S/m}^2$ and the distributed thermal contact resistance to $1 \times 10^{-2}\,\text{K}\,\text{m}^2/\text{W}$. Transforming the value of distributed electrical contact conductance per unit surface σ_{el}^{c} to a lumped resistance R_a, the value found is $8 \times 10^{-8}\,\Omega$, which is line with the experimental data presented in [22].

5.3.1 Quench Analysis

In the quench case hereby described, one terminal of each tape is energized with a transport current of $55\,\text{A}$ and a 77-K temperature is imposed as initial and boundary conditions at the terminals. To analyse the effect of the boundary conditions, a convergence study was performed by reducing the length of the cable. For a cable length of $2\,\text{m}$, the boundary conditions do not affect the solution of the problem presented in this work.

The quench is initialized by a triangular pulse starting at $t = 0.95\,\text{s}$ and lasting $1\,\text{s}$ with a peak power of $7.2 \times 10^9\,\text{W/m}^3$ and a total amount of energy

of 128 J. The virtual quench heater is 3 cm long and located in the middle of tape #4. Fig. 5.2 shows the temperature along selected tapes (namely tapes #1, #3, #4, #5, #6, #7, #11, #15) at different time instants. The temperature of tape #4 rises up due to the heater pulse (Fig. 5.2a). After a few seconds the temperature redistributes (Fig. 5.2b) and at $t = 40$ s all tapes exhibit the same temperature (Fig. 5.2c). The profile clearly shows the complete quench of the cable.

The current redistribution along the cable at different time instants, reported in Fig. 5.3, shows the complete transition to the normal state of the central zone, which is the most stressed area of the cable. In that zone, the tapes are in normal state and the currents in all tapes are forced to flow on the metallic matrices as indicated by the same current (55 A) near the zone. This results in large Joule heating, rising the peak temperature of the central zone.

The evolution of the current distribution during the quench initiation and propagation is shown in Fig. 5.3. Computing the Normal Zone Propagation Velocity from the data reported in Figs. 5.3a and 5.3b gives a value of 6 cm/s in line with results reported in [19] [20].

The temperature evolution at $x = 1$ m is shown in Fig. 5.4a for selected tapes. The details of the temperature distribution in the range from 70 K to 100 K is given in the inset of Fig. 5.4a. The temperature of tape #4 rises up to a peak value of about 200 K due to the heater disturbance. The tapes with temperatures higher than the current sharing temperature become resistive and thus carry a current lower than the transport current of 55 A. The current in these tapes decreases and redistributes towards the neighboring ones (see Fig. 5.4b). After about 25 s, the temperature of the tapes rises up irreversibly due to the Joule effect.

As shown in Fig. 5.4c, the electric potential of selected tapes at $x = 1$ m with respect to the reference location rises irreversible around $t = 20$ s. It is worth nothing that the tapes exhibit the same electric potential profile: the current redistribution between them maintains the overall electric potential constant. The quench decision time shown in Fig. 5.4c is in line with the experimental values presented in [22].

In case of recovery, the temperature profile is reported in Fig. 5.5 for a peak power of 7.0×10^9 W/m^3 and a total energy of 125 J. After a quench decision time of about 20 s, a change of slope can be observed in the tape temperatures.

5.3.2 Quench Energy

The Quench Energy QE for different Roebel configurations is shown in Fig. 5.6 as a function of $i = I/I_c$.

The QE is computed for the 15-tape cable in the case of 3 and 10 cm long heater. In the 3-cm case, for transport current below 55 A ($1 - i < 0.2$),
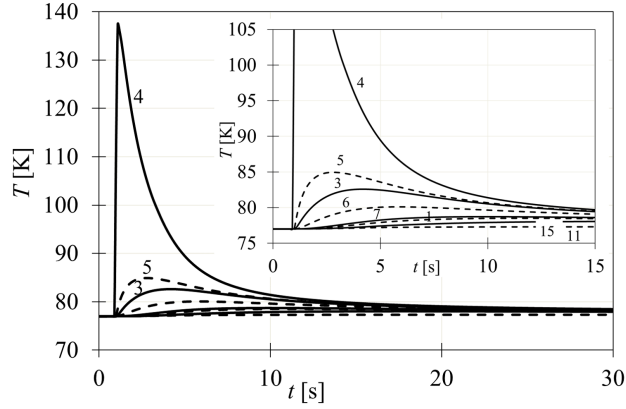
Figure 5.5: Tape temperature evolution in time at $x = 1\,\mathrm{m}$ during a quench simulation with transport current of $55\,\mathrm{A}$ and input energy of $125\,\mathrm{J}$.
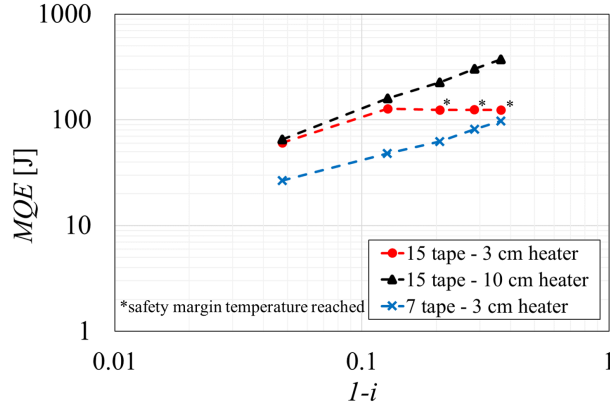
Figure 5.6: Quench Energy of the Roebel cable with different configurations at 77 K.

the working point is far from the critical surface and the Joule effect is not sufficient for the quench propagation over the whole cable. The temperature increases due to the heater pulse and, after the pulse, the temperature decreases to the nominal values. The data points characterized by this behaviour are marked with an asterisk in Fig. 5.6 and the QE is computed as the energy required to reach a threshold temperature of $200\,\mathrm{K}$ at the hot-spot location. In order to deposit an amount of energy avoiding the exceeding of the safety temperature, the heater length is increased to $10\,\mathrm{cm}$.

To analyse the impact on the QE of the total number of tapes, the QE is also presented in Fig. 5.6 for a Roebel cable assembled by 7 tapes. Fig. 5.6 shows the effect of the number of tapes: the QE in the 15-tape cable is increased more than a factor 2.5 with respect to the 7-tape cable.

5.4 Conclusion

A novel approach for the analysis of quench and thermal stability of HTS Roebel cable is developed in the frame of a quasi-3D electro-thermal FEM model. Each tape of the Roebel cable is modelled by a reduced dimensionality approach as a 1D pattern thermally and electrically in contact with the others by distributed contact thermal resistances and electrical conductance per unit surface.

The model is hereby applied for the analysis of quench in a 15-tape Roebel cable for the EuCARD-2 project. The quench case presented points out the current sharing and the temperature redistribution between tapes during quench disturbance. If compared with the LTS cables, the low Normal Zone Velocity equal to $6\,\mathrm{cm/s}$ increases the quench detection time strongly influencing the design of safety protection systems for the Roebel devices.

As a consequence of the higher heat capacity and of the current and heat redistribution, the 15-tape cable exhibits Quench Energy greater by a factor 2.5 with respect to the 7-tape cable.

The comfortable results of the quasi-3D electro-thermal model make the authors confident for further improvements. The effect on quench of the current redistribution through the terminals at the ends of the cable and the influence of the self-filed on the critical current parametrization are further investigated. Future applications for the study of quench and current redistribution are analysed not only in HTS Roebel cable but also in HTS insulated coils wound with the Roebel bar technique.

Bibliography

[1] German Patent: Ludwing Roebel (BBC company) 19th March 1912.

[2] D. S. Beard, W. Klose, S. Shimamoto and G. Vescey "The IEA large coil task Fusion," *Eng. Des.* 7 2353, 1988

[3] M. Leghissa, V. Hussennether and H. W. Neumueller "kA-class high-current HTS conductors and windings for large scale applications," *CIMTEC 2006: 5th Int. Conf. on Science and Engineering of Novel Superconductors (Acireale, June) published in Proceedings*

[4] W. Goldacker1, A. Frank, A. Kudymow, R. Heller, A. Kling, S. Terzieva and C. Schmidt, "Status of high transport current ROEBEL assembled coated conductor cables," *Supercond. Sci. Technol. 22 (2009) 034003 (10pp).*

[5] L. Rossi, A. Badel, M. Bajko, A. Ballarino, L. Bottura, M. M. J. Dhall, M. Durante, Ph. Fazilleau, J. Fleiter, W. Goldacker, E. Hr, A. Kario, G. Kirby, C. Lorin, J. van Nugteren, G. de Rijk, T. Salmi, C. Senatore, A. Stenvall, P. Tixador, A. Usoskin, G. Volpini, Y. Yang, N. Zangenberg, "The EuCARD-2 Future Magnets European Collaboration for Accelerator-Quality HTS Magnets," *IEEE Trans. Appl. Supercond., vol. 25, no. 3, Jun. 2015*

[6] G. A. Kirby, J. van Nugteren, A. Ballarino, L. Bottura, N. Chouika, S. Clement, V. Datskov, L. Fajardo, J. Fleiter, R. Gauthier, L. Gentini, L. Lambert, M. Lopes, J. C. Perez, G. de Rijk, A. Rijllart, L. Rossi, H. ten Kate, M. Durante, P. Fazilleau, C. Lorin, E. Hr, A. Stenvall, S. Caspi, M. Marchevsky, W. Goldacker, and A. Kario, "Accelerator-Quality HTS Dipole Magnet Demonstrator Designs for the EuCARD-2 5-T 40-mm Clear Aperture Magnet," *IEEE Trans. Appl. Supercond., vol. 25, no. 3, Jun. 2015*

[7] N. Glasson, M. Staines, R. Buckley, M. Pannu, and S. Kalsi, "Development of a 1 MVA 3-Phase Superconducting Transformer Using YBCO Roebel Cable," *IEEE Trans. Appl. Supercond., vol. 21, no. 3, Jun. 2011*

[8] J. Fleiter, A. Ballarino, L. Bottura, W. Goldacker, and A. Kario, "Characterization of Roebel Cables for Potential Use in High-Field Magnets," *IEEE Trans. Appl. Supercond., vol. 25, no. 3, Jun. 2015*

[9] V. Zermeno, F. Grilli1 and F. Sirois, "A full 3D time-dependent electromagnetic model for Roebel cables," *Supercond. Sci. Technol. 26 (2013) 052001 (8pp)*

[10] F. Grilli, V. Zermeno, M. Vojenciak, E. Pardo, A. Kario and W. Goldacker, "AC Losses of Pancake Coils Made of Roebel Cable," *IEEE Trans. Appl. Supercond., vol. 23, no. 3, Jun. 2013*

[11] Naoyuki Amemiya, Tadaaki Tsukamoto1, Masahiro Nii1, Takashi Komeda1, Taketsune Nakamura1 Zhenan Jiang, "Alternating current loss characteristics of a Roebel cable consisting of coated conductors and a three-dimensional structure," *Supercond. Sci. Technol. 27 (2014) 035007 (16pp)*

[12] M. Nii, N. Amemiya and T. Nakamura, "Corrigendum: Three-dimensional model for numerical electromagnetic field analyses of coated superconductors and its application to Roebel cables," *Supercond. Sci. Technol. 25 (2012) 119501 (1pp)*

[13] W. K. Chan, J. Schwartz, "A Hierarchical Three-Dimensional Multiscale Electro-MagnetoThermal Model of Quenching in REBa2Cu3O7 Coated-Conductor-Based Coils," *IEEE Trans. Appl. Supercond., vol. 22, no. 5, pp. 47060104706010, 2012.*

[14] W. K. Chan, P. J. Masson, C. Luongo, and J. Schwartz, "Threedimensional micrometer-scale modeling of quenching in high aspect ratio YBa2Cu3O7 coated conductor tapes. Part I: Model development and validation," *IEEE Trans. Appl. Supercond., vol. 20, no. 6, pp. 23702380, Dec. 2010.*

[15] G. Willering, "Stability of Superconducting Rutherford Cables: For Accelerator Magnets." *Ph.D. thesis, University of Twente, 2009.* Available: https://ris.utwente.nl/ws/portalfiles/portal/6083891

[16] J. van Nugteren, "High Temperature Superconducting Accelerator Magnets." *Ph.D. thesis, University of Twente, 2016.* Available: https://cds.cern.ch/record/2228249/files/CERN-THESIS-2016-142.pdf

[17] COMSOL Multiphysics Users Guide, COMSOL, Burlington, MA, USA, 2012.

[18] M. Casali, M. Breschi, and P. L. Ribani, "Two-dimensional anisotropic model of YBCO coated conductors," *IEEE Trans. Appl. Supercond., vol. 25, no. 1, Feb. 2015, Art. no. 6600112.*

[19] M. Breschi, M. Casali, L. Cavallucci, G. De Marzi, and G. Tomassetti, "Electro thermal analysis of a twisted stacked YBCO cable in conduit conductor," *IEEE Trans. Appl. Supercond., vol. 25, no. 3, Jun. 2015, Art. no. 4800505.*

[20] M Breschi, L Cavallucci, P. L. Ribani, A. V. Gavrilin, and H. W. Weijers, "Analysis of quench in the NHMFL REBCO prototype coils for the 32T magnet project," *Supercond. Sci. Technol., vol. 29, 2016, Art. no. 055002.*

[21] M Breschi, L Cavallucci, P. L. Ribani, A. V. Gavrilin, and H. W. Weijers, "Modeling of Quench in the Coupled HTS Insert/LTS Outsert Magnet System of the NHMFL," *IEEE Trans. Appl. Supercond., vol. 27, no. 5, Aug. 2017.*

[22] Q. Zhang, Y. Yang, E. Young, L. Cavalucci, A. Kario, W. Goldacker, A. Usoskin, and L. Bottura, "Performance and Quench Characteristics of a Pancake Coil Wound with 2G YBCO Roebel Cable," presented at EUCAS2017 (EUCAS2017-4LP4-11) accepted for publication on *IEEE Trans. Appl. Supercond., vol. , no. ,*

[23] A. Kario, "HTS Roebel cables for the EuCARD-2 'Future Magnets'," 3rd EuCARD-2 Annual Meeting, 2016. Available: https://indico.cern.ch//event//489475//contributions//1166833//attachments//1263291//1868932//23.04.2016_Malta_Kario.pdf.

Part II

Analysis of Losses in Superconducting Magnets

Chapter 6

Analysis of Losses for the Future Superconducting Gantry Configuration

6.1 Introduction

In both the analysis for the NHMFL prototypes and of the EUCARD2-Roebel cable, the slow time-varying magnetic field allows one to study the stability without accounting for the coupling and magnetization losses. In the second part of this study a different theme is presented, in the frame of the design of the first superconductive Gantry magnet for cancer therapy at the Paul Scherrer Institute (Switzerland), the electrothermal stability of the Gantry is analysed during its operation cycle. The magnetic flux density variation during the cycle to bend the beam particle causes coupling and hysteresis losses in the Gantry magnet system. The computed ac and coupling losses are introduced in a thermal model to study the temperature margin and the safety operation conditions of the Grantry magnet during its operating cycle. The same thermal model and homogenization procedure for the calculation of anisotropic equivalent material properties developed for the quench studies described in the previous chapters is hereby applied and furthermore validated. Before to describe the numerical techniques adopted in the study, a brief introduction about the Gantry magnet for cancer therapy and the common adopted methodologies for the ac and coupling losses estimation is presented.

The medical therapies based on ion or proton beams are widely developing for cancer treatment due to their capability to irradiate the tumor from different directions in order to reduce the dose on the normal cells. The radiation dose delivered to the target volume is maximized and the dose to the surrounding normal tissues is minimized [1]-[3]. Many facilities use rotatable gantry beamlines to direct the proton or ion beam to the patient

110

from different angle [4]. The proton or ion therapy facilities are composed of beamline magnets, beam diagnostic elements and the mechanical support structure. The gantry magnet system is the final section of these facilities; it rotates around the patient and allows irradiating the tumor from different directions. These systems can be extremely heavy and cumbersome: as an example, the gantry magnet system of the Heidelberg Carbon Ion Gantry facility weighs 600 tons [4], and the Proton Therapy Gantry 2 of PSI weighs 200 tons [5]. A remarkable step forward in the direction of designing more compact and lighter gantries could be achieved by means of superconducting magnets, in particular for the final bending section that has a large aperture. The high field intensities that can be achieved with superconducting magnets allow decreasing the bending radius and, therefore, the overall weight and footprint of the system, with consequent reduction of the total size and complexity of the mechanical structure. Moreover, superconducting magnets allow reaching higher magnetic field gradients, which allows increasing the momentum acceptance of the particle beam. This feature reduces the need to ramp the magnet, which allows covering a large momentum spread, and enables new treatment techniques [6]-[7]. Recently, superconducting magnets have been designed and built for the carbon ion gantry at the National Institute of Radiological Sciences (NIRS) in Chiba (Japan) and for a proton gantry developed by the US company Pro-Nova [8]-[10]. These first superconducting gantry systems are currently under commissioning [11]. An R&D project to reduce the size of rotating gantry systems is presently in progress at the Paul Scherrer Institute [1]-[2], Switzerland, with the aim of developing a superconducting magnet system wound with Nb_3Sn Rutherford cables. The use of coolant for the magnet mounted on a rotating gantry is extremely difficult, and therefore, a conduction cooling option has been selected for this project. As already mentioned, the magnetic field of the rotating gantry has to vary in time depending on the energy of the particle beam. These electrodynamic transients generate losses in the superconducting coils, both due to hysteresis and to coupling currents. Moreover, some particles escaping from the nominal trajectory (beam losses), may collide with the coils causing thermal inputs that can result in a poor thermal stability of the conduction cooled coils. Therefore, the determination of coupling and hysteresis ac losses in relation with the magnetic field cycle is essential to ensure the thermal stability of a gantry magnet [12].

The state of the art for superconducting gantry systems is based on NbTi magnets. The analysis of losses and stability on NbTi gantry magnets is relatively widely analyzed in literature. Experimental tests of thermal stability on NbTi gantry magnets are presented in [12], whereas theoretical analyses are described in [13] and [14]. Superconducting materials other than NbTi, such as Nb_3Sn and HTS have several advantages due to their increased current carrying capability and temperature margin, but have been usually ruled out due to cost and difficulties associated with magnet fabri-

cation (such as conductor heat treatments on the winding tapes). Detailed studies of available temperature margins have to be carried out to determine the capabilities of Nb_3Sn and HTS materials for their application in gantry systems [14]. A few studies have been presented to determine the advantages and overall thermal stability of HTS materials for gantry magnet systems [15]-[16]. Meanwhile, the temperature margin and ac losses for Nb_3Sn gantry magnets have not been thoroughly analyzed yet.

In this chapter, a detailed numerical analysis is presented for the determination of temperature increase related to coupling and hysteresis losses during the working scenario of the Nb_3Sn gantry magnet under development at the Paul Scherrer Institute [1]-[2]. The THELMA code developed at the University of Bologna, validated for the study of Cable in Conduit Conductors for the ITER project [17]-[18], is adapted here to the analysis of ac losses in the Nb_3Sn Rutherford cable configuration. The model of the Rutherford cable is based on a distributed parameter circuit approach, that was proved suitable for the analysis of long range coupling currents both with numerical [19], [20] and analytical studies [21] [23]. The main development of the model adopted in this chapter with respect to the models presented in [19]- [23] consists in the adoption of non-homogenous interstrand contact conductances along the cable length, which allow a proper description of the short range coupling currents and related losses. The computation of coupling losses is validated in simplified cases versus analytical formulae available in the literature. Then, the coupling and hysteresis losses during the gantry magnet system operating transport current cycle are computed with THELMA, and implemented in a thermal model developed in the COMSOL Multiphysics environment [24]. Finally, the computed temperature distribution of the coils is compared with the current sharing temperature to determine the temperature margin during the operating current cycle.

6.2   Gantry Magnet System Configuration

The magnetic flux density in accelerator magnets is usually represented through a series development, in which the various components are referred to as field harmonics [25].

$$B_y + jB_x = \sum_{n=1}^{\inf} (B_n + jA_n) \left(\frac{x + jy}{r_0} \right)^{n-1} \tag{6.1}$$

where r_0 is a reference radius, B_n is the normal 2n-pole component of the magnetic field and A_n is the skew 2n-pole component of the magnetic field. In a former study a configuration of superconducting gantry magnet system proposed by PSI was presented in [1]. Several modifications to improve the magnetic system were then implemented in the configuration presented
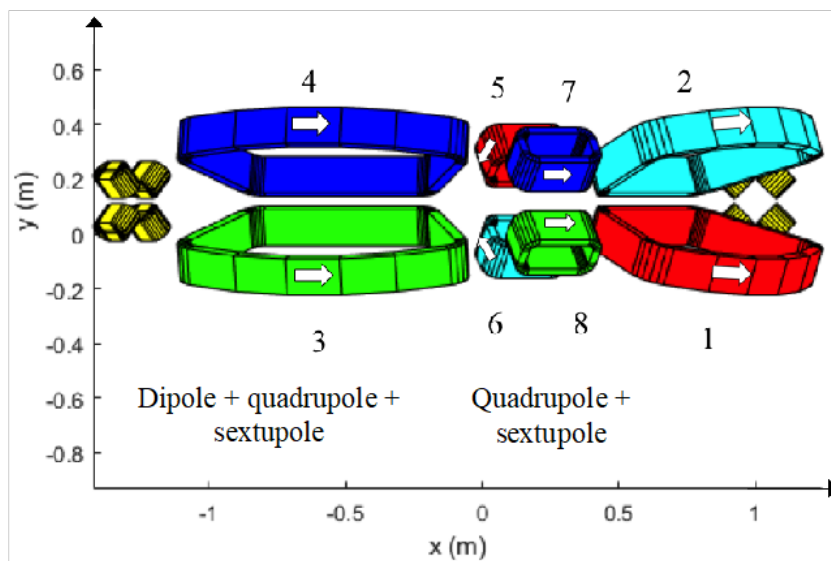
Figure 6.1: Layout of the gantry magnetic system as implemented in the THELMA code model. The split of the curvilinear part of each coil in 5 segments is only made for graphical representation purposes.

in [2], which is the one analysed in the present study. In this configuration, the dipolar field used to bend the protons to the patient location is produced by racetrack coils. The combined function magnet system configuration includes 8 main coils and two end quadrupoles, as shown in Fig. 6.1. The main dipole field component is provided by coils #1, #2, #3, #4. These coils also contribute with two other harmonics, namely a quadrupole and a sextupole field component. The coils #5, #6, #7, and #8, located in the middle of the magnet configuration, mainly contribute to the magnetic flux density with a quadrupole and a sextupole component. The end quadrupoles (with indices from #9 to #16) provide essentially a quadrupole component and consist of four copper racetrack coils. The magnetic geometry is such to produce a FODO structure (the term "FODO" describes a sequence of focusing, F, and defocusing, D, quadrupole magnets with dipole magnets or drift spaces denoted by "O") with the first quadrupole focusing in the bending plane. The superposition of dipole and quadrupole fields allows having locally achromatic bending sections without increasing the gantry size. For this reason it is important to use combined function magnets [6]. In optics rays of different wavelength find a different refraction index in a lens and therefore they experience a different focal length producing chromatic aberrations. In analogy to that, particles of different momentum see a different focusing strength in the quadrupoles. To correct the natural chromaticity produced by the focusing elements, a sextupole field component is added. In a sextupole a particle passing off-center receives a kick proportional to

Table 6.1:
MAIN GEOMETRIC DATA OF THE COILS

Coils N. 1,2,3,4

Cross section Width	40 mm
Cross section Height	140 mm
Number of layers (in the width direction)	27
Number of turns per layer (in the height direction)	28
Total number of turns	756
Cross section of cable with insulation in the coil	$7.41\,\text{mm}^2$
Length of the coil axis	2.65 m

Coils N. 5,6,7,8

Cross section Width	31 mm
Cross section Height	150 mm
Number of layers (in the width direction)	21
Number of turns per layer (in the height direction)	30
Total number of turns	630
Cross section of cable with insulation in the coil	$7.38\,\text{mm}^2$
Length of the coil axis	0.794 m

Coils N. 5,6,7,8

Cross section Width	40 mm
Cross section Height	100 mm
Length of the coil axis	0.215 m

the square of its displacement from the center. A sextupole acts then as a quadrupole with a focusing strength proportional to the displacement from the center.

The main geometric data concerning the magnet system design are reported in Table 6.1. In the present configuration, the same Nb$_3$Sn Rutherford cable structure is adopted for winding all the coils (#1 #8). The cable is not keystoned and composed of 12 Nb$_3$Sn strands. The main data of the Rutherford cable are reported in Table 6.2, whereas the main data concerning the superconducting wire are reported in Table 6.3. The parameterization of the critical surface of the wire adopting the ITER like parameterization is reported in [26].

The reference working scenario of the gantry magnet system is characterized by a series of transport current ramps and plateaus as shown in Fig. 6.2. The transport currents in the coils from #1 to #4 are identical, since they are connected in series; the same holds for the transport currents in the coils from #5 to #8. All transport currents exhibit an initial ramp

Table 6.2:
MAIN DATA OF THE RUTHERFORD CABLE

Type of cable	Rutherford
Twist Pitch	70 mm
Number of strands	12
Strand diameter	0.82 mm
lay angle	8.0°
Keystone angle	0°
Cu/nonCU	0.93
RRR	100
Width	4.9 mm
Thickness	1.45 mm
Critical current (4.2 K, 8 T, -22%)	363 A

Table 6.3:
MAIN DATA OF THE COMPOSITE SUPERCONDUCTING WIRE

Material	Area	% fraction
Cu	$3.05 \times 10^{-6} \, \text{m}^2$	41.2
Nb_3Sn	$1.64 \times 10^{-6} \, \text{m}^2$	22.2
Epoxy	$1.07 \times 10^{-6} \, \text{m}^2$	14.5
Bronze	$1.64 \times 10^{-6} \, \text{m}^2$	22.2

to their maximal value, followed by several cycles between this maximum and an intermediate current level set to 2/3 of the maximal current level. The transport current scenario is based on a worst case treatment scenario where four fields are applied each having a large depth extension requiring three magnets ramps per layer.

6.3 Model Description and Loss Computation Methodologies

6.3.1 Model Description

The electromagnetic model of the Rutherford cable in THELMA code [17]-[18] is based on a distributed parameter circuit approach. The equations of the model are derived from the Magneto-Quasi-Static formulation of the Maxwell equations. In order to discretize the Rutherford cable geometry, a single strand is a cable element (CE) of the model and the number of cable elements (NCE) of the model coincide with the number of strands. The
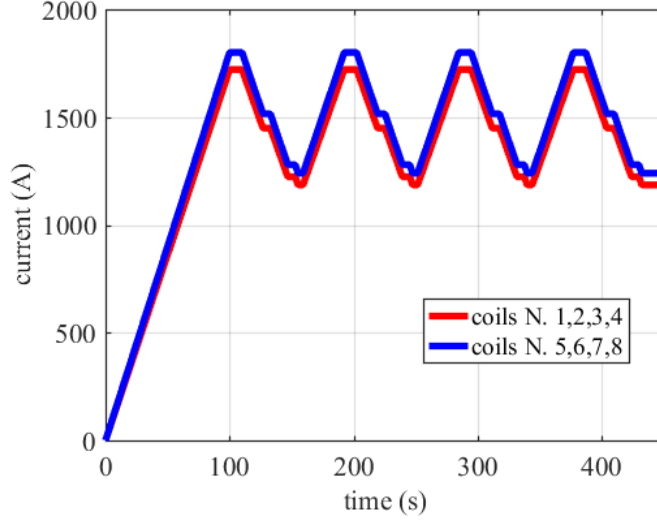
Figure 6.2: Evolution in time of the transport currents of the 8 main coils of the PSI gantry magnet system during a typical operating cycle.

unknowns of the problem are the values of the difference currents (i_α with $\alpha = 1, \cdots, NCE$) of the cable elements with respect to a uniform current distribution.

$$i_\alpha = I_\alpha - \frac{I}{NCE} \qquad \text{where } \alpha = 1, ..., \text{NCE} \qquad (6.2)$$

where I_α is the current in the α-th cable element and I is the total current of the cable. The scalar electrical potential and the magnetic vector potential are solved. The current density continuity condition is added to compute the current density in each CE.

$$\mathbf{E}(\mathbf{P}, t) = -\nabla V - \frac{\partial}{\partial t} \left[\frac{\mu_0}{4\pi} \int_\Omega \frac{\mathbf{J}(\mathbf{Q}, t)}{\mid \mathbf{P} - \mathbf{Q} \mid} d^3 \mathbf{Q} \right] \qquad (6.3)$$

$$\nabla \cdot \mathbf{J} = 0 \qquad (6.4)$$

The closure of equations is obtained by the power law as a constitutive law of the superconducting material. The other materials that compose the strand are supposed in parallel with the superconducting one.

The self and mutual per unit length induction coefficients are numerically calculated from geometrical parameters of the cable (twist pitches, cable-axes trajectory, strand diameter etc etc). From the geometrical parameters is also computed the per-unit-length conductance between CEs as a function of the longitudinal coordinate.

116

6.3.2 Hysteresis Losses

The electrodynamic losses are generated mainly during the current ramps and are due to both the hysteresis and coupling losses. The equations of the electrodynamic model implemented in the THELMA code [17]- [18] allow one to compute the current distribution between the strands and the corresponding coupling losses. The current sharing between strands occurs through either a uniform or a variable contact conductance per unit length. In both cases, the per unit length conductances are computed in order to obtain given values of the adjacent (Ra) and crossover (Rc) resistances [27] respectively set to $50\,\mu\Omega$ and $100\,\mu\Omega$.

The determination of the hysteresis losses starts from the calculation of the effective diameter (d_{eff}) of the strand. In the present analysis, the Nb$_3$Sn strand selected for the magnet system design owes to the pool of the ITER strands. The d_{eff} is computed from the magnetization cycle obtained experimentally, and is equal to $7.8\,\mu\mathrm{m}$ for this wire.

The local value of the power dissipated per unit volume due to the hysteresis losses is then given by the following expression [28]

$$P\left[\frac{W}{m^3}\right] = \frac{2}{3\pi}\mu_0 J_c\left(B, T, \epsilon\right)\lambda\, d_{deff}\mid\frac{dB}{dt}\mid \tag{6.5}$$

where J_c is the critical current density as a function of the temperature T, magnetic flux density B and strain ϵ; λ is the superconductor fraction; d_{eff} is the effective diameter of the strand and $\mid dB/dt\mid$ is the time derivative of the magnetic flux density.

This formula requires the knowledge of the field distribution at every coil location: from this input both the local value of the critical current density and of the time derivative of the magnetic flux density can be computed.

6.3.3 Coupling Losses

The validation of the THELMA model [17]- [18] for the calculation of the coupling losses was carried out in a simplified test case, by comparison with two analytical formulae available in the literature [29]- [30]. The selected case study consists of a rectilinear Rutherford cable composed by 14 strands, without transport current, subjected to a uniform magnetic field applied orthogonally to the broad face of the cable. The time dependence of the magnetic field follows a triangular wave from 0 to $3\,\mathrm{T}$, with a variable ramp rate.

The comparison between the analytical and the numerical THELMA results are performed with two different models. In a first approximate model the per unit length conductance is assumed uniform along the cable length; the value selected is equivalent to the overall resistance between the two strands over one cable twist pitch given by the local contact resistances
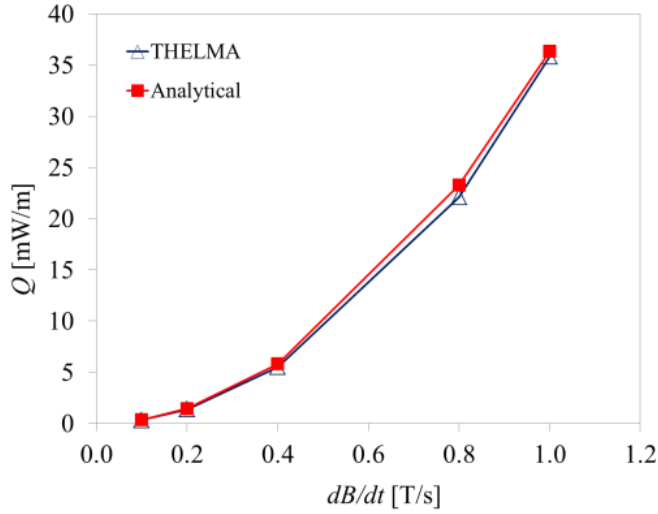
Figure 6.3: Power per unit length dissipated in the Rutherford cable subjected to a uniform magnetic field applied perpendicular to the cable wide face: numerical vs analytical results.

between two strands. A second approach is based on the definition of a variable contact conductance between the strands. The variable conductance is calculated from the geometrical model assuming a given value of the per unit surface conductance, which is implemented as a fitting parameter.

A convergence study was performed by changing the number of mesh elements per twist pitch in the numerical simulations. The comparison between the numerical and analytical results is presented in Table 6.4. The results clearly indicate that the model based on a uniform contact conductance per unit length, which is suitable for the calculation of long range coupling currents [19], is not suited for the analysis of short range coupling currents, as it underestimates the losses due to coupling currents. The results show that the model with non-uniform contact conductances between strands is suitable to compute the losses due to coupling currents; the number of mesh elements in a twist pitch does not significantly affect the results. In the case of 14 mesh elements per twist pitch, only one mesh point is included in every cross-over contact between non-adjacent strands. In the 28 and 42 mesh element cases, each contact is discretized with two and three mesh point respectively. The convergence study shows that using 28 elements along one cable twist pitch is sufficient for a correct computation of the coupling losses without excessively increasing the computational efforts. This level of mesh refinement was therefore selected for the following analyses. In order to compare analytical and numerical results over a broader range of model parameters, the power loss was computed with variable ramp-rates of the magnetic flux density applied perpendicular to the broad face of the cable. Fig. 6.3 shows the quadratic dependence of the losses on the ramp rate, and

118

Table 6.4:
THELMA MODEL RESULTS WITH $\dot{B} = 1$ T/S

Number of elements in a twist pitch	Q(mW/m) constant conductance	Q(mW/m) variable conductance	Q(mW/m) Sytnikov [29]	Q(mW/m) Akhmetov [30]
magnetic flux density field perpendicular to the large surface of the cable				
14	21.45	35.07		
28	21.31	34.55	36.38	35.86
42	21.30	35.86		

Table 6.5:
THELMA VERSUS ANALYTICAL RESULTS.

$\dot{B}$(T/s)	Q(mW/m) variable conductance	Q(mW/m) Sytnikov
0.1	0.35	0.36
0.2	1.38	1.46
0.4	5.53	5.82
0.8	22.11	23.28
1.0	35.87	36.38

a good agreement of numerical and analytical results over the whole range of this parameter is obtained (see Table, which therefore gives confidence in the modeling approach adopted.

6.4 Computation of Total Losses in the Gantry Magnet System

6.4.1 Computation of Total Losses at Selected Turns of the Gantry Magnets

The power losses during the electrodynamic transients of the gantry system were computed selecting for each coil a given number of reference turns. In particular, six representative turns for each coil were modeled at the strand level by the THELMA code. The locations of these turns, numbered from #1 to #6, are shown in Fig. 6.4. The indication of the trajectory of the Rutherford cable along turn #1 of coil #1 is shown in Fig. 6.4a.

The geometry of the reference turns is reproduced for all the main coils of the gantry magnet system. The total power losses, including hysteresis and coupling losses, are computed by the THELMA code at the representative
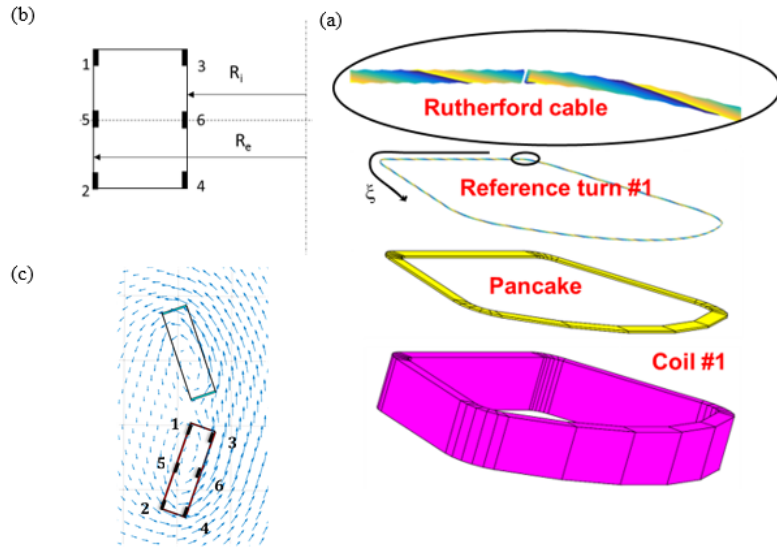
Figure 6.4: (a) Components of coil #1 used, with indication of the trajectory of the Rutherford cable along turn #1 of coil #1. (b) Position of the representative turns of a coil (figure not in scale) (c) Magnetic flux density lines at the positions of coils #1 and #2 in 2D plot of the coil cross section in the middle plane orthogonal to the z axis.

turns during the typical operating current cycle (see Fig. 6.1). As a first step, in order to understand the symmetries of the magnet system, only turns #1, #2, #3 and #4 are considered in the analysis. The total power, integrated over the whole length of each turn, is divided by the total volume of the turn, including both the cable and the epoxy resin insulation located around each turn, in order to obtain the losses per unit volume. The total losses per unit volume computed for the coils #1, #2, #3, and #4 are reported in Fig. 6.5. It is worth noting that the power evolution follows the operation current profile, with null power losses during the plateau, and a cyclic behaviour during the transport current cycles mentioned above. It can be noticed that the computed power loss curves for the coils #1 and #3 are identical; this identity is confirmed for all the representative turns at every location of the coil. The same comment applies for the losses in coils #2 and #4. These identities are related to the symmetry of the gantry magnet system in the present configuration. Moreover the losses in coil #1 and coil #2 are identical once the representative turn #2 is exchanged with turn #4 and turn #1 is exchanged with turn #3. The same consideration holds for the losses in coil #3 and coil #4. These identities derive from simple symmetry considerations about the configuration of the gantry magnet system and of the representative turns geometry shown in Fig. 6.4. These arguments lead to the conclusion that all coils #1 through #4 will be characterized by the same temperature distribution at the end of the transport current cycle in
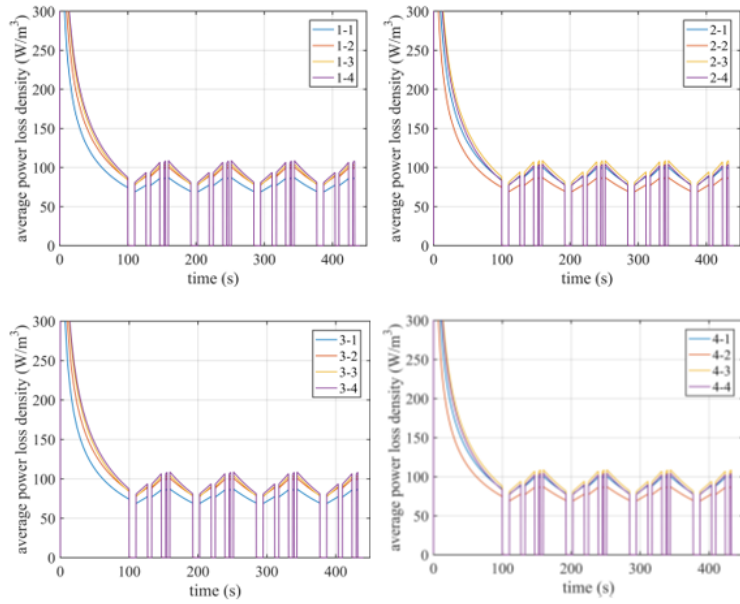
120

Figure 6.5: Average power loss per unit volume for the 4 representative turns of respectively coil #1, coil #2, coil #3, coil #4 computed with uniform current boundary conditions.

adiabatic conditions. Thus, only one coil out of the first 4 of the gantry magnet system is analyzed for the detailed calculations of the temperature distribution. The selected representative coil for these computations is coil #1.

Similar considerations hold for the coils #5, #6, #7, and #8. Therefore, the expected temperature distribution after the transport current cycle in these 4 coils is practically the same. Thus, only one coil is selected for the temperature distribution computation at representative, namely coil #5.

Once identified the two coils #1 and #5 of interest for the present analysis, a more detailed description of these two is then performed computing the losses in the two additional turns #5 and #6 shown in Fig. 6.4b. The losses at all the 6 representative turns of the coils #1 and #5 are presented in Fig. 6.6.

6.4.2 Impact of Boundary Conditions on Current Distribution and Power Losses

Several types of boundary conditions can be applied to the calculation of current distribution in the frame of distributed parameter circuit models. The first type of boundary condition supposes that the transport current is uniformly distributed between strands at the cable ends. The second type of boundary condition assumes that the strands are connected through an
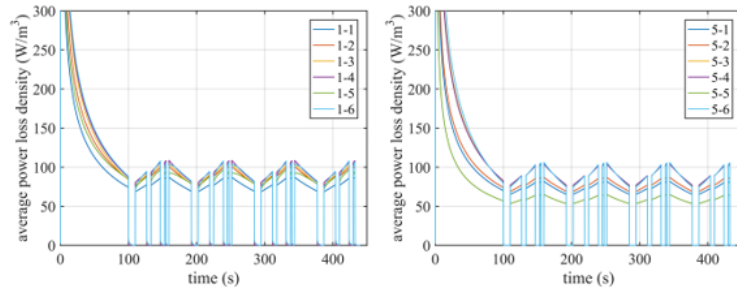
Figure 6.6: Average power loss per unit volume for the 6 representative turns of coil #1 and coil #5, computed with uniform current boundary conditions.

equipotential surface at the cable ends. The real operating conditions, represented by a continuous flow of currents from one turn to the next one, are included between these two extreme cases. The impact of these two different boundary conditions on the total power losses along one representative turn are shown in Fig. 6.7 for coil #1 (turn #4) and coil #5 (turn #3) respectively. It is worth noting that no essential modification of the
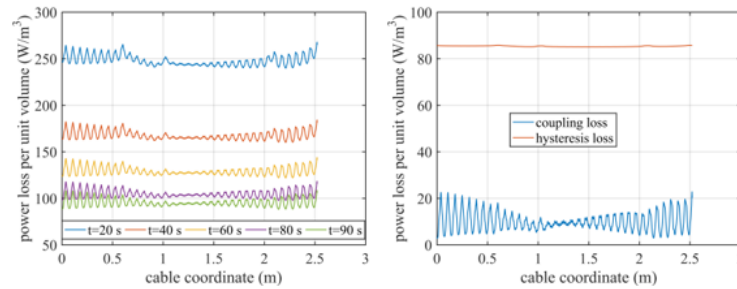

Figure 6.7: Average power loss per unit volume for turn #4 of coil #1 and turn #5 of coil #3 with uniform current boundary conditions and short circuit boundary conditions.

total power loss in the two coils is observed when changing the boundary conditions. This result is mainly related to the predominant effect of the hysteresis losses on the total losses in each strand. The boundary condition affects the current redistribution between the different strands of the cable. Therefore, the effect of boundary condition is predominant on the coupling losses. The hysteresis losses are mainly dominated by the value of the total magnetic field, whereas the influence of the current redistribution and of the boundary conditions on the hysteresis losses is negligible. The described behaviour, with reference to turn #4 of coil #1, is shown in Fig. 6.8 for short circuit boundary conditions and in Fig. 6.9 for uniform current boundary conditions. The difference in coupling losses obtained with the two studied types of boundary conditions does not affect the results on the total losses. The total AC and coupling losses are not affected by the two

type of boundary conditions. Since the uniform current distribution boundary condition reduces the degrees of freedom of the model and is usually adopted in literature [22], it is also implemented in the present work. The same considerations can be deduced analysing the results obtained for coil #5.
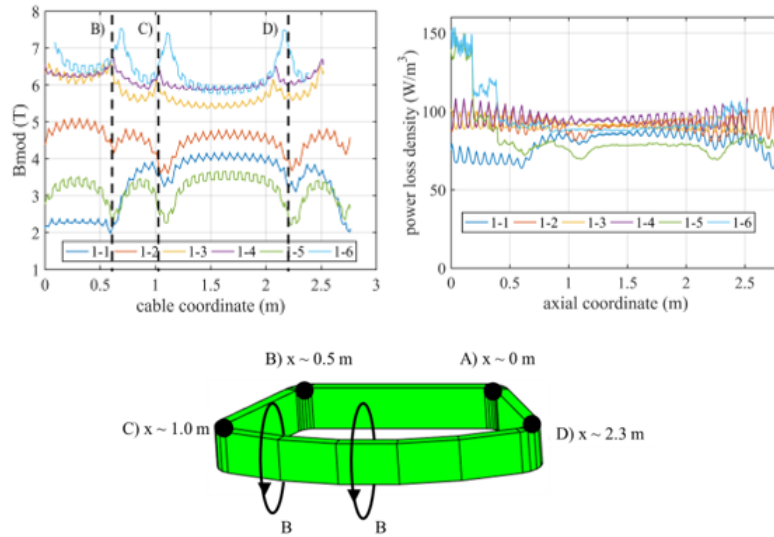

Figure 6.8: (a) Modulus of the magnetic flux density field on strand #1 of the coil #1 at t = 100 s. (b) Average power loss (hysteresis + coupling) along the reference turns of coil #1 at t = 90 s. (c) Sketch of the different locations along the turns of coil #1.

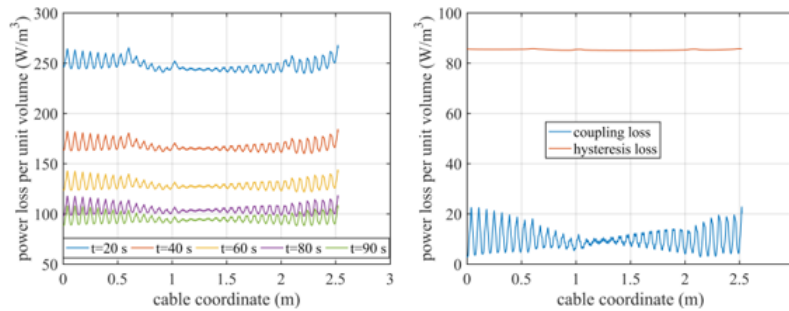Figure 6.9: Simulations with uniform current boundary conditions: (a) total power loss along the length (cable coordinate) of turn #4 of coil #1 at t = 20 s t = 40 s, t = 60 s, t = 80 s, t = 90 s and (b) coupling and hysteresis losses at t = 90 s.

6.4.3   Results

The flux lines of the magnetic flux density at the locations of coils #1 and #2 are shown in Fig. 6.4c. The modulus of the magnetic flux density is

greater at the turns #3, #4 and #6 than at the locations of turns #1, #2 and #5.

In order to understand the dependence of the current distribution on the magnetic flux density inside the coil, the longitudinal variation of the magnetic flux density along selected strands is analysed here. Fig. 6.7 shows the modulus of the magnetic flux density field along the cable coordinate for the 6 reference turns of coil #1. The magnetic flux density is highest at the turn #6, since it is located close to the magnet bore. The magnetic field exhibits a periodicity with period equal to the twist pitch of the cable, due to the zig-zag path of each strand along the cable length. The magnetic flux density is higher at the internal turns (#1, # 2 and #5) then at the external turns (#3, #4 and #6). Therefore, the magnetic flux density differently affects the different turns and the different points A, B, C, D (see Fig. 6.8c) along the turns. The different power loss regions are related to the impact of the magnetic flux density at the various coil locations. The power loss density along the turns of coil #1 at t = 90 s is shown in Fig. 6.7b. It can be noticed that the power loss density along the reference turns is more homogeneous than the magnetic flux density at the turns themselves. The result is due to dominant contribution of the hysteresis losses on the total losses. Moreover, the hysteresis losses depend on the product of the critical current density, which decreases with the magnetic flux density, and the time derivative of the magnetic flux density, which is greater at the high field locations. The total power losses per unit volume along the length of turns #1 and #3 of coil #1 are shown in Fig. 6.8. The power losses closely follow the distribution of the magnetic flux density along the length of the turn. Moreover, the power losses decrease in time during the initial transport current ramp up. As mentioned above, the hysteresis losses are dominant and depend linearly on the critical current of the wires, which decreases with increasing the magnetic flux density during the current ramp. Therefore, the initial parts of the ramp are quite delicate in terms of input power from the electrodynamic losses in these coils.

6.5   Thermal Model of the Gantry Magnet System

6.5.1   Calculation of Temperature Distributions for Coil #1 and Coil #5

The thermal model of the magnet system solves the heat balance equation in a 3D reference system where the homogenized cable properties are considered.

$$\rho_{Hom} C_{p_{Hom}} \frac{\partial T}{\partial t} + \nabla \cdot (-\mathbf{K}_{Hom} \cdot \nabla T) = Q_{tot} \tag{6.6}$$

where the homogenized cable properties are considered. The parameter ρ_{Hom} [kg/m^3] is the homogenized density, $C_{p_{Hom}}$ [J/kgK] is the homoge-

nized specific heat and $\mathbf{K}_{Hom}$ [W/mK] the tensor of homogenized anisotropic thermal conductivity .

The materials considered in the present analysis are: copper, superconductor and bronze in the composite wire cross section, and epoxy resin in the winding pack. Their respective cross section areas are reported in Table 6.3.

Both the specific heat and the longitudinal thermal conductivity have been homogenized accounting for the cross section areas of the coil constituting materials. The thermal conductivity in the transverse direction, instead, has been taken equal to the thermal conductivity of the epoxy resin, which represents the main thermal resistance to the flux flow in transverse direction. The validation of the homogenization procedure and the comparison with smaller volume with all the individual material components is carried on in [31]. The approach was further applied and compared with experimental results for large scale devices in [33]- [34].

As anticipated in the previous sections, the incoming power density from the electrodynamic losses is calculated with the THELMA code at the selected reference turns 1, 2, 3, 4, 5 and 6 of the coils #1 and #5. The calculation of the temperature rise due to these losses is performed for these two coils only, given the aforementioned symmetry conditions. Of course, the heat source obtained with THELMA has a time-dependent profile related to the magnetic flux density ramp rate. The heat source at the vertex points is interpolated in the mesh of the COMSOL model by spreadsheet tables. A further interpolation in time is required to account for the time dependence of the total losses computed by THELMA at different time instants. As mentioned above, in the parametrization of the critical surface of the strand, the critical current depends on the magnetic flux density, and it diverges for very low values of this field. Therefore the losses diverge if the magnetic flux density gets close to zero. The influence of losses on the temperature increase is controlled by setting their maximal value to $300\,\mathrm{W/m}^3$. The introduced maximum value is obtained for a magnetic flux density of around $0.5\,\mathrm{T}$. Computations performed without limits on the ac losses maximum value show no substantial changes in the final temperature of the coils #1 and #5.

The temperature distributions obtained from the COMSOL computation at t = 20 s during the initial current ramp- up and at t = 440 s, almost at the end of the transport current cycle, are reported respectively in Fig. 6.10. It is worth noting that a very uniform temperature distribution is obtained both during the current ramp and at the end of the operating current cycle over the whole volume of the coil transverse cross section. This result is quite important, as it shows that the formation of hot spots is not expected in these working conditions. The same result is shown for the coil #5 in Fig. 6.11 at t = 20 s and t = 440 s. Also the coil #5 exhibits the same thermal behaviour: the temperature distributions are very uniform and the formation of hot spots due to the losses in electrodynamic transients is not
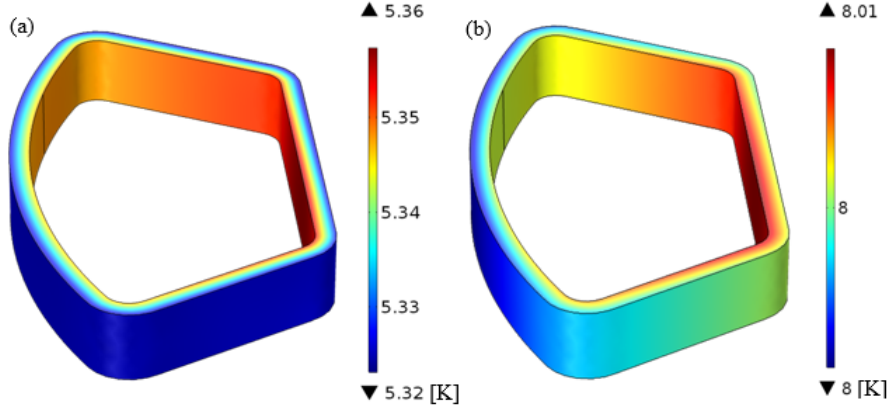
expected.

Figure 6.10: Temperature profile over the volume of coil #1 at (a) t = 20 s during the initial current ramp-up and (b) after the whole operating current cycle (t = 440 s)
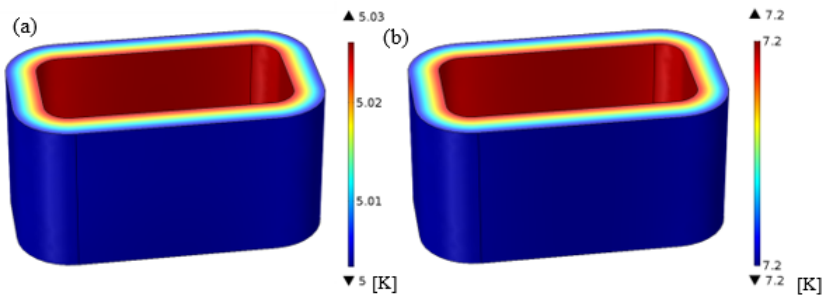

Figure 6.11: Temperature profile over the volume of coil #5 at (a) t = 20 s during the initial current ramp-up and (b) at t = 440 s after the whole operating current cycle

6.5.2 Computed Temperature Distribution *vs* Current Sharing Temperature

In order to compare the increase of the coils temperature during their operating current cycle with the allowable temperature limits of the magnet, the current sharing temperature (T_{cs}) of the coil is computed at the peak field locations of both coil #1 and #5. Since the temperature distribution resulting from the power losses is very uniform for both coils, the temperature margin of the coil can be assessed by only considering the margin available at the location of peak field. The current sharing temperature is defined here as the temperature at which the electric field reaches its critical value conventionally set to 10×10^{-5} V/m. Since the current sharing temperature is a function of the applied magnetic flux density, its value varies in time during the operating current cycle.

The time evolution of the current sharing temperature (T_{cs}) at the peak magnetic flux density location of coil #1 is reported in Fig. 6.12. It is worth noting that the maximal temperature reached in coil #1, 8 K, is below the lowest limit of 9.7 K set by current sharing temperature at the peak field location. The temperature margin for this coil is therefore 1.7 K, which is sufficient for a safe magnet design. The same considerations are deduced for the coil #5. The T_{cs} at the peak magnetic flux density location is reported in Fig. 6.13. Also in this case, the maximal temperature reached in the coil (7.2 K) is below the lowest limit of 9.3 K set by the current sharing temperature. A temperature margin of about 2.1 K is sufficient for a safe operation of the coil.

In these design considerations, it should be reminded that the temperature distribution of the coils is computed assuming adiabatic boundary conditions, which therefore give a conservative approach.

Figure 6.12: Profile of the current sharing temperature (T_{cs}), blue curve, primary axis on the left) and magnetic flux density at the peak field location of coil #1 (B, red curve, secondary axis)
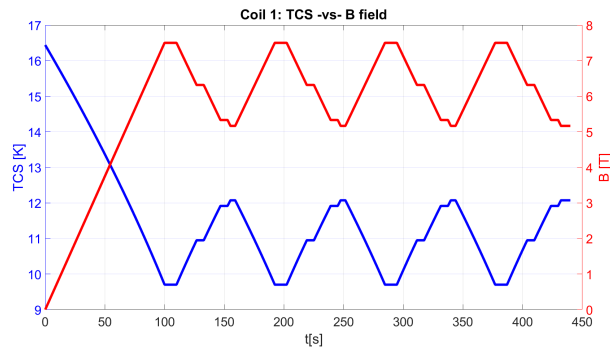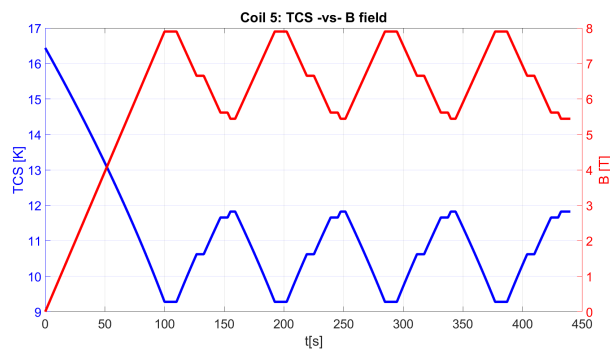

Figure 6.13: Profile of the current sharing temperature (T_{cs}), blue curve, primary axis on the left) and magnetic flux density at the peak field location of coil #5 (B, red curve, secondary axis)

Conclusion

The analysis reported in this paper is aimed at determining the losses in a superconducting Gantry magnet system for proton treatment in the frame of tumour therapy.

The THELMA model, previously developed for the analysis of Cable in Conduit Conductor, was adapted to analyse ac losses in the Rutherford cable configuration, and validated by comparison to analytical formulae in simplified test cases. The code was validated for the calculation of losses in Rutherford cables by comparing analytical and numerical results in simplified cases available in the literature. The comparison shows that a good agreement can be achieved with a number of elements per cable twist pitch equal to the double of the number of strands. A variable contact conductance between strands along the cable length is essential to achieve a good agreement with the analytical calculations.

The THELMA model was then applied to the analysis of the gantry magnet system, by determining both hysteresis and coupling losses. The hysteresis losses are mainly influenced by the variation of the total magnetic field, by the critical current density and by the effective diameter of the superconducting wires. It was found that in the considered design the hysteresis losses are predominant with respect to the coupling losses. The interstrand coupling losses were computed by selecting a number of representative turns in the winding pack cross section. The THELMA code allows one to account for the magnetic field generated by all coils in the magnet system, and by all turns except for the selected one, under the assumption that the current is uniformly distributed between strands. The analysis show that the interstrand coupling losses are affected by the selection of the boundary conditions at the ends of the representative turn. The real current distribution should be included between the two extreme conditions represented by the two boundary conditions of uniform current distribution at the cable ends and of equipotential surface at the cable ends. The total losses however, are only marginally affected by the selection of the boundary conditions of the coupling loss calculation.

Due to the influence of the magnetic field on the hysteresis losses, the total losses depend on the distribution of the magnetic flux density along the length of the representative turn. On one hand, the hysteresis losses increase with the critical current of the wire, which decreases with increasing the magnetic field. On the other hand, the hysteresis losses depend on the time derivative of the magnetic flux density, which is greater at the high field locations. Although the locations of peak field generally exhibit higher losses than the rest of the winding pack, there is some compensation effect, so that the loss distribution versus location is smoother than the field distribution. As far as the time distribution of the losses, during the initial ramp of the transport current cycle, when the critical current density is high due to the

low values of magnetic field, a significant input power enters the magnet system due to the electrodynamic losses.

The computed losses were implemented in an adiabatic thermal model to perform a conservative estimation on the thermal stability of the magnet system design during the operation current cycle. The computed temperature profile was compared with the time dependent current sharing temperature, obtaining as a result a sufficiently large temperature margin, that guarantees a safe magnet design.

Bibliography

[1] C. Calzolaio, S. Sanfilippo, M. Calvi, A. Gerbershagen, M. Negrazus, M. Schippers, M. Seidel, "Preliminary Magnetic Design of a Superconducting Dipole for Future Compact Scanning Gantries for Proton Therapy," *Cryogenics* 40 (2000), 445-457.

[2] S. Sanfilippo, C.Calzolaio, A.Anghel, A. Gerbershagen and J.M.Schippers, "Conceptual design of superconducting combinedfunction magnets for the next generation of beam cancer therapy gantry," Proceedings of RuPAC2016, St. Petersburg, Russia

[3] N. Amemiya, Y. Sogabe1, M. Sakashita1, Y. Iwata, K. Noda, T. Ogitsu, Y. Ishii and T. Kurusu, "Magnetisation and field quality of a cosine-theta dipole magnet wound with coated conductors for rotating gantry for hadron cancer therapy," *Supercond. Sci. Technol.* 29 (2016) 024006 (14pp)

[4] C. Muehle, B. Langenbeck, A. Kalimov, F. Klos, G. Moritz, and B. Schlitt, "Magnets for the Heavy-Ion Cancer Therapy Accelerator Facility (HICAT) for the Clinic in Heidelberg," *IEEE Trans. Appl. Supercond., vol. 14, no. 2, June 2004.*

[5] E. Pedroni *et al.* "The PSI Gantry 2: a second generation proton scanning gantry," *Z. Med. Phys. 14 (2004) 2534v.*

[6] A. Gerbershagen, D. Meer, J. M. Schippers, M. Seidel, "A novel beam optics concept in a particle therapy gantry utilizing the advantages of superconducting magnets," *Zeitschrift fr Medizinische Physik, Volume 26, Issue 3, September 2016, p. 224237.*

[7] K. Noda, T. Furukawa, T. Fujimoto, T. Inaniwa, Y. Iwata, T. Kanai, M. Kanazawa, S. Minohara, T. Miyoshi, T. Murakami, Y. Sano, S. Sato, E. Takada, Y. Takei, K. Torikai, M. Torikoshi, "New treatment facility for heavy-ion cancer therapy at HIMAC," *Nuclear Instruments and Methods in Physics Research B 266 (2008) 21822185.*

[8] Y. Iwata, K. Noda, T. Shirai, T. Murakami, and T. Furukawa, "Design of a superconducting rotating gantry for heavy-ion therapy," *Phys. Rev.Special Topics, Accel. Beams, vol. 15, no. 4, 2012, Art. no. 044701.*

[9] Y. Iwata, K. Noda, T. Shirai, T. Furukawa, and T. Murakami, "Development of curved combined-function superconducting magnets for a heavy ion rotating-gantry," *IEEE Trans. Appl. Supercond., vol. 23, no. 3, June 2014.*

[10] V. Derenchuk, "The ProNova SC360 Gantry," *Modern Hadron Therapy Gantry Developments, Cockcroft Inst., Daresbury, U.K., Tech. Rep., Jan. 2014.*

[11] Y. Iwata *et al.*, "Beam commissioning of a superconducting rotating-gantry for carbon-ion radiotherapy," *Nuclear Instruments and Methods in Physics Research A, vol. 834, pp. 7180, 2016.*

[12] Y. Iwata, K. Noda , T. Murakami, T. Shirai, T. Furukawa, T. Fujita, S. Mori, K. Mizushima, K. Shouda, T. Fujimoto, T. Ogitsu, T. Obana, N. Amemiya, T. Orikasa, S. Takami, S. Takayama, "Development of a superconducting rotating-gantry for heavy-ion therapy," *Nuclear Instruments and Methods in Physics Research B, vol. 317 (2013), pp. 793797.*

[13] C. Priano, P. Fabbricatore, S. Farinon, R. Musenich, M. Perrella, and S. Squarcia, "A Superconducting Magnet for a Beam Delivery System for Carbon Ion Cancer Therapy," *IIEEE Trans. Appl. Supercond., vol. 12, no. 1, March 2002.*

[14] L. Brouwer, S. Caspi, R. Hafalia, A. Hodgkinson, S. Prestemon, D. Robin, and W. Wan, "Design of an Achromatic Superconducting Magnet for a Proton Therapy Gantry," *IEEE Trans. Appl. Supercond., vol. 27, no. 4, March 2017.*

[15] S. Takayama, K. Koyanagi, T. Tosaka, K. Tasaki, T. Kurusu, Y. Ishii, N. Amemiya, K. Suzuki, T. Ogitsu, Y. Iwata, and K. Noda, "Thermal Stability of Conduction-Cooled HTS Magnets for Rotating Gantry," *EEE Trans. Appl. Supercond., vol. 26, no. 4, June 2016.*

[16] S. Takayama, K. Koyanagi, A. Yamaguchi, K. Tasaki, T. Kurusu, Y. Ishii, N. Amemiya, T. Ogitsu and K. Noda, "Design of conduction-cooled HTS coils for a rotating gantry," *Phys. Procedia 67 87984.*

[17] M. Breschi, P.L. Ribani, "Electromagnetic Modeling of the Jacket in Cable-in-Conduit Conductors," *IEEE Trans. Appl. Supercond., vol. 18, no.1, March 2008.*

[18] M. Breschi, M. Bianchi, R. Bonifetto, S. Carli, A. Devred, N. Martovetsky, P. L. Ribani, L. Savoldi, I. Takaaki, and R. Zanino, "Analysis of AC Losses in the ITER Central Solenoid Insert Coil," *IEEE Trans. Appl. Supercond.,, vol. 27, no. 4, June 2017.*

[19] A. Akhmetov, L. Bottura, M. Breschi, P. L. Ribani, "A theoretical investigation on current imbalance in flat two-layer superconducting cables," *Cryogenics, Vol. 40, n. 9-10, pp. 627 635, 2000.*

[20] A. Akhmetov, L. Bottura, M. Breschi, "A Continuum Model for Current Distribution in Rutherford Cables," *IEEE Trans. Appl. Supercond., vol. 11, no. 1, March 2001.*

[21] L. Bottura, M. Breschi, M. Fabbri, "Analytical solution for the current distribution in multistrand superconducting cables," *Journal of Applied Physics, Vol. 92, n. 12, pp. 7571 7580, 2002.*

[22] L. Bottura, M. Breschi, M. Fabbri, "Analytical Calculation of Current Distribution in Multistrand Superconducting Cables," *IEEE Trans. Appl. Supercond., vol. 13, no. 2, June 2003.*

[23] L. Bottura, M. Breschi, M. Fabbri, "An analytical benchmark for the calculation of current distribution in superconducting cables," *Cryogenics, Vol. 43, n. 3-5, pp. 241 248, 2003.*

[24] COMSOL Multiphysics Users Guide, COMSOL, Burlington, MA, USA, 2012.

[25] P. Schmuser, "Course on Acelerator Optics," *Proceedins of the 986 CERN Accelerator School, CERN 87-10, 1987.*

[26] L. Bottura, B. Bordini, "Jc(B,T,) parametrization for the ITER Nb3Sn Production," *IEEE Trans. Appl. Supercond., vol. 9, no. 3, June 2009.*

[27] A.P. Verweij. "CUDI: A model for calculation of electrodynamic and thermal behaviour of superconducting Rutherford cables", *Cryogenics 46 (2006) 619626*.

[28] M. N. Wilson, Superconducting Magnets. Oxford, U.K.: Oxford Univ. Press, 1983

[29] V.E. Sytnikov, G.C. Svalov, S.G. Akopov, I.B. Peshkov, "Coupling losses in superconducting transposed conductors located in changing magnetic fields," *Cryogenics 29 (1989), 926-930*.

[30] A.A. Akhmetov, "Compatibility of two basic models describing the a.c. loss and eddy currents in flat superconducting cables," *Cryogenics, 40 (2000), 445-457*.

[31] M. Casali, M. Breschi, and P. L. Ribani, "Two-dimensional anisotropic model of YBCO coated conductors," *IEEE Trans. Appl. Supercond., vol. 25, no. 1, February 2015*.

[32] M Breschi, L Cavallucci, P. L. Ribani, A. V. Gavrilin, and H. W. Weijers, "Analysis of quench in the NHMFL REBCO prototype coils for the 32T magnet project," *Supercond. Sci. Technol., vol. 29, 2016, Art. no. 055002*.

[33] M Breschi, L Cavallucci, P. L. Ribani, A. V. Gavrilin, and H. W. Weijers, "Modeling of Quench in the Coupled HTS Insert/LTS Outsert Magnet System of the NHMFL," *IEEE Trans. Appl. Supercond., vol. 27, no. 5, August 2017*.

[34] A. Morandi, M. Breschi, M. Casali, M. Fabbri, C. Ferdeghini, U. Gambardella, A. Malagoli, S. Pace, P. L. Ribani, G. Romano, A. Saggese, and M. Vignolo, "Quench Behavior of MgB2 Pancake Coil for FCL Applications," *IEEE Trans. Appl. Supercond., vol. 23, no. 3, August 2013*.

Conclusions

A fundamental step in the design of superconducting magnets is the calculation of the minimum energy that determines the transition of the superconducting material from the superconducting to the normal state. In the present work several numerical models are developed and applied to the analysis of quench in superconducting HTS magnets. The large scale and hence the large number of degrees of freedom of superconducting magnets and moreover the high aspect ratio that characterize the REBCO-based materials require the introduction of numerical techniques that reduce the computational effort to a reasonable scale.

In the present work, several numerical models are presented. In the second chapter the first prototype developed in the R&D activity for the 32-T magnet project at the NHMFL is discretized adopting a quasi-3D FEM model. In the third chapter, the same model is applied for the quench analysis of the second prototype of the NHMFL, able to describe the inductive coupling between the HTS insert coil and the LTS outsert. In the fourth chapter, the same model is applied for the study of the 32 T magnet itself, an HTS magnet composed of two coil and 120 pancakes in total. In the fifth chapter, the same approach applied for the NHMFL coils is used for the modelling of quench initiation and propagation in the Roebel cable for the EuCard-2 project.

In the last chapter, a different topic is presented. The ac and coupling losses in the operating cycle of a Gantry magnet system are studied in detail. The computed losses are introduced in a thermal model to study the temperature margin and the safety operation conditions of the magnet during its operating cycle.

The modelling of the large scale superconducting devices requires the introduction of a technique for the reduction of the degrees of freedom. To this purpose, the different layers that compose the REBCO tape are homogenized considering the different materials as in parallel for the longitudinal properties and as in series for the transversal ones, thus obtaining a anisotropic equivalent material. The approach allows one to consider a single element (the pancake in the NHMFL coils and the single tape in Roebel cable) as composed by a single material; nevertheless the model is able to compute precisely the magnetic flux density, the temperatures and voltages

at each location of the pancake for the NHMFL coils and along the tapes of the Roebel cable. The homogenized approach is further applied in the last chapter. While in the NHMFL coils and in the Roebel cable cases, the homogenization is applied at the conductor level, in the temperature margin study of the Gantry magnet, the global magnet is homogenized to determine the properties of a single anisotropic material.

In the first part of this work, the solution of temperatures and voltages of the pancakes (for the NHMFL coils) and of the tape (for the Roeble cable) is based on the discretization of one single mesh. The solution of the current density continuity condition and of the heat balance equation for an array of variables (voltage and temperature) one for each pancake of the coil or for each tape of the cable.

The possibility to simulate experimental tests is allowed by the coupling of the detailed FEM model with a general law determined on the base of the Kirchhoff's relations. In the case of the NHMFL coils, the heat balance equation and the current density continuity condition is coupled with the coil constitutive law. The approach enables the study of both the detailed and the global behaviour of a magnet during quench.

The aim of the developed numerical models is the analysis of quench initiation and propagation. In the different cases where the models are applied, the models allowed to study the Minimum Quench Energy (MQE) and the Normal Zone Propagation Velocity (NZPV). The MQE is determined in the different cases in the range of about 50 J. The Normal Zone Propagation Velocity is computed between 6 cm/s and 15 cm/s. Both MQE and NZPV are in line with the values available in the literature.

The study of the temperature distributions and of the voltage profiles are of great importance to investigate in detail the behavior of a magnet during quench and to determine the hot spot points and areas that could determine the damage of the magnet. A key role in the protection of a magnet from permanent damages is played by the quench protection system. The threshold voltage of the protection system is a crucial parameter: a too high value could determine the disruption of the magnet, whereas a too low value could affect the nominal operation of a magnet. In the case analysed, the terminal voltages of each pancake in the NHMFL coils, the voltage profile of the tapes and the quench decision time of about 10 s in the Roebel cable are determined with care so as to be useful for the setting of a reliable value of threshold voltage in the quench protection system.

If, on one side, the models give the chance to study the details of quench initiation and propagation, on the other side they give the opportunity to analyse the global behavior of a magnet. In most of the selected cases, the current decay of the magnets is presented in order to give an insight of the damping time. The influence of the different pancakes (for the NHMFL coils) or of the different tapes (for the Roebel cable) on the quench of the analysed magnets is studied in detail to determine the most stressed area

of a magnet and the impact on quench of the main variables: temperature, magnetic flux density, field angle, heater location. The total amount of energy stored in the magnet and the energy exchange between the insert and the outsert are determined to study the impact of the outsert on the quench of the insert.

In the second part of this work, a numerical approach is applied for the determination of the temperature margin in the Gantry magnet system. The technique is focused at the determination of ac and coupling losses in a range of 100 W/m^3 and 10 W/m^3 respectively and the introduction of the losses in the thermal model to determine the temperature increase of the magnet. A temperature margin of about 2 K allows one to conclude the safety operation of the Gantry system.

In conclusion, based on the same techniques, homogenization procedure, single mesh and resolution of an array of variables, different models are developed in this work. The comparison of the models with experimental and with numerical investigations performed by other research groups allow to be confident of the approach proposed and the possibility to be applied also to large scale magnets.